In-Situ Monitoring of Microwave Plasma-Enhanced Chemical Vapour Deposition Diamond Growth

William George Smith Leigh

Submitted in partial fulfilment of the requirements for the degree of Doctor of Philosophy

School of Physics and Astronomy
Cardiff University

2022

Abstract

With a wealth of extreme properties, including the highest thermal conductivity of any known material, diamond is a highly desirable material for a wide range of applications. However, the growth of high-quality diamond films on heterogeneous materials can be challenging. With the properties of diamond films highly dependent on the substrate temperature during growth, non-uniform substrate temperature will result in the growth of inhomogeneous films. Chapter 4 details the development of an inexpensive temperature mapping system, combining dual wavelength pyrometry with a mirror galvanometer to produce substrate temperature maps under growth conditions. Temperature maps produced are compared to finite element simulations and spectroscopic ellipsometry and Raman spectra, with good agreement between the results.

As well as substrate temperature, the quality of diamond films is dependent on the early stages of growth. In Chapter 5, spectroscopic ellipsometry is applied to the initial stages of diamond growth on silicon. *Ex-situ* spectra are used to develop an optical model for characterisation, which is then applied to *in-situ* spectra. The model identified the point of coalescence of crystallites into a single film through a decrease in bulk void content followed by a spike in sp^2 content. *Ex-situ* Raman spectra and atomic force microscopy images were used to validate the model.

One potential application of diamond is for thermal management of gallium nitride devices, with potential growth routes on an aluminium nitride interlayer atop the GaN stack. This application is limited by a thermal resistance associated with the disordered transition region formed in the early stages of growth. Chapter 6 utilises spectroscopic ellipsometry for *in-situ* monitoring of the early stages of diamond growth on AlN, with observations again verified by Raman spectroscopy and atomic force microscopy images.

Acknowledgements

Firstly, I would like to thank my supervisor, Prof. Oliver Williams. His continued support and infectious enthusiasm for scientific research have been a driving force behind the production of this thesis.

Also from the Cardiff Diamond Foundry, I would like to thank Dr. Evan Thomas, Dr. Jerome Cuenca, and Dr. Soumen Mandal for their everyday assistance in the lab, training me on the usage of lab equipment, and patience with my frequently stupid questions. Thanks also go to Henry Bland, Scott Manifold, and Jaspa Stritt for non-scientific discussions and commiserating over failed experiments.

Finally, this thesis would not have been possible without the support I have received from friends and family, including (but not limited to) Ivan, Kate, Dan, Lara, Jambon, Elsa, and especially Mum and Ian. Thank you all for putting up with me.

The following experimental work was not conducted by the author:

- Finite element simulations in Chapter 4 were carried out by Dr. Jerome Cuenca. The analysis in this thesis was written by the author.
- Aluminium nitride substrates in Chapter 6 were grown by Prof. David Wallis from the Cardiff University School of Engineering and Cambridge University Department of Materials Science and Metallurgy.

Publications

W. G. S. Leigh, J. A. Cuenca, E. L. H. Thomas, S. Mandal, O. A. Williams, "Mapping the effect of substrate temperature inhomogeneity during microwave plasma-enhanced chemical vapour deposition nanocrystalline diamond growth", Carbon. **201** (2023) 328–337.

W. G. S. Leigh, E. L. H. Thomas, J. A. Cuenca , S. Mandal, O. A. Williams, "*In-situ* monitoring of microwave plasma-enhanced chemical vapour deposition diamond growth on silicon using spectroscopic ellipsometry", Carbon. **202** (2023) 204–212.

Conference Presentations

Oral

W. G. S. Leigh, E. L. H. Thomas, J. A. Cuenca, S. Mandal and O. A. Williams, "*In-situ* monitoring of CVD diamond growth on silicon using spectroscopic ellipsometry", De Beers Diamond Conference 2022.

Poster

W. G. S. Leigh, J. A. Cuenca, E. L. H. Thomas and O. A. Williams, "*In-situ* MPECVD temperature mapping using dual-wavelength pyrometry", Hasselt Diamond Workshop 2020.

W. G. S. Leigh, J. A. Cuenca, E. L. H. Thomas, S. Mandal and O. A. Williams, "The effect of substrate temperature inhomogeneity during microwave CVD nanocrystalline diamond growth", De Beers Diamond Conference 2021.

W. G. S. Leigh, E. L. H. Thomas, J. A. Cuenca, A. Hinz, R. Oliver, D. J. Wallis, S. Mandal and O. A. Williams, "Spectroscopic ellipsometry of nanocrystalline diamond film growth on aluminium nitride", Hasselt Diamond Workshop 2022.

W. G. S. Leigh, E. L. H. Thomas, J. A. Cuenca, A. Hinz, R. Oliver, D. J. Wallis, S. Mandal and O. A. Williams, "Spectroscopic ellipsometry of nanocrystalline diamond film growth on aluminium nitride", De Beers Diamond Conference 2022.

Contents

List of Figures

List of Tables

Acronyms

AFM Atomic Force Microscopy.

BEN Bias-Enhanced Nucleation.

CVD Chemical Vapour Deposition.

EMA Effective Medium Approximation.

FEM Finite Element Model.

FWHM Full Width at Half Maximum.

HFCVD Hot Filament Chemical Vapour Deposition.

HPHT High Pressure High Temperature.

MOCVD Metalorganic Vapour-Phase Epitaxy.

MPECVD Microwave Plasma-Enhanced Chemical Vapour Deposition.

MSE Mean Square Error.

RMS Root Mean Square.

SE Spectroscopic Ellipsometry.

SEM Scanning Electron Microscopy.

STEM Scanning Transmission Electron Microscopy.

TEM Transmission Electron Microscopy.

Chapter 1

Introduction

The extreme properties of diamond films make them desirable in a wide range of applications. These properties and several applications are discussed in Chapter 2, along with three different methods of artificial diamond synthesis. This thesis focuses on the growth of diamond films by Microwave Plasma-Enhanced Chemical Vapour Deposition (MPECVD), with the experimental techniques used described in Chapter 3. High quality diamond films can be challenging to grow, particularly over large areas. Firstly, the properties of a diamond film are heavily dependent on the substrate temperature, with higher growth temperatures known to result in a faster growth rate [1] and lower level of sp^2 content [2]. Inhomogeneity in substrate temperature during growth will result in the growth of a non-uniform film. This is a particular concern in MPECVD growth, as the plasma generated (which causes heating of the substrate) is typically non-uniform in distribution [3]. The size, shape, and temperature of this plasma are influenced by the microwave power and chamber pressure. Selection of the optimum parameters for MPECVD growth therefore requires the ability to evaluate the uniformity of substrate temperature. In Chapter 4 a simple-to-implement and inexpensive non-contact method of measuring the temperature variation across the substrate under growth conditions is detailed. The existing technique of dual-wavelength pyrometry is combined with a mirror galvanometer, producing two-dimensional temperature maps. Temperature maps produced are compared with Finite Element Model (FEM) simulations and Raman and SE spectra. The work carried out in this chapter is published in [4].

Also important during the diamond growth process are the seeding, nucleation, and early stages of film growth, with the quality of films produced heavily dependent on these [5]. The ability to monitor growth *in-situ* is therefore incredibly important to optimise film quality. However, the harsh plasma environment largely restricts *in-situ* monitoring to optical techniques, as the relatively high pressure during growth prevents the use of electron-based techniques such as reflection high-energy electron diffraction. Laser and pyrometric interferometry are commonly used to monitor the film thickness during growth [6, 7], although these can be limited in resolution and do not provide any compositional information. Raman spectroscopy can be used to determine the composition of diamond films [8, 9], but it much more sensitive to sp^2 material than to diamond and totally insensitive to void [10]. SE provides advantages over these techniques, with an ability to determine the thickness of diamond films as thin as 4 nm with sub-nanometre resolution, as well as identify the diamond, sp^2, and void content [11]. Furthermore, as SE relies on the measurement of a change in polarisation state upon reflection and not intensity of the reflected light, it can be used for *in-situ* measurement even in the case of a bright plasma background [12]. Whilst previous attempts at *in-situ* SE characterisation of diamond films have been made, the ability to characterise early-stage growth has been limited by substrate damage caused by the process of mechanical abrasion used to seed substrates. Chapter 5 details *in-situ* SE of diamond growth on silicon substrates seeded with diamond nanoparticles, a process which does not cause substrate damage. *Ex-situ* spectra are used to build up an optical model of the diamond film, which is then applied to *in-situ* spectra, with characterisation of the initial stages of growth and determination of the point of coalescence of individual crystallites into a film demonstrated. Atomic Force Microscopy (AFM) and Raman spectroscopy are used to validate the model. The work detailed in this chapter is published in [13].

With its incredibly high thermal conductivity [14], diamond is an ideal material for thermal management. When diamond layers are grown on heterogeneous materials for this purpose, the early stages of growth are of an even greater importance; the thermal barrier at the substrate-diamond interface (associated with the disordered transition region formed during the early stages of growth) is often a significant limitation [15]. One potential thermal management application of diamond is on top of gallium nitride devices. Whilst growth of a thick diamond film directly on GaN is challenging [16], it is possible to grow thick diamond films on aluminium nitride [17], leading to potential diamond growth routes on an AlN interlayer atop the GaN stack [18]. In comparison to growth on Si substrates, growth of diamond layers on AlN is less understood [17]. Chapter 6 extends the work carried out in Chapter 5 by applying SE to early-stage diamond growth on AlN. *Ex-situ* spectra are used to develop an optical model for the AlN film and then a diamond film grown on AlN, with the model then applied to *in-situ* spectra. Early-stage growth and the coalescence of crystallites are observed, with the model validated using *ex-situ* Raman spectroscopy and AFM. Chapter 7 concludes this thesis, with a summary of the key findings and a discussion of potential future work.

Chapter 2

Diamond Properties and Growth

This chapter gives a brief overview of the structure, properties and applications of diamond, before describing several different methods of diamond synthesis. Finally, growth of diamond on heterogeneous substrates is described, including an evaluation of the pre-treatment processes necessary to achieve the high nucleation density needed for the growth of coalesced films on these substrates.

2.1 Structure, Properties, and Applications of Diamond

Carbon has 6 electrons which adopt the configuration $1s^2\ 2s^2\ 2p^2$ in the ground state, with the latter four electrons available for bonding. The single 2s and three 2p orbitals can combine to form four hybrid sp^3 orbitals as shown in Figure 2.1 [19]. This allows for the formation of sigma bonds with four other carbon atoms in a tetrahedral arrangement. The bonding of a large number of carbon atoms in this pattern results in a diamond crystal. This arrangement has a relatively short bond length of 0.154 nm, with a high bond energy of 711 kJ mol^{-1} [20]. The structure of the diamond crystal is made up of two face-centred cubic lattices with one displaced by (1/4 a, 1/4 a, 1/4 a), with a being the lattice constant of diamond (3.567 Å) [21]. This structure is shown in Figure 2.2.

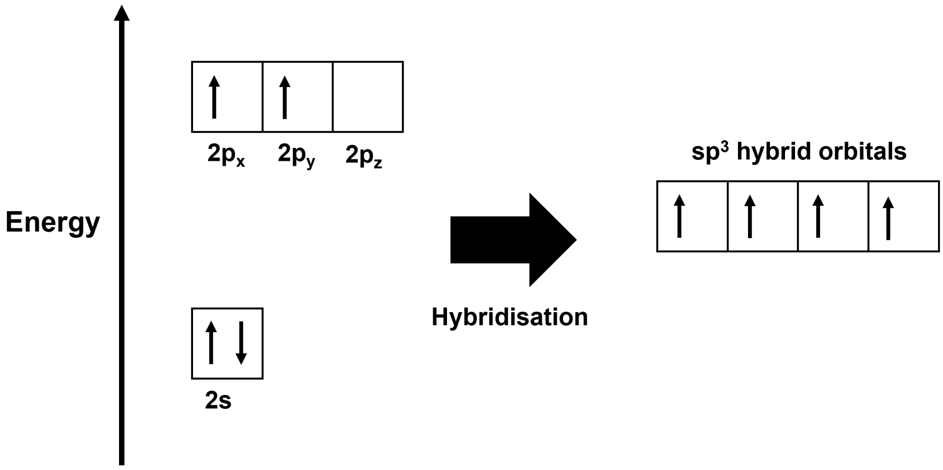

Figure 2.1: sp^3 hybridisation of carbon orbitals.

The structure and bonding of diamond result in many superlative properties, some of which are listed below:

- Diamond has the highest atom density of any known material with a molar density of 0.293 g-atom/cm^3, and so is incredibly hard and very incompressible [21].
- The very high vibrational frequencies of the bonds result in diamond having the highest thermal conductivity of any known material at room temperature [22].

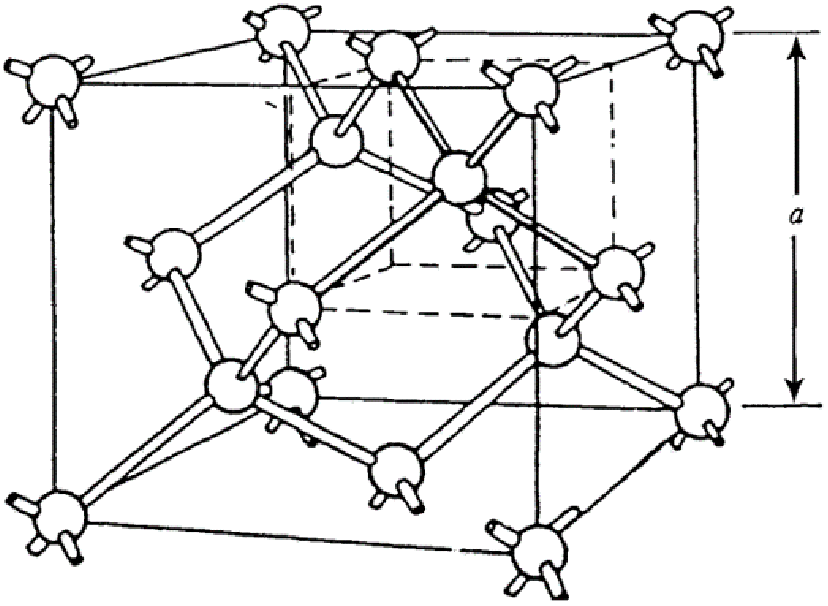

Figure 2.2: Crystal structure of diamond. Reproduced with permission from [21].

- Diamond has a high index of refraction (2.417) and is transparent from 0.22 μm all the way to the far infrared region of the spectrum [23].
- Diamond is chemically and biologically inert [24].
- Undoped diamond has a very high electronic band gap of 5.5 eV [25].
- Diamond has a low coefficient of thermal expansion [19].
- Single crystal Chemical Vapour Deposition (CVD) diamond exhibits the highest hole and electron mobilities of any known wide-bandgap semiconductor at room temperature [26].

With such extreme properties, diamond is a desirable material for use in many applications such as:

- Cutters for oil and gas drilling [27].
- Thermal management for electronic devices [18, 28].
- Boron-doped diamond electrodes [29].
- Filtration of viruses and toxic molecules [30, 31].

- Nuclear fusion reactor windows [32].
- Photodetectors for space applications [33].
- Microelectromechanical systems [34].

2.2 Diamond Synthesis

Sir Humphry Davy proved in 1814 that diamond was composed solely of carbon, burning diamond and noting that only CO_2 was produced [35]. This discovery spurred a multitude of unsuccessful attempts at the production of synthetic diamond over the course of more than a century, although success was not achieved until the 1950s. Part of the difficulty of diamond synthesis is due to the fact that diamond is only metastable, with graphite being the more stable allotrope at room temperature and pressure. However, the energy barrier required to rearrange the structure means that conversion from diamond to graphite does not readily occur under these conditions [36]. With the application of pressure, diamond becomes the thermodynamically favourable allotrope [37]. Figure 2.3 shows a phase diagram of carbon with changing temperature and pressure. Whilst diamond becomes thermodynamically favoured at low temperature and high pressure, the kinetic barrier means that very high pressures and temperatures (in excess of 13 GPa and 3300 K) are required for the reaction to actually proceed at a rate that is observable [38]. In practice, such conditions are very challenging and expensive to produce.

2.2.1 High Pressure High Temperature

In the 1950s, work carried out simultaneously by General Electric in the USA [39], ASEA in Sweden [40], and the Institute of High Pressure Physics in the Soviet Union [41] resulted in the development of the catalyst-assisted High Pressure High Temperature (HPHT) technique, creating a synthetic route with lower activation energy than the direct transition from graphite to diamond. This technique utilises a catalytic solvent, usually a transition metal such as iron, cobalt or nickel, coupled with a graphitic carbon source and a seed diamond. The solvent dissolves

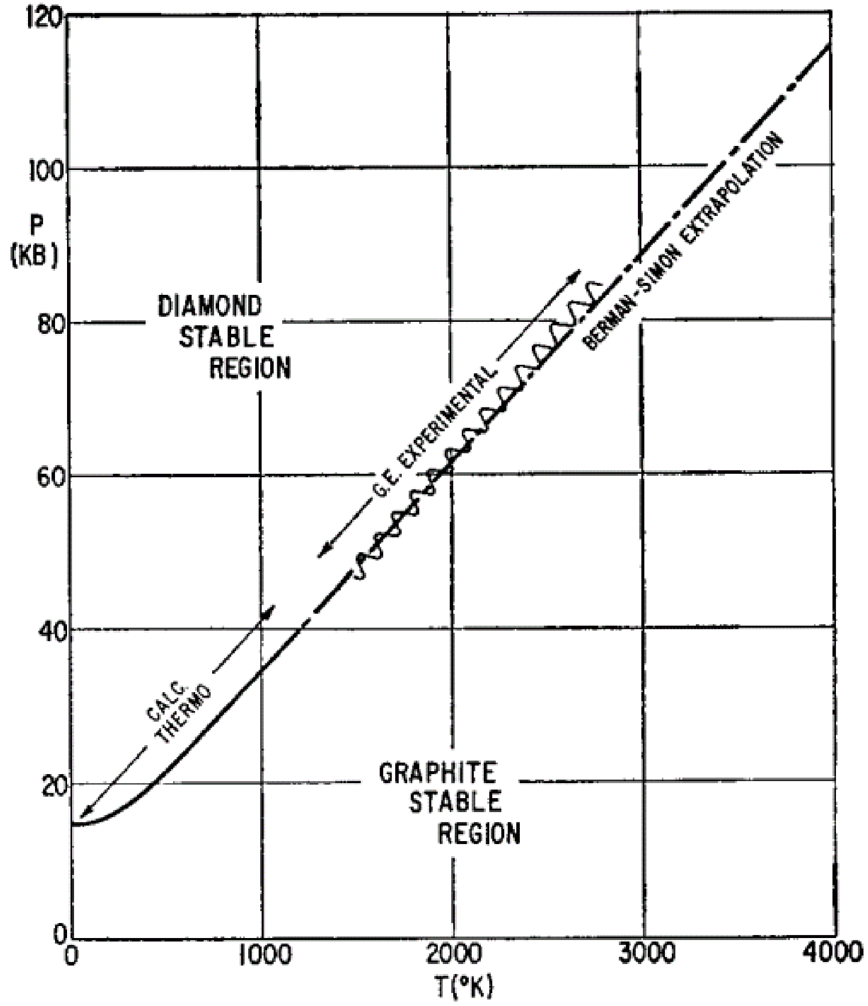

Figure 2.3: Phase diagram of carbon with changing temperature and pressure. Reprinted from F. P. Bundy et al., "Diamond-Graphite Equilibrium Line from Growth and Graphitization of Diamond", The Journal of Chemical Physics **35**, 383–391 (1961), with the permission of AIP Publishing.

carbon, breaking down carbon-carbon bonds, and transports carbon atoms to the diamond surface. With such an approach, the pressures and temperatures required for diamond growth are significantly reduced to the order of 1500 K and 5 GPa [19]. These conditions are typically achieved using a hydraulic press. The limitations of this method are the high levels of incorporation of nitrogen and solvent metals into the diamond crystal, along with the limitation of crystal sizes to the order of millimetres [42].

2.2.2 Detonation

The shockwave from an explosion generates a very high temperature and pressure for a few fractions of a second, and can be used to synthesise diamond [19]. This was discovered in the 1960s by researchers in the Soviet Union attempting to synthesise diamond through the compression of graphite and carbon black. It was found that placing a carbon source directly within the charge resulted in a much greater yield [43]. Explosive mixtures with the composition $C_aH_bN_cO_d$ with a negative oxygen balance (where the mixture contains fewer oxygen atoms than is necessary to oxidise all the components) are typically used for this purpose, as these result in incomplete combustion and therefore formation of elemental carbon [43]. Figure 2.4 shows a phase diagram of carbon, along with a line showing the temperature and pressure experienced during detonation synthesis. The line AB indicates the decomposition of the explosive mixture, which moves temperature and pressure above the M1 phase line, leading to the formation of liquid carbon clusters which condense to form 5 nm diamond nanoparticles. The Jouguet point, B, indicates the end of combustion. From this point the pressure rapidly drops, with the high temperature decaying more slowly, resulting in the formation of graphitic shells around the diamond nanoparticles. Aggregates approximately 100-200 nm in size are typically formed by this process, shown in Figure 2.5.

2.2.3 Chemical Vapour Deposition

The challenges of methods replicating the natural conditions for diamond growth led to the search for new methods of growth at low pressures. Initial experiments

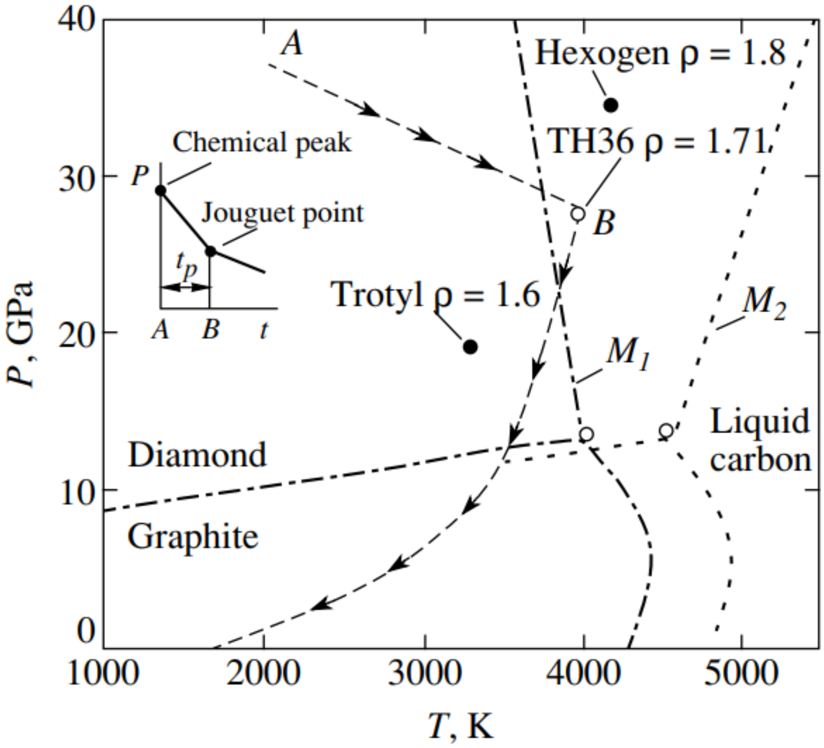

Figure 2.4: Phase diagram of carbon during detonation diamond synthesis. The inset indicates the pressure profile of the explosion. Reproduced from [43], with permission from Springer Nature.

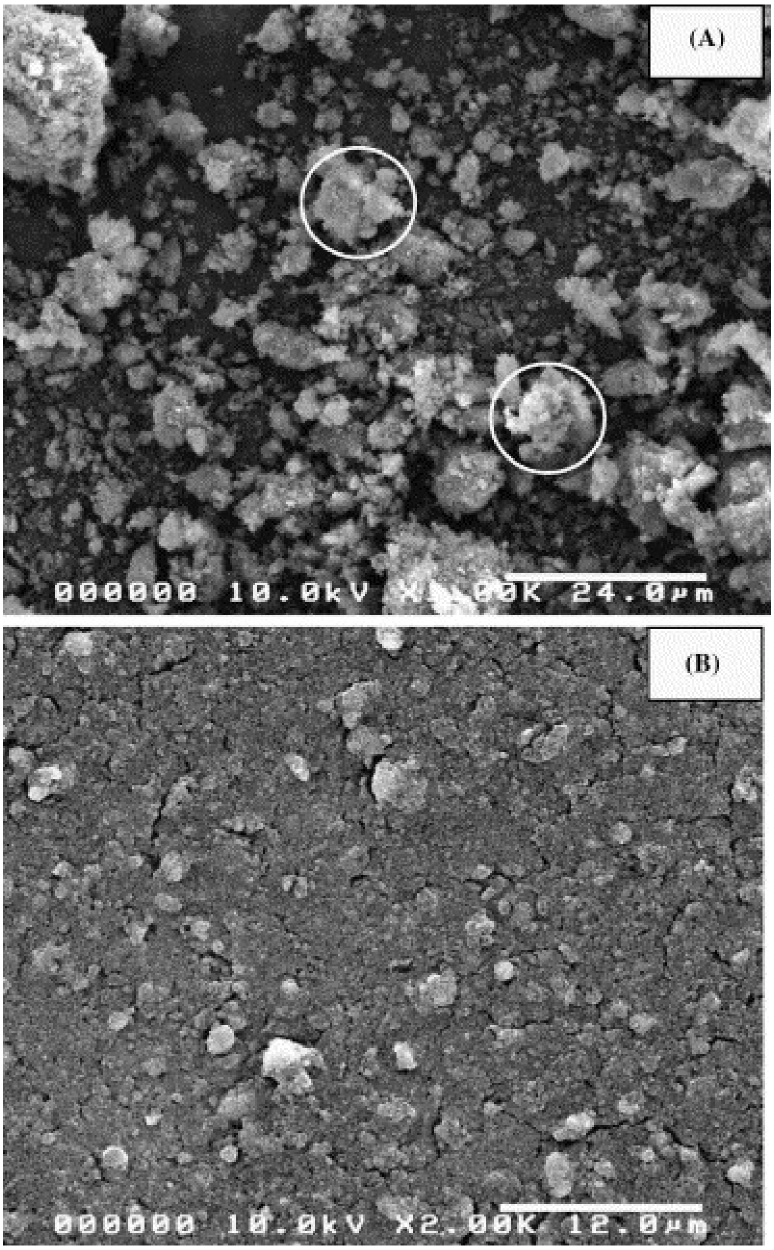

Figure 2.5: SEM images of detonation diamond aggregates. Reprinted from A. Krüger et al., “Unusually tight aggregation in detonation nanodiamond: Identification and disintegration”, Carbon **43**, 1722–1730 (2005), © 2005, with permission from Elsevier.

by Eversole at the Union Carbide Corporation in 1958 [45] and Deryagin in Russia in 1968 grew diamond on the surface of natural diamond crystals heated to 900 °C by thermal decomposition of carbon-containing precursor gases [42, 46]. This approach was limited by the deposition of sp^2 material at the same time as diamond, limiting growth rate and purity. Angus in 1968 [47] made a key discovery; that atomic hydrogen preferentially etched sp^2 material if present during the growth process, leading to the growth of pure diamond by the CVD method. It was later shown by Russian groups [48] that heterogeneous diamond growth was possible using such a method. The hot filament reactor was developed in 1982 at the Japanese National Institute for Research in Inorganic Materials [49], growing high quality diamond on heterogeneous substrates at rates of approximately 1 μm/hour. The same group developed the microwave plasma reactor the following year [50].

Common to all forms of CVD diamond growth is the requirement of activation of carbon-containing precursors. To result in diamond growth and not graphite, the carbon-containing precursor gas must be diluted in an excess of hydrogen (typically 1-5%), with the substrate temperature in excess of 700 °C [42, 51]. Hot Filament Chemical Vapour Deposition (HFCVD) typically operates in a vacuum chamber maintained at approximately 20-30 Torr, with a substrate heater holding the substrate at temperatures between 700-900 °C [42]. A typical experimental setup is shown in Figure 2.6. Activation of the carbon-containing species is carried out by a metal filament (typically tungsten or tantalum), held a few millimetres above the substrate. This method is relatively inexpensive, and can produce moderate-quality polycrystalline films at rates between 1-10 μm/hr. However, during growth the diamond film becomes contaminated with metal from the filament, making HFCVD unsuitable for the growth of diamond for electronic applications [42].

An alternative method of activating the growth species is through MPECVD, where microwaves are coupled into the chamber. Heating of gas molecules through collisions with electrons leads to dissociation and the formation of growth species [42]. Diamond is then grown on a substrate immersed in the plasma. A typical

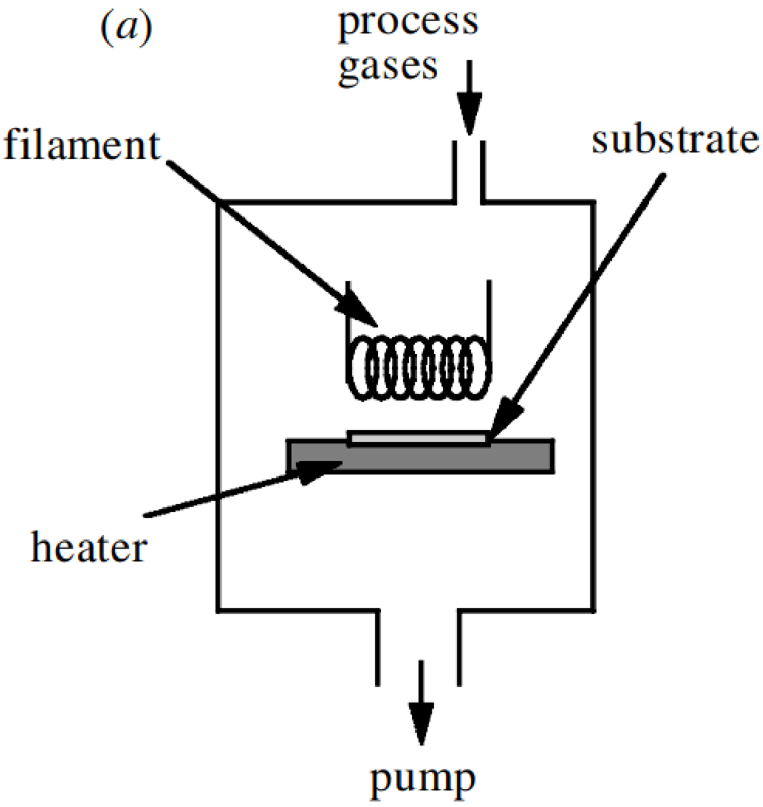

Figure 2.6: HFCVD experimental setup. Reprinted from [42], by permission of the Royal Society.

MPECVD reactor is shown in Figure 2.7. Large substrates can be grown on in this way, with high microwave powers allowing for growth rates exceeding 10 μm/hour [42]. Furthermore, with no filament involved the problem of contamination is removed, with MPECVD capable of producing high quality films. [42].

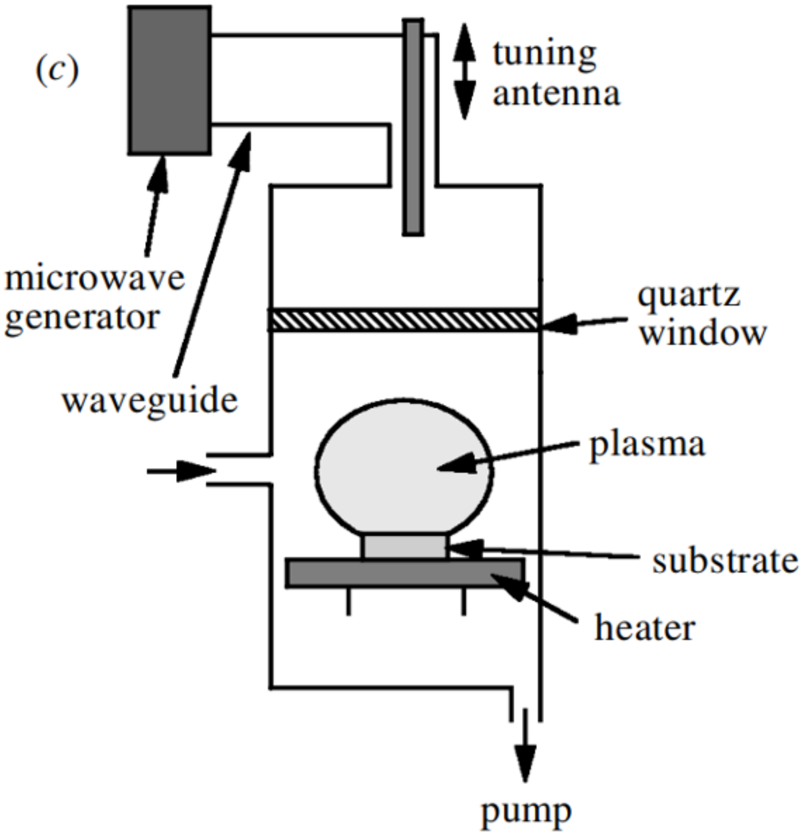

Figure 2.7: MPECVD experimental setup. Reprinted from [42], by permission of the Royal Society.

Whilst complex, the chemistry of the CVD growth process is now largely understood. A simplified version is provided below and pictured in Figure 2.8. [42, 52]. Within the plasma, H_2 molecules dissociate to form reactive atomic hydrogen. This can react with carbon-containing molecules to form reactive hydrocarbon species such as $CH_3^\bullet$. Under growth conditions, the surface of the diamond is almost completely terminated with hydrogen. Atomic hydrogen will abstract a surface hydrogen atom, creating a reactive surface site and forming H_2. Whilst most of these reactive sites will react with nearby hydrogen atoms and return to the previous state, in some cases a nearby $CH_3^\bullet$ radical will react with the surface site, adding a carbon atom to the lattice. If this occurs at adjacent sites, hydrogen abstraction can form a reactive radical from one of the adsorbed CH_3 species, creating a $CH_2^\bullet$ group, which can react with the neighbouring CH_3 group to form a carbon-carbon bond. Repetition of this process results in stepwise growth of the diamond crystal.

2.3 Diamond Growth on Heterogeneous Substrates

Heterogeneous growth of single crystal diamond is only possible on single crystal iridium [53], with attempts at growth on non-diamond materials resulting in polycrystalline films [51]. However, polycrystalline films maintain many of the extreme properties of diamond whilst allowing for growth over large areas [51]. Growth of diamond on untreated silicon results in nucleation densities that are too low for the growth of coalesced films, to the order of 10^4-10^5 cm^{-2} [54]. Figure 2.9 shows AFM images of two substrates after exposure to MPECVD growth conditions, one seeded with diamond nanoparticles and the other untreated. There is no significant film growth visible in the latter. There are several reasons for the low nucleation density. Firstly, the surface energy of diamond is significantly higher than that of silicon (6 J/cm^2 vs 1.5 J/cm^2 [55]). In addition, competition occurs from non-diamond phases, and the carbon-containing precursors have a low sticking coefficient on the substrate. Therefore, heterogeneous substrates require a pre-treatment step prior to growth to enhance the nucleation density. Several different approaches have been used for this purpose.

2.3.1 Nucleation Enhancement Techniques

Mechanical abrasion of substrates with diamond powder has been shown to significantly enhance nucleation density [56]. Spontaneous nucleation of diamond can occur on defects in the wafer formed by this process, but the main mechanism for enhancing nucleation is through diamond particles being embedded in the substrate. These act as nuclei for the growth of diamond, with nucleation densities of up to 10^{10} cm^{-2} reported [56]. The main disadvantage of this technique is that it results in significant substrate damage.

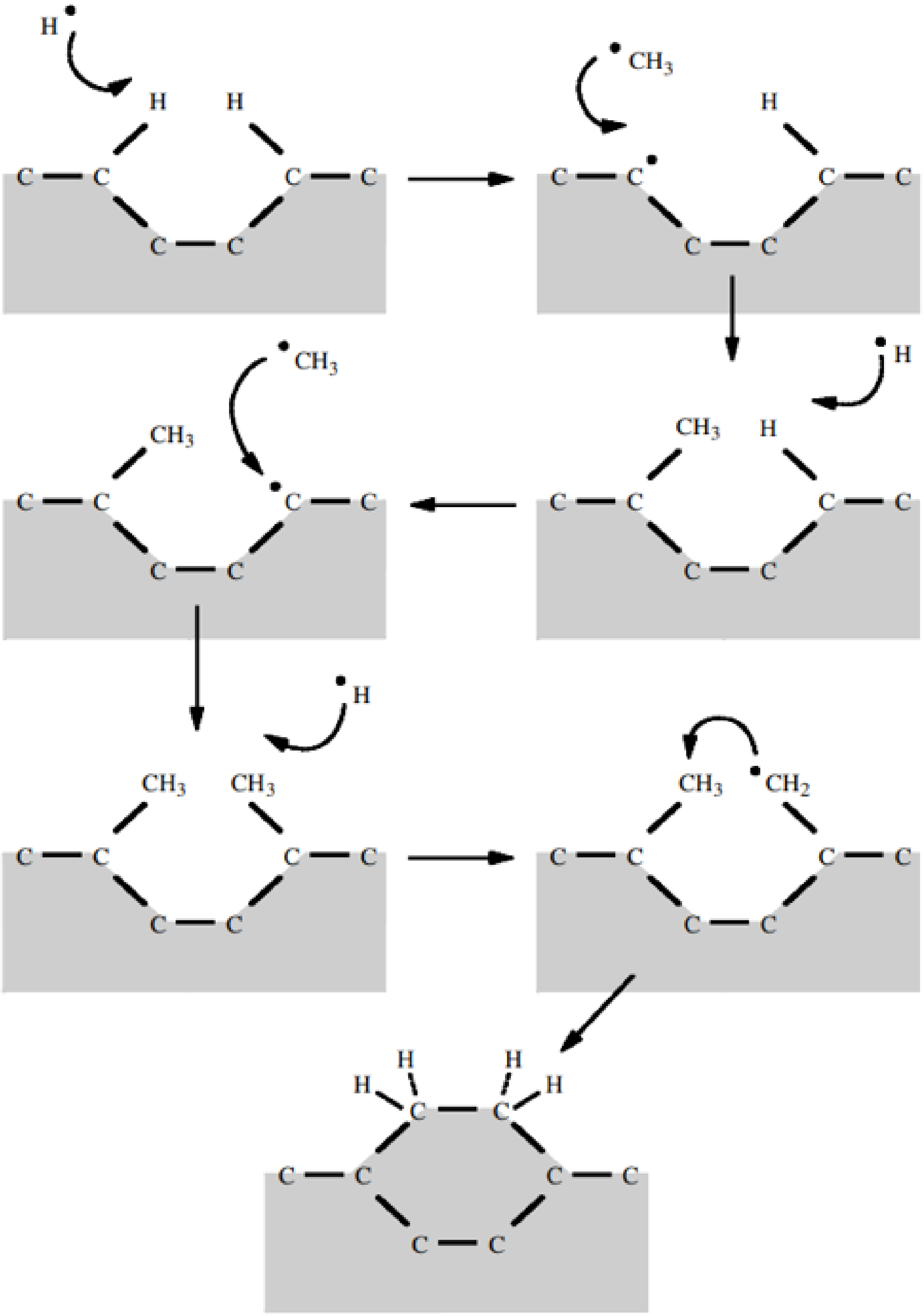

Figure 2.8: Simplified chemistry of the CVD growth process. Reprinted from [42], by permission of the Royal Society.

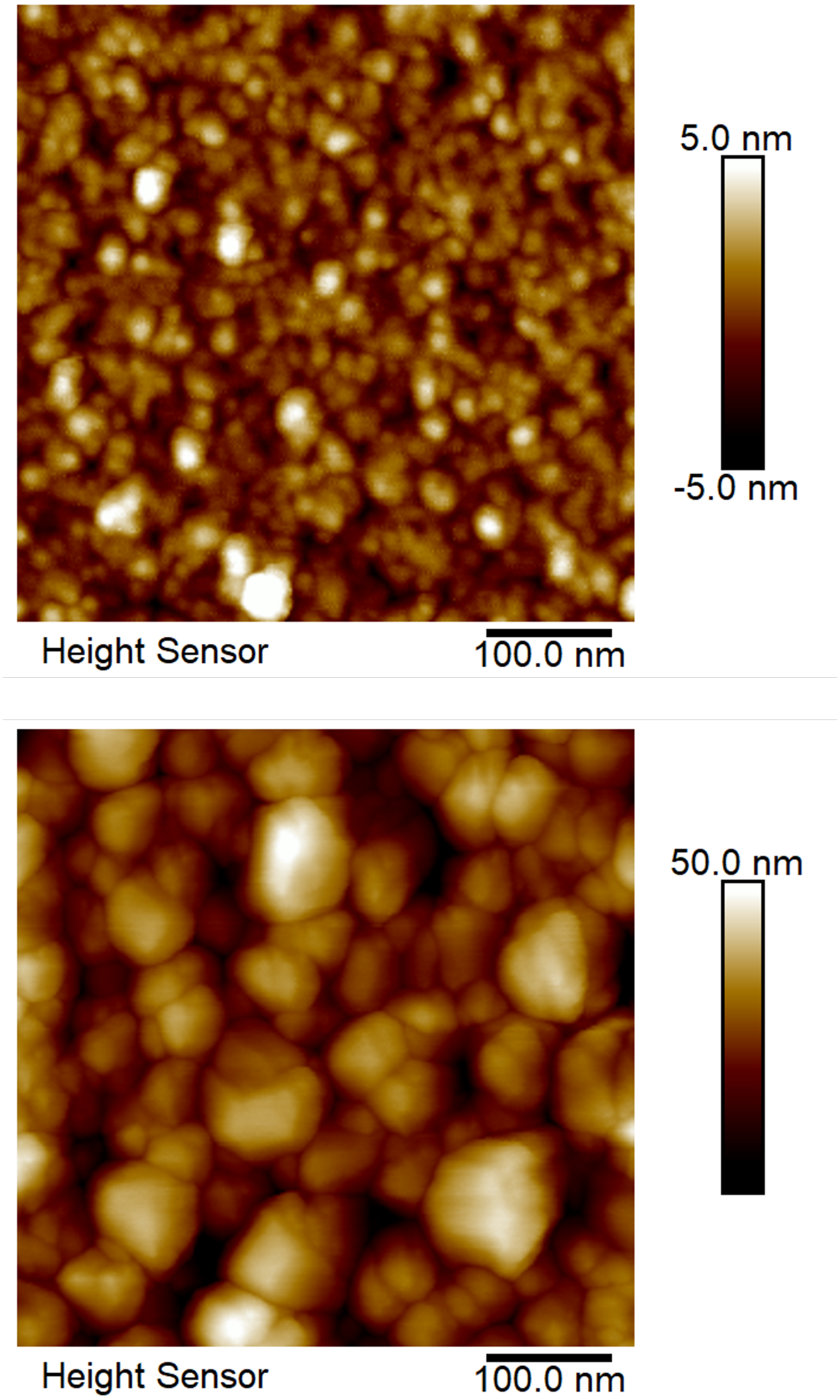

Figure 2.9: AFM images of silicon substrates after exposure to MPECVD diamond growth conditions. Top: Unseeded substrate. Bottom: Substrate seeded with diamond nanoparticles. No significant film growth is seen on the unseeded substrate.

Ultrasonic treatment of substrates immersed in slurries containing micron-sized diamond particles can result in nucleation densities of up to 10^{11} cm^{-2} [57]. The ultrasound treatment causes damage to the substrate and embeds diamond particles within it, with nucleation occurring as a result of diamond growth on these fragments, as is the case with mechanical abrasion [57]. Whilst this process produces high nucleation densities, the problem of substrate damage is still present.

Bias-Enhanced Nucleation (BEN) involves the negative biasing of a conductive substrate by 100-250 V relative to either a second electrode or the reactor chamber. It is typically carried out under high-methane conditions (4-10% diluted in hydrogen) [58].Incident CH_X^+ ions will have an energy of approximately 80 eV, which is sufficient to sub-plant them into the substrate, forming an amorphous carbon layer [59]. Nucleation sites arise from either the formation of nanocrystalline graphite due to the high substrate temperature or the formation and annealing of sp^3 sites within the amorphous layer [51, 59]. BEN can produce nucleation densities of 10^{10} cm^{-2} [60] but requires the use of conductive substrates.

As diamond particles act as nucleation sites for growth, nucleation density can be enhanced by coating the surface of a substrate with diamond particles. This has the advantage of avoiding substrate damage, and unlike BEN does not require a conductive substrate. With the use of nanometre-scale diamond particles, produced through either milling or detonation synthesis, very high seeding densities are possible [61]. Substrates are immersed in a diamond particle solution, with particles adhering to the growth substrate through electrostatic attraction [61, 62]. Detonation synthesis provides very small diamond particles, ideal for high nucleation densities. However, these require additional treatment prior to use in seeding, as the high levels of sp^2 material produced during the synthesis process lead to the formation of agglomerates. These can be broken down through techniques such as oxidation in air [63], bead-milling [44], or hydrogenation [62]. The technique used determines the zeta potential (a measure of surface charge) of the diamond nanoparticles, with oxidation in air and acid cleaned particles having negative zeta potential [63], whilst hydrogenated particles have a positive zeta potential [62]. As the mechanism of adherence to the substrate is through electrostatic attraction, it is important to consider the zeta potential of both substrate and seeds. For example, the thin SiO_2 layer observed to form on silicon wafers under ambient conditions [13] has a negative zeta potential [64], and so high seeding densities can be achieved by using hydrogen-terminated nanoparticles, which have a positive zeta potential. An AFM image of a wafer seeded with diamond nanoparticles can be seen in Figure 2.10, showing the high nucleation density possible with this method.

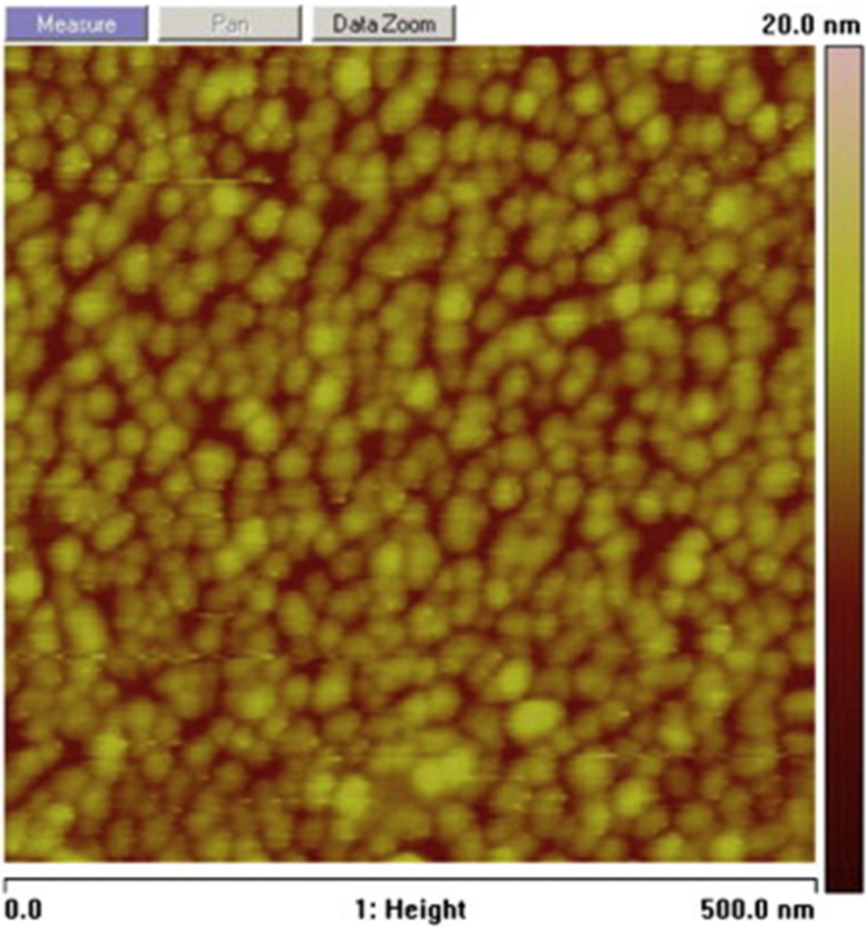

Figure 2.10: AFM image of a silicon wafer seeded with diamond nanoparticles. Reprinted from O. A. Williams, "Nanocrystalline diamond", Diamond and Related Materials **20**, 621–640 (2011), © 2011, with permission from Elsevier.

2.3.2 Growth

During the initial stages of diamond growth, there is a period of time where no film growth occurs, often referred to as the incubation period [51]. As the substrate is not completely covered with diamond nuclei at this point, carbon diffuses into the substrate until either lateral growth of diamond nuclei or the formation of a carbide layer on the substrate prevents this. These early stages typically follow the Volmer-Weber growth model, with adatoms preferentially bonding to diamond nuclei, which leads to the forming of isolated islands [55]. The islands expand both vertically and laterally until they contact, forming a coalesced film. This intersection of crystallites results in the trapping of non-diamond carbon within grain boundaries [65]. After coalescence, growth continues by the van der Drift model. Crystallographic planes normally have different growth rates as a result of differences in sticking probability and surface diffusion rates for each plane [66]. According to the van der Drift evolutionary selection rule, grains growing fastest in the direction perpendicular to the substrate will overgrow slower-growing grains, dominating the film [66, 67]. This results in columnar growth, with crystallite size and surface roughness increasing with film thickness [67, 68]. Figure 2.11 shows a schematic of the early stages of the growth process on silicon, showing the etching of the native oxide by the plasma and the formation of a silicon carbide layer, the formation of isolated islands and coalescence into a single film, as well as the transition to van der Drift-type growth. The length of the incubation period varies with growth conditions, with greater substrate temperatures [2] and higher methane concentrations [13, 51] resulting in a shorter incubation period.

The process of re-nucleation must be considered in the growth of polycrystalline diamond. It occurs when the growth of a crystallite is interrupted by secondary nucleation, triggering new crystallite growth. This interruption of growth increases the level of defects within the film, with increased levels of sp^2 bonding observed in films grown with renucleation [69]. High levels of re-nucleation will reduce grain size, which can produce films with a low surface roughness [51]. Figure 2.12 shows SEM images of two films, one with suppressed renucleation and one with enhanced re-nucleation. The larger grain size and increased surface roughness is clearly visible in the former. Re-nucleation is enhanced by greater methane concentrations and lower substrate temperatures [51].

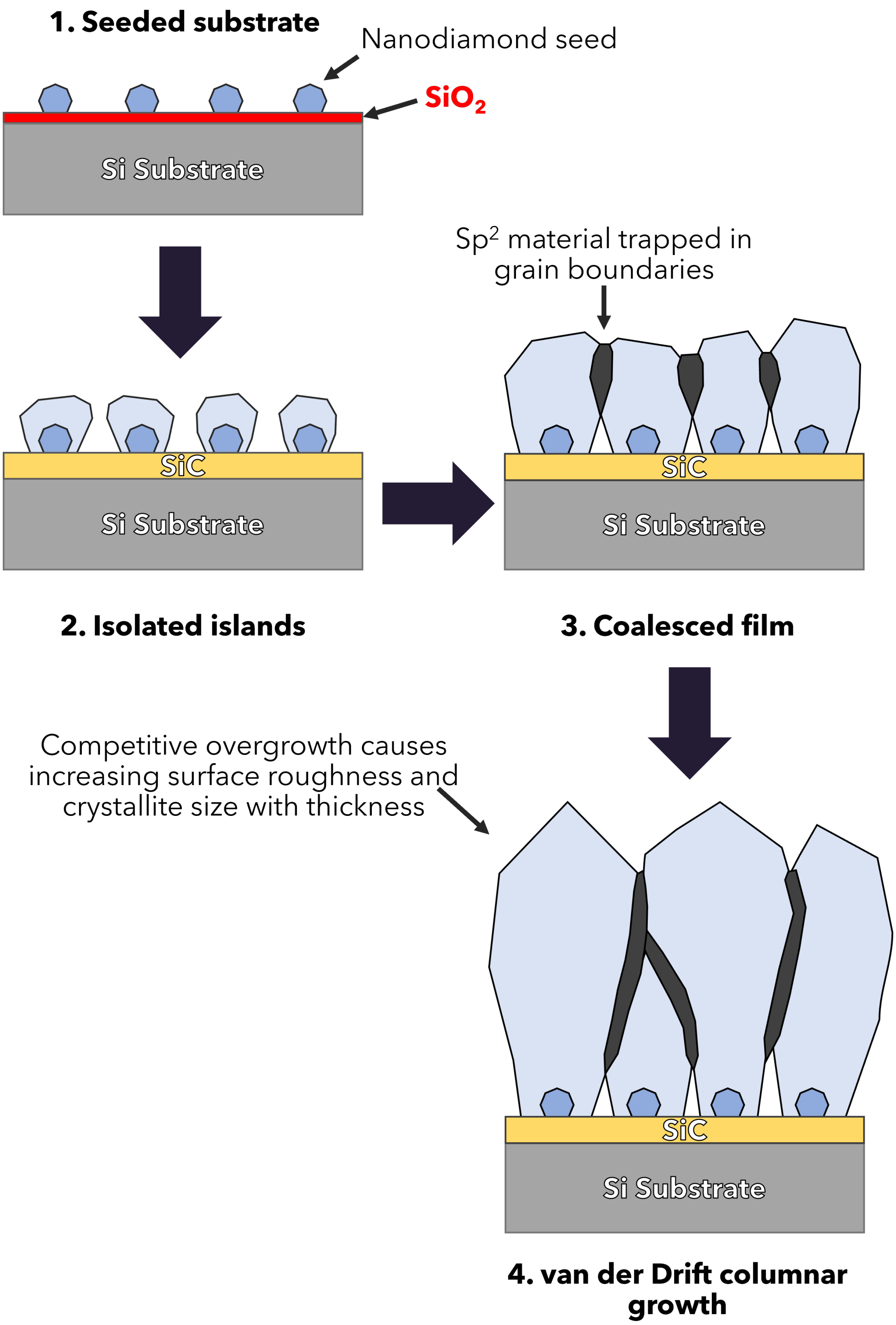

Figure 2.11: Schematic of the early stages of MPECVD diamond growth on silicon.

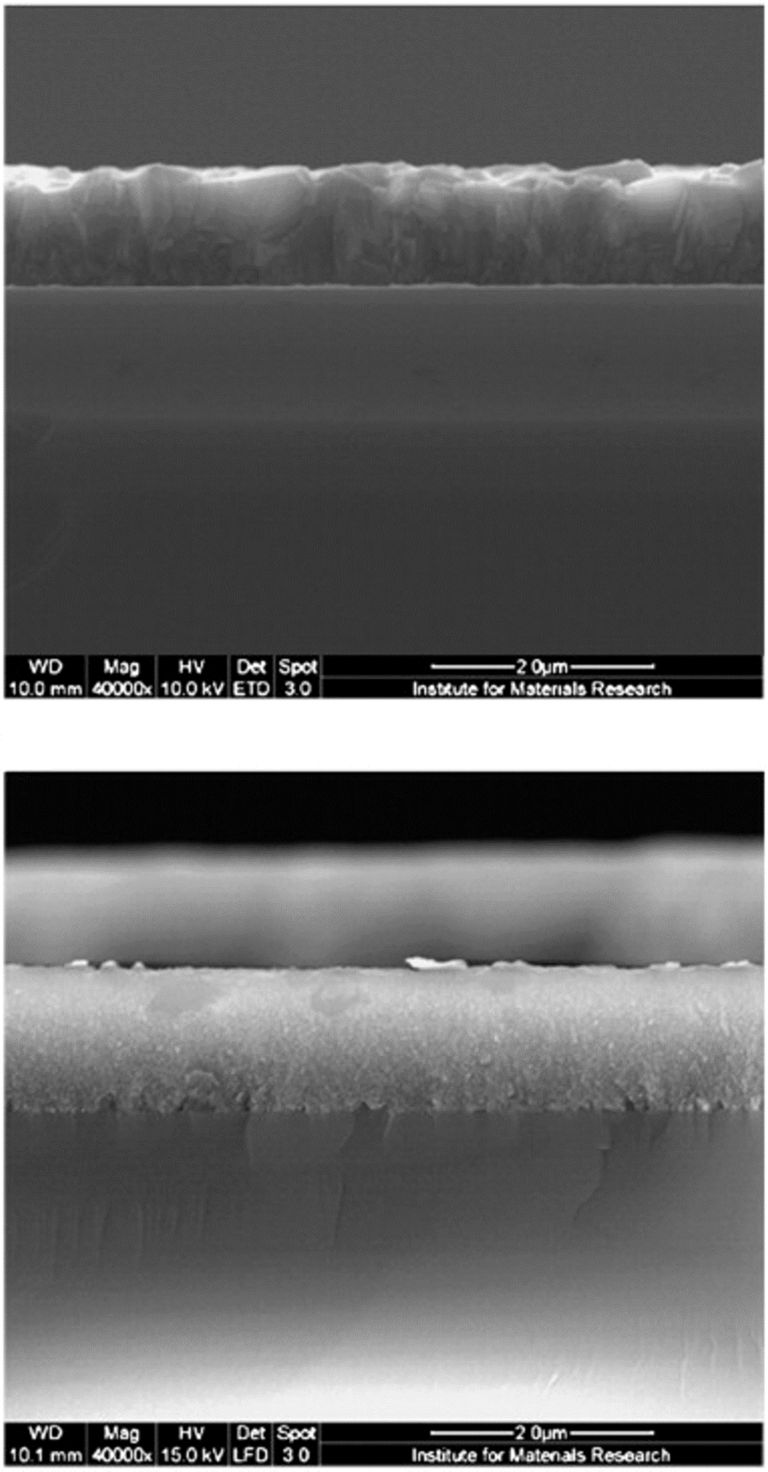

Figure 2.12: SEM cross sections of films grown with suppression (above) and enhancement (below) of re-nucleation processes. Reprinted from O. A. Williams et al., "Growth, electronic properties and applications of nanodiamond", Diamond and Related Materials, Proceedings of Diamond 2007, the 18th European Conference on Diamond, Diamond-Like Materials, Carbon Nanotubes, Nitrides and Silicon Carbide **17**, 1080–1088 (2008), © 2008, with permission from Elsevier.

Chapter 3

Experimental Methodology

This chapter provides a brief theoretical background of the experimental techniques used within this thesis. These include MPECVD, pyrometry, SE, laser and pyrometric interferometry, Raman spectroscopy, AFM, and finite element modelling.

3.1 Microwave Plasma-Enhanced Chemical Vapour Deposition

The MPECVD reactor (pictured in Figure 3.1) used for the growth of the diamond films in this thesis is a Carat SYstems CTS6U clamshell-type reactor, essentially a modified Seki (formerly ASTEX) 6500-series reactor. Microwaves are coupled into the chamber through a dielectric window from the underside of the reactor, with the dimensions of the chamber designed to allow only one microwave mode at 2.45 GHz. This design allows for the formation of a large plasma, and so is suitable for growth over large areas [42]. Substrates to be grown on are positioned within a molybdenum substrate holder atop a copper stage, with both the copper stage and reactor dome water-cooled. The pressure of the reactor is maintained using a rotary pump, with mass flow controllers used to regulate the ratio of feed gases. Film thickness can be monitored using SE and laser or pyrometric interferometry, with a dual-wavelength WilliamsonIR Pro 92 pyrometer used to monitor substrate temperature.

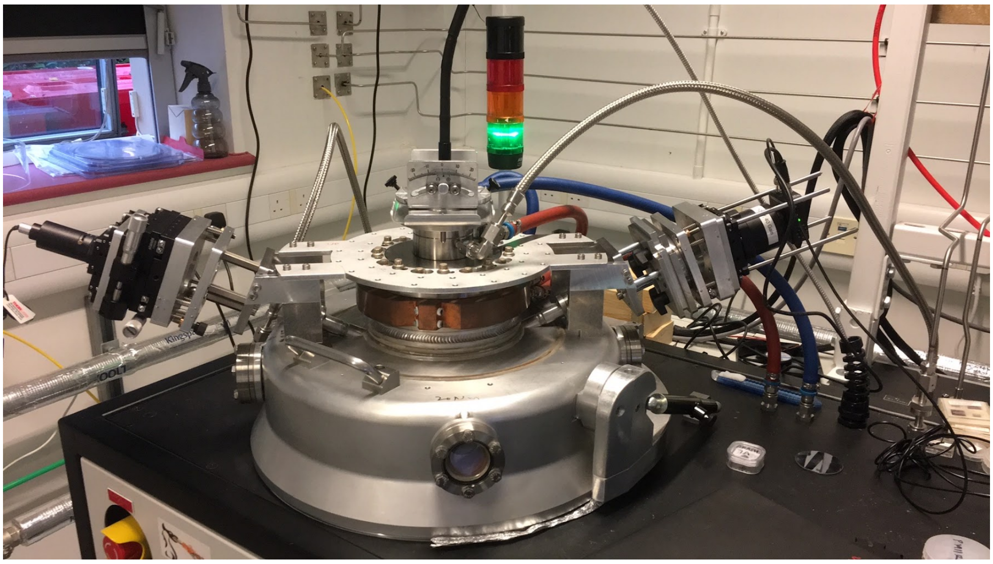

Figure 3.1: The MPECVD reactor used for growth of samples within this thesis.

3.2 Pyrometry

Transfer of heat occurs through three different processes: convection, conduction and radiation [70]. All matter with a temperature greater than absolute zero emits energy in the form of electromagnetic radiation, termed thermal radiation [71]. As the temperature of a body rises, the amount of heat emitted as thermal radiation increases. Objects at higher temperatures will often seem brighter, and this has been used as a crude estimation of an object's temperature for some time. In 1782, the potter Josiah Wedgewood noted that "red, bright red or white heat are indeterminate expressions" [72], and such methods are still used to this day by engineers and blacksmiths [70].

The thermal radiation emitted exhibits a dependence on wavelength, with the spectral emissive power E_λ used to describe the thermal radiation emitted by a surface per unit area [70]. For an ideal black body, the spectral emissive power can be calculated using Planck's law [73]:

$$E_{\lambda,b} = \frac{C_1}{\lambda^5[\exp(\frac{C_2}{\lambda T}) - 1]} \tag{3.1}$$

Where $E_{\lambda,b}$ is the spectral emissive power for a black body in W/m^3, λ is the wavelength in m, T is the temperature in K, and C_1 and C_2 are the first and second radiation constants respectively, equal to:

$$C_1 = 2hc^2 \qquad C_2 = \frac{hc}{k_B} \tag{3.2}$$

Where h is Planck's constant, c is the speed of light in the medium and k_B is the Boltzmann constant.

The maximum black body spectral emission for a particular temperature can be determined using Wien's displacement law [74]:

$$\lambda_{max}T = 0.028978 \text{ m K} \tag{3.3}$$

Figure 3.2 shows the variance of the spectral emissive power of a black body with wavelength over a range of temperatures, calculated from Planck's law.

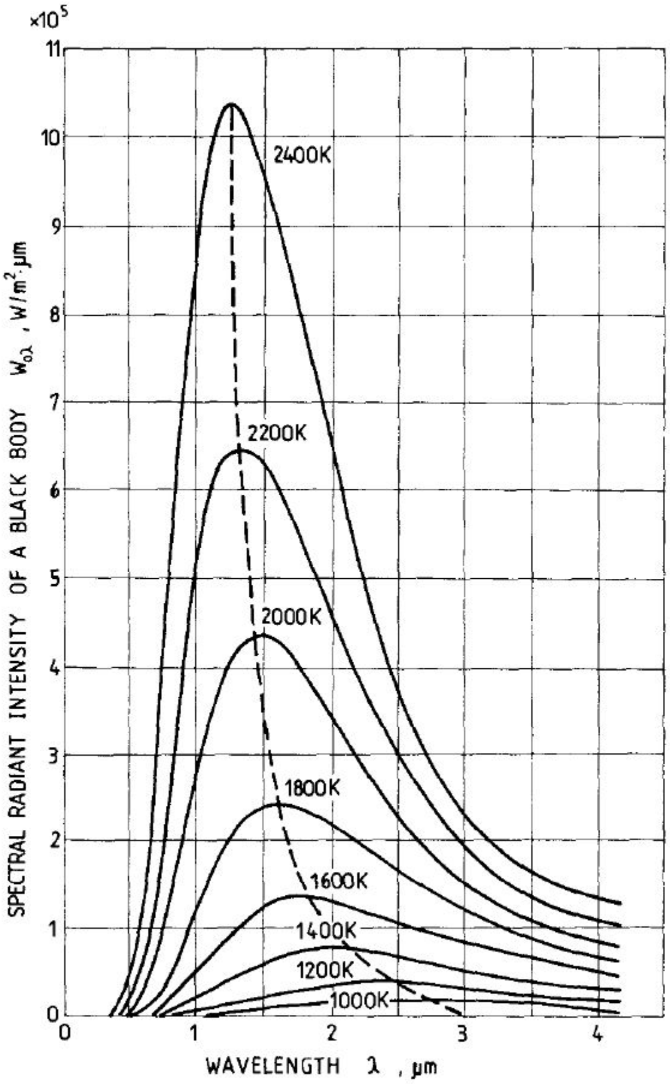

Figure 3.2: A plot of the spectral emissive power of a black body at various temperatures, calculated using Planck's Law. Reproduced with permission from [75], © 2001 John Wiley & Sons Ltd.

When used in infrared pyrometry, the value of the exponential term in Planck's law is much greater than 1. It is therefore possible to ignore the -1 term, an approximation known as Wien's law [70]:

$$E_{\lambda,b} = \frac{C_1}{\lambda^5[\exp(\frac{C_2}{\lambda T})]} \tag{3.4}$$

The approximation is generally valid for wavelengths below $5\lambda_{max}$.

The above equations can be used to calculate properties of radiation emitted from an ideal black body. Unfortunately these are only valid for an ideal black body, and therefore are of limited use for the non-ideal surfaces encountered in the real world. For real surfaces, the quantity of radiation emitted from a surface is a function of both the temperature and properties of the surface [70]. To fully describe non-black body surfaces, the concept of emissivity must be introduced. Emissivity (ε) is the property that governs the quantity of radiation emitted. It is defined as the ratio of electromagnetic flux emitted from a surface to the flux that would be emitted from an ideal black body at the same temperature, and can take a value from 0 to 1. This value is generally dependent on wavelength [76], so the spectral emissivity (ε_λ) is defined as the emissivity at a specific wavelength. Therefore, the spectral emissive power of a real surface differs from that of an ideal black body in both spectral distribution and magnitude. A surface that exhibits variation in in ε_λ with wavelength is known as a selective emitter [77]. Real bodies can also exhibit directionally-dependent properties, although it is often sufficient to assume that an emitting material is diffuse and that directional dependencies are negligible [70]. A material with spectral emissivity that is constant (but not equal to 1) for all wavelengths is known as a grey body [75]. Grey bodies can be used as an approximation for the behaviour of some real materials [77]. Figure 3.3 shows a comparison of the variance of emissive power with wavelength for a black body, grey body and a real object (selective emitter).

The first modern pyrometer was the disappearing filament pyrometer, invented independently in 1901 by Harmon Northrup Morse in the United States [79, 80] and Ludwig Holborn and Ferdinand Kurlbaum in Germany [81]. It was the first method to accurately measure temperatures above 1000 °C [82], and it it is possible for a skilled operator to achieve a resolution of 10 °C at temperatures up to 2000 °C [83]. This pyrometer uses the human eye as a spectrometer. It works using a lamp filament visible through the eyepiece, with a target in the background (figure 3.4). The current of the filament is adjusted, changing its temperature, until the filament is no longer visible against the background of the target. If both the filament and target are black bodies, then they will have the same temper-

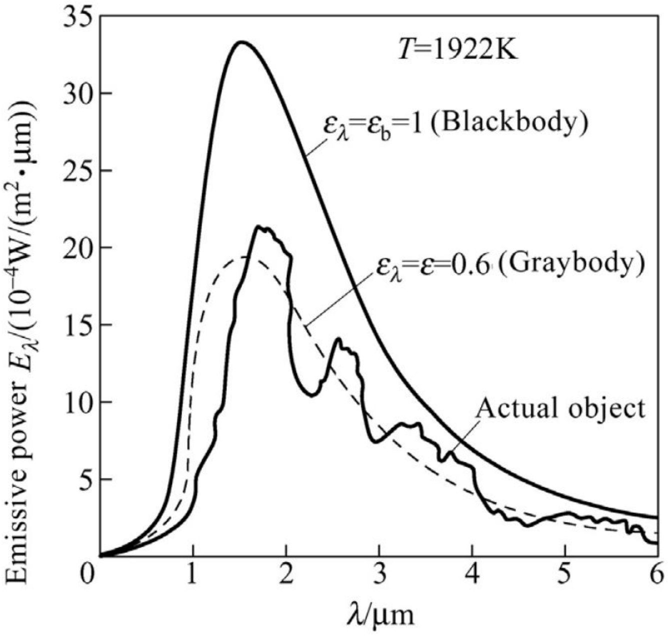

Figure 3.3: The relation of emissive power to wavelength of a black body, grey body and a real object (selective emitter). Reproduced from [78] with permission from Elsevier.

ature. In practice, a disappearing filament pyrometer sighted upon a non-black body surface will return a temperature lower than the true temperature of the body [83]. Therefore, calibration for the emissivity of the surface is required for accurate measurement.

The red filter in a disappearing filament pyrometer acts to restrict the measured region of the spectrum to a narrow band. Figure 3.5 shows the response of the human eye and the transmittance of a red filter. The reduced sensitivity of the human eye to red light acts as a long wavelength cutoff, whilst the filter prevents transmission of light at a lower wavelength [84]. Measurements of higher temperatures can be taken by the inclusion of a grey absorbing filter in the design. Disappearing filament pyrometers have been largely superseded by other types of pyrometer, such as the single-colour pyrometer [84].

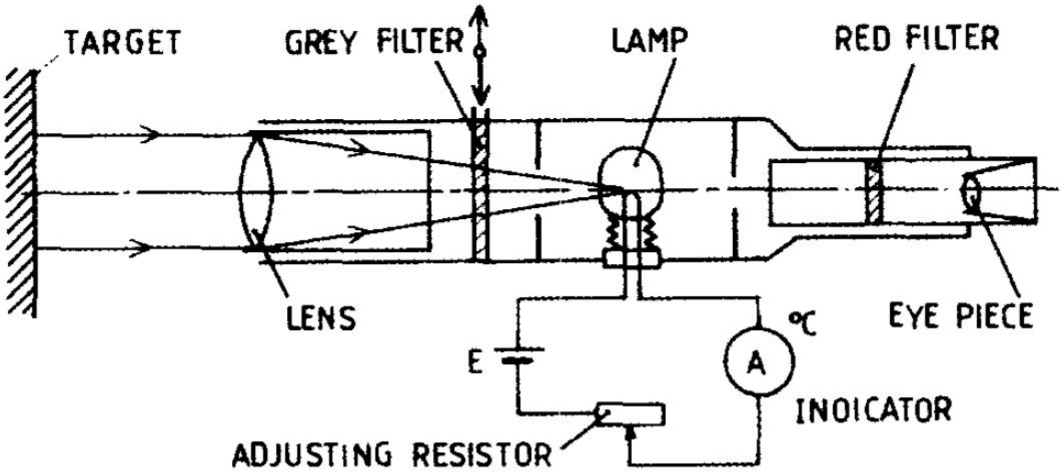

Figure 3.4: A disappearing filament pyrometer. The current of the filament is adjusted using the resistor, changing its temperature, until the filament is no longer visible against the background of the target. Reproduced with permission from [75], © 2001 John Wiley & Sons Ltd.

A single-colour pyrometer uses a rearranged form of Wien's approximation to determine the temperature of a sample.

$$T = \frac{C_2}{\ln\left(\frac{C_1 \varepsilon_\lambda}{\lambda^5 I_\lambda}\right)} \tag{3.5}$$

Where λ is the effective wavelength of the pyrometer. The disadvantage of this form of pyrometry is that the emissivity of the substrate must be known. The dual-wavelength pyrometer, also known as ratio or two-colour, overcomes this issue by measuring radiation emitted at two fixed spectral bands (effective wavelengths λ_1 and λ_2). The ratio of emitted radiation at each spectral band R_{12} is given by:

$$R_{12} = \frac{\varepsilon(\lambda_1)\lambda_2^5[\exp(\frac{C_2}{\lambda_2 T}) - 1]}{\varepsilon(\lambda_2))\lambda_1^5[\exp(\frac{C_2}{\lambda_1 T}) - 1]} \tag{3.6}$$

If the temperature of the target is sufficiently low, $\exp(\frac{C_2}{\lambda T})$ will be significantly greater than 1, so the -1 term can be ignored:

$$R_{12} = \frac{\varepsilon(\lambda_1)\lambda_2^5[\exp(\frac{C_2}{\lambda_2 T}) - 1]}{\varepsilon(\lambda_2))\lambda_1^5[\exp(\frac{C_2}{\lambda_1 T} - 1]} = \frac{\varepsilon(\lambda_1)\lambda_2^5}{\varepsilon(\lambda_2)\lambda_1^5} \exp\left(\frac{C_2}{\lambda_2 T} - \frac{C_2}{\lambda_1 T}\right) \tag{3.7}$$

Assuming the emissivity at both wavelengths is the same, the measurement will

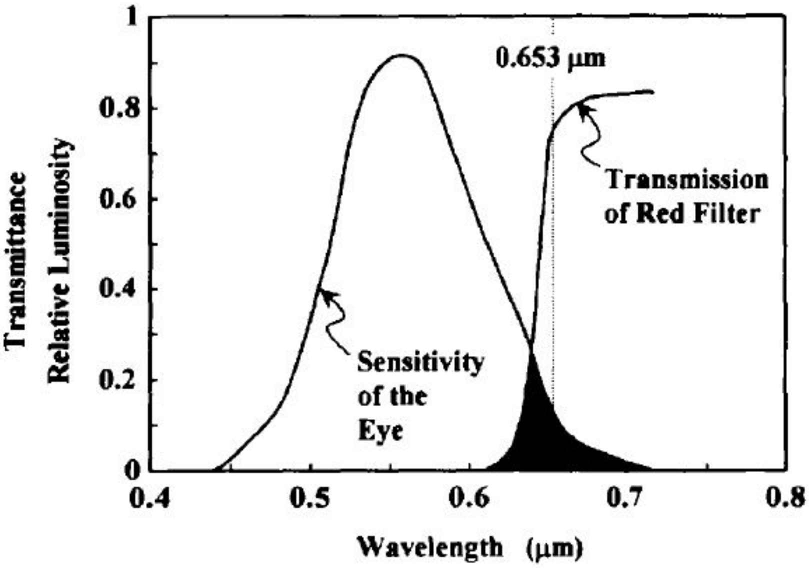

Figure 3.5: The combination of the response of the human eye and the transmittance of a red filter restricts the detected region of the spectrum to a narrow band. Reproduced with permission from [84], © 1998 John Wiley & Sons Ltd.

become independent of surface emissivity:

$$R_{12}\left(\frac{\lambda_1}{\lambda_2}\right)^5 = \exp\left(C_2\left(\frac{\lambda_1-\lambda_2}{\lambda_1\lambda_2 T}\right)\right) \tag{3.8}$$

This can be rearranged to give:

$$T = \frac{C_2(\lambda_2-\lambda_1)}{\lambda_1\lambda_2\left(5\ln\left(\frac{\lambda_1}{\lambda_2}\right) - \ln(R_{12})\right)} \tag{3.9}$$

Whilst dual-wavelength pyrometers reduce the uncertainty in emissivity, they are less sensitive than spectral band pyrometers [70].

3.3 Spectroscopic Ellipsometry

SE involves the irradiation of a sample with polarised light at angles close to the Brewster angle (Figure 3.6). The optical constants, film thickness and microstructure of the sample can be derived from the changes in polarisation state caused by the reflection or transmission of light [85]. When a sample is probed with polarised light, reflection coefficients from the perpendicular (s) and parallel (p) components of the light can generated by rewriting Fresnel equations using Snell's law:

$$r_s \equiv \frac{E_{rs}}{E_{is}} = \frac{\cos\theta_i - (N_{ti}^2 - \sin\theta_i)^{\frac{1}{2}}}{\cos\theta_i + (N_{ti}^2 - \sin\theta_i)^{\frac{1}{2}}} = \mid r_s \mid e^{i\delta_{rs}} \tag{3.10}$$

$$r_p \equiv \frac{E_{rp}}{E_{ip}} = \frac{N_{ti}^2\cos\theta_i - (N_{ti}^2 - \sin\theta_i)^{\frac{1}{2}}}{N_{ti}^2\cos\theta_i + (N_{ti}^2 - \sin\theta_i)^{\frac{1}{2}}} = \mid r_p \mid e^{i\delta_{rp}} \tag{3.11}$$

Where $\mathrm{E_{is}}$ and $\mathrm{E_{ip}}$ are the electric fields of the s and p components of the incident light respectively, $\mathrm{E_{rs}}$ and $\mathrm{E_{rp}}$ are the electric fields of the s and p components of the reflected light, θ_i is the angle of incidence relative to the normal, and $\mathrm{N_{ti}}$ is the ratio of the complex refractive indices of the sublayer and incident materials [85].

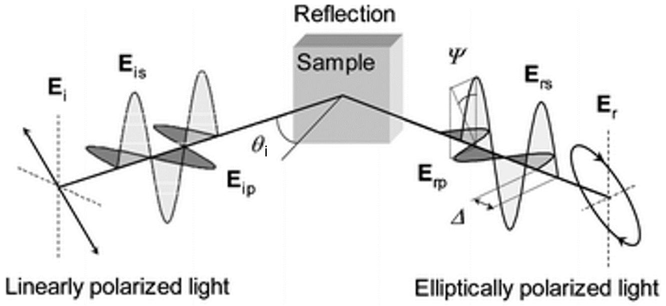

Figure 3.6: The changes in polarisation state upon reflection of linearly polarised light. Reproduced from [86] with permission of The Royal Society of Chemistry.

The two measured values in SE are delta (Δ) and psi (Ψ). When polarised light reflects form a surface, a phase shift can occur. This phase shift is not always the same for both p and s components of the light. The parameter Δ is defined as:

$$\Delta = \delta_1 - \delta_2 \tag{3.12}$$

Where δ_1 is the phase difference between p and s components prior to reflection, and δ_2 is the phase difference after reflection. Delta, therefore, is the phase shift caused by reflection, and can take values from -180° to +180° [87]. In addition to this phase shift, reflection results in a reduction in amplitude for both p and s components, and as before this is not the same for both. The quantity Ψ is defined as:

$$\tan\Psi = \frac{\mid r_p \mid}{\mid r_s \mid} \tag{3.13}$$

Where r_p and r_s are the total reflection coefficients of the p and s components respectively. Ψ is therefore the angle whose tangent is the ratio of the magnitudes of the total reflection coefficients. It is a real number and can range in value from 0° to 90° [85]. The quantity rho (ρ) is defined to be the complex ratio of the total reflection coefficients:

$$\rho = \frac{r_p}{r_s} \tag{3.14}$$

The fundamental equation of ellipsometry is:

$$\rho = \tan \Psi e^{i\Delta} = \frac{r_p}{r_s} \tag{3.15}$$

$\tan \Psi$ is the magnitude of ρ, and the exponential function is the phase shift [85]. The quantities Δ and Ψ are directly measured by the ellipsometer, and so these are always correct if the instrument is functioning correctly. As the measurement is of the change in polarisation state and not intensity of the reflected light, the measurement is possible even when there is a bright background [12]. The physical characteristics of the sample are derived from a comparison between simulated and measured values of Δ and Ψ. An iterative fitting process is typically used, with potential samples tructures varied to improve the Mean Square Error (MSE) between measured and modelled spectra. Regression analysis is typically employed to determine the combination of model parameters that results in the lowest MSE. It is important to note that the quality of the derived parameters is entirely dependent on the quality of the model employed.

Modern spectroscopic ellipsometers typically employ a xenon arc lamp to produce unpolarised white light. This beam is then collimated an linearly polarised so that $E_{ip} = E_{is}$. The beam is used to irradiate the beam at an angle close to the Brewster angle. The reflected beam, with altered Δ and Ψ, passes through a compensator and analyser (with one of the two rotating), before being separated by wavelength and measured by a charge-coupled device detector [87]. A schematic of a rotating compensator ellipsometer is shown in Figure 3.7.

Whilst in theory the light reflected from the sample will be perfectly elliptically polarised, in practice depolarisation can be introduced by imperfections in ei-

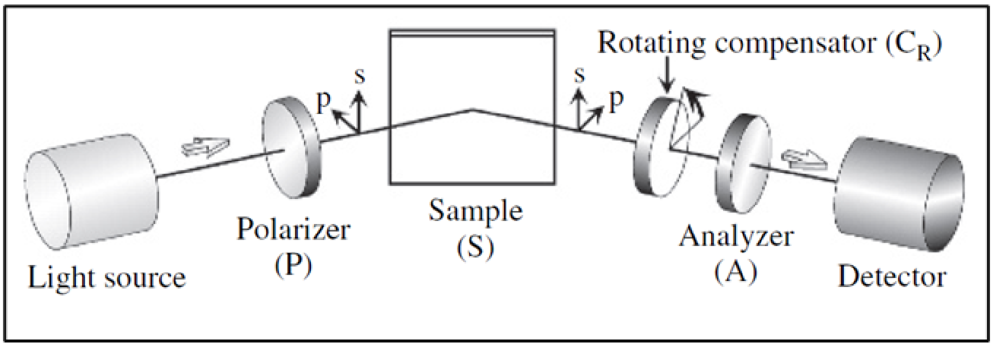

Figure 3.7: A typical experimental setup for spectroscopic ellipsomety, showing a rotating compensator instrument. Reproduced with permission from [85], © 2007 John Wiley & Sons Ltd.

ther the sample or the instrument [85]. The Stokes parameters can be used to fully characterise all possible degrees of polarisation, from fully unpolarised to completely polarised light. These are often mathematically represented in vector form, termed the Stokes vector:

$$\begin{bmatrix} S_0 \\ S_1 \\ S_2 \\ S_3 \end{bmatrix} = \begin{bmatrix} 1 \\ -p\cos 2\Psi \\ p\sin 2\Psi\cos\Delta \\ -p\sin 2\Psi\sin\Delta \end{bmatrix} \tag{3.16}$$

S_0 is the total light intensity, whilst the parameters S_{1-3} are representative of the relative difference in light intensity between the different states of polarisation: S_1 is the difference in intensity between light linearly polarised in the x direction (horizontal) and light linearly polarised in the y direction (vertical); S_2 is the difference in intensity between light polarised at +45° and light polarised at -45°; S_3 is the difference in light intensity between the left circular polarisation and the right circular polarisation. p is the degree of polarisation given by:

$$p = \frac{(S_1^2 + S_2^2 + S_3^2)^{\frac{1}{2}}}{S_0} \tag{3.17}$$

For totally polarised light, p is equal to 1, whereas for totally unpolarised light it is equal to 0 [85].

3.4 Laser and Pyrometric Interferometry

A slightly simpler technique than spectroscopic ellipsometry frequently used for in-situ monitoring of diamond film growth is interferometry. As shown in Figure 3.8, the intensity of a laser reflected from a substrate during diamond growth will oscillate due to constructive and destructive interference from the growing film. The growth rate of the film can be determined from the period of oscillations using the following equation [7, 88]:

$$R = \frac{1}{T} \times \frac{\lambda}{2n\cos\theta} \tag{3.18}$$

Where R is the growth rate, T is the period of oscillations, λ is the wavelength of the laser used, θ is the angle of incidence, and n is the refractive index of the diamond film. Over time, the intensity of the signal will decrease due to scattering from the increasing diamond film roughness with growth duration [7, 88].

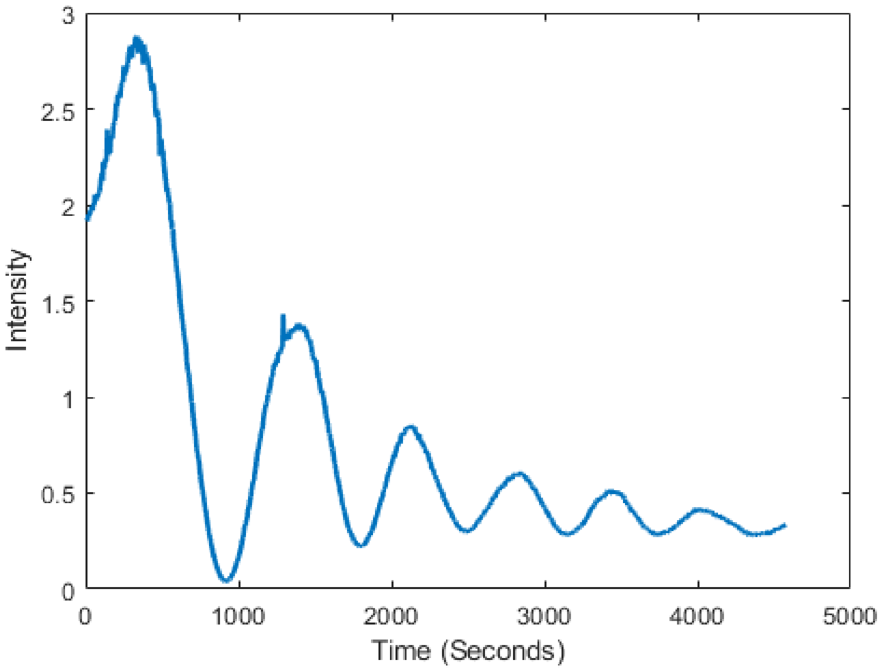

Figure 3.8: Intensity of a laser reflected from a silicon substrate during diamond film growth, showing fluctuating intensity due to interference.

Interference caused by changing thicknesses of the film will also influence the apparent temperature of the substrate measured by a pyrometer, [6, 89]. This can be used to measure the growth rate, and if a dual-wavelength pyrometer is used the growth rate can be determined using [6]:

$$R = \frac{(\lambda_1 + \lambda_2)\cos\theta}{4nT} \tag{3.19}$$

Where λ_1 and λ_2 are the two wavelengths of the pyrometer.

3.5 Raman Spectroscopy

When intense monochromatic light is incident upon a sample, the electric field of the radiation distorts electron clouds making up chemical bonds of the sample, absorbing energy. As the field reverses, the distorted electron clouds relax, releasing this absorbed energy as radiation. The majority of this is emitted at the same energy as the incident light, a phenomenon known as Rayleigh scattering [90, 91]. A fraction of the absorbed energy excites vibrational modes within the sample, resulting in a small re-emission at lower energies than the incident light [92]. This is termed Stokes scattering. The difference in energy between the Rayleigh and Stokes bands is directly related to the vibrational energies of the sample [90]. It is also possible for the opposite to occur, with a decrease in vibrational energy within the sample resulting in re-emission at greater energies than the incident light (anti-Stokes scattering). As this phenomenon is due to existing vibrational states within the sample, its intensity is heavily dependent on the temperature of the sample. Stokes scattering, on the other hand, is only mildly temperature-dependent. As a result of this, anti-Stokes scattering is not commonly measured in Raman spectroscopy [90]. Figure 3.9 shows energy level diagrams for the different kinds or scattering.

Whilst the original experiments by the Indian physicist C. V. Raman in 1928 used a mercury lamp as an excitation source [94], most modern experiments use a laser for this purpose. Typical wavelengths employed include 514, 633, and 780 nm [95]. Scattered light is typically separated by a grating and collected by a detector to form a spectrum. With the degree of scattering directly related to the vibrational energies of the bonds in a sample, Raman spectroscopy can be used

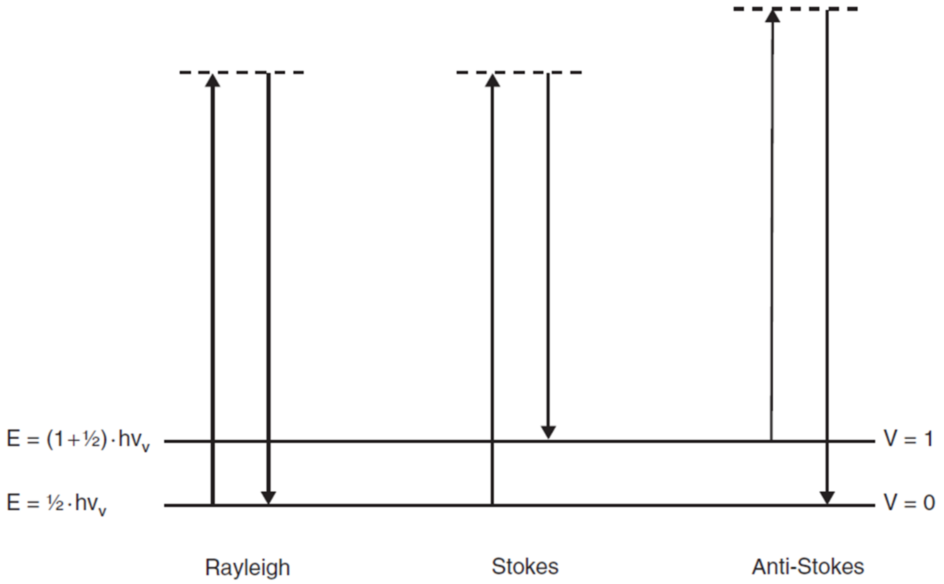

Figure 3.9: Model for the dispersion of light by molecules, showing different kinds of scattering. Reproduced with permission from [93], © 2013 John Wiley & Sons Ltd.

to determine the forms of carbon present within a diamond film [8, 9, 96].

3.6 Atomic Force Microscopy

First developed by Binnig in 1986 [97], AFM is a high-resolution technique for surface imaging. Typically, areas imaged are under 150 × 150 μm with maximum surface roughness on the order of 10-20 μm [98]. The technique involves the scanning of the nanometre-sharp tip of a cantilever across the surface of a sample. As the tip experiences forces, the cantilever will deflect in accordance with Hooke's law. This is typically measured by reflecting a laser off the top of the cantilever, with movement of the laser spot tracked using a four-quadrant photodiode (Figure 3.10).

AFM is typically used in one of three regimes, shown in Figure 3.11 [100, 101]. The simplest of these is contact mode, where the tip is pressed against the surface of the sample and experiences repulsive forces. This is operated in one of two ways. The first, constant force, is where a feedback loop operates to maintain a constant distance from the sample, with the change in height of the tip recorded

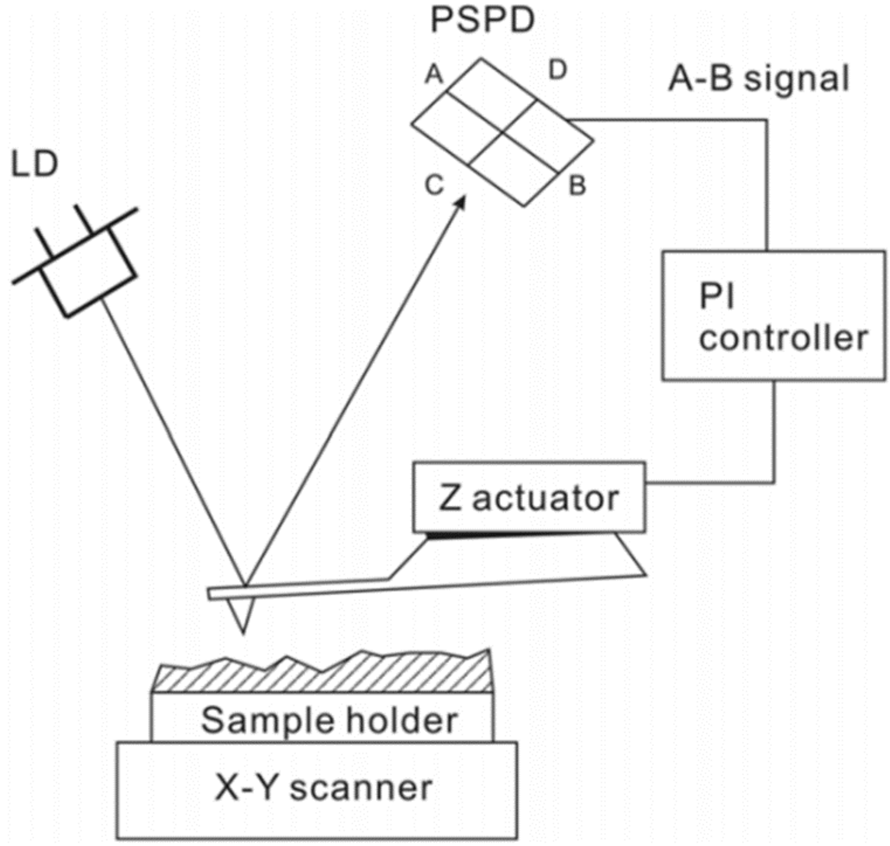

Figure 3.10: Typical AFM experimental setup. A laser beam is focused at the end of the cantilever, and a reflected beam is aligned at the center of the four-quadrant photodiode. When the cantilever bends, the A–B signal of the PSPD is changed and fed to the controller to control the height of the cantilever through the Z-actuator. Reproduced with permission from Y. Seo and W. Jhe, "Atomic force microscopy and spectroscopy", Reports on Progress in Physics **71**, 016101 (2007). © IOP Publishing. All rights reserved.

to measure the topography of the sample. The second is variable force, where no feedback loop is employed and deflection of the tip is measured as it is dragged across the sample. This only possible for smooth samples, as roughness can result in damage to the tip. Whilst contact mode can produce a high resolution, it can also result in damage to the sample, and frictional or adhesive forces between the sample and tip produce image artefacts.

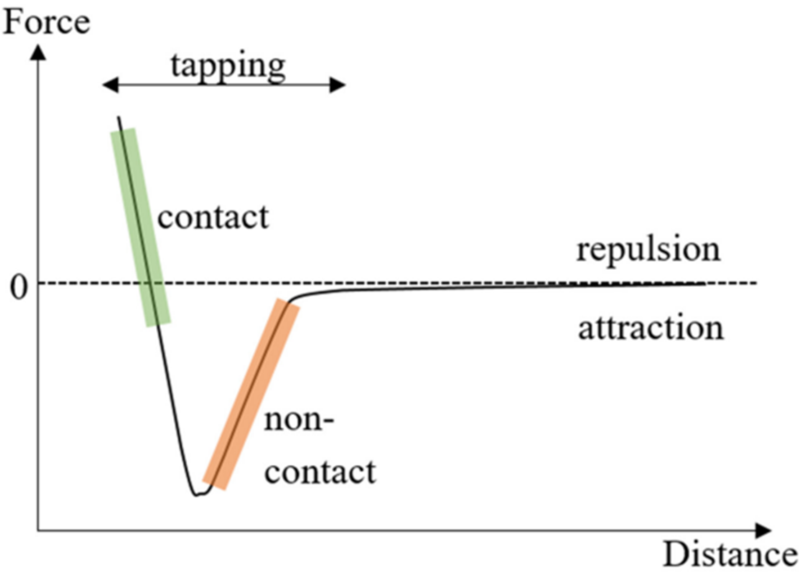

Figure 3.11: Schematic of the force experienced by the tip as a function of distance from the surface. As the tip moves into contact, there is a shift from attractive to repulsive forces. The three imaging regimes are defined by which area of this curve the measurement is operating in. Reproduced with permission of IOP Publishing through PLSclear from K. Morrison, *Characterisation Methods in Solid State and Materials Science* (IOP Publishing, Oct. 2019). © IOP Publishing Ltd 2019.

Non-contact mode is where the probe is positioned at a greater distance from the sample, with long-range attractive forces causing deflection of the tip. The tip is oscillated at its resonant frequency, with the small deflections caused by these forces resulting in a shift in amplitude. The comparatively weak forces experienced by the tip in this mode result in a limited resolution, although the risk of damage to the sample or tip is eliminated [102].

The final mode of operation is tapping mode. In this mode, the cantilever is oscillated at a greater amplitude than in non-contact mode, with the tip coming into contact with the sample. This contact results in a reduction in amplitude of the oscillations. This mode minimises the loss of resolution in comparison to contact mode, whilst exerting less force on the sample; whilst contact mode typically exerts forces of 1-100 nN on the sample [102], the forces produced by tapping mode are on the order of 0.1 nN [103], reducing the chances of damage to the tip or sample.

3.7 Finite Element Modelling

The laws of physics are often described by partial differential equations. For more complex systems, it is generally not possible to obtain exact solutions [104]. The finite element method is a computational method used to obtain approximate solutions. Figure 3.12a shows an example of a two-dimensional field variable ϕ(x,y) defined by a known equation. Figure 3.12b shows a triangular finite element within the field. The vertices of this element are termed nodes; specific points within the finite element where it is possible to calculate the value of the field variable. Further triangular elements can be added to this to form a mesh, shown in Figure 3.12c. In finite element analysis, the values of the modelled variables are computed only at nodes, with interpolation used to approximate the values at points between the nodes [105] The size of the mesh used must be carefully chosen for a particular problem, as whilst a smaller mesh size will result in a more accurate solution, a smaller mesh will have more nodes and therefore the simulation will be more computationally intensive. The convergence of simulated values and the exact physical solution can be evaluated by increasing the number of nodes and observing how this impacts the values obtained by the simulation [105].

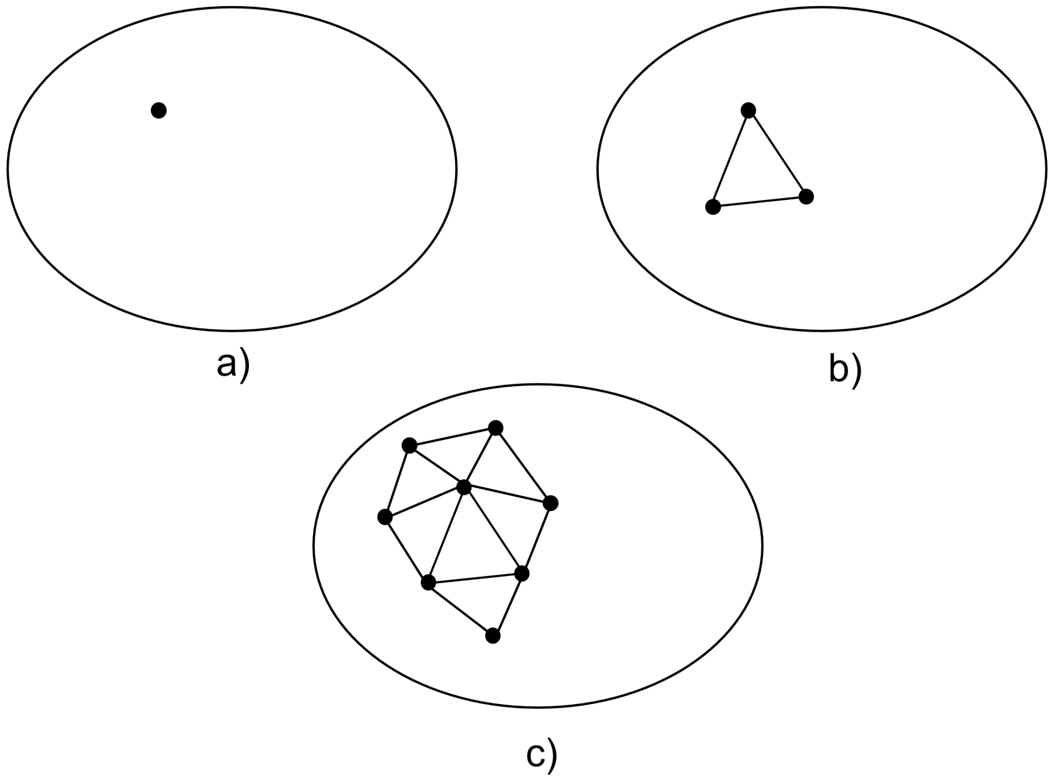

Figure 3.12: (a) A general two-dimensional domain of field variable ϕ(x,y). (b) A three-node finite element within the domain. (c) Addition of further elements forming a partial finite element mesh of the domain.

Chapter 4

Substrate Temperature Mapping During Diamond Growth

The substrate temperature during (MPECVD) diamond growth has a significant influence on the properties of the deposited film. Therefore, a non-uniform substrate temperature will result in the growth of an inhomogeneous film, presenting issues for the scalability of MPECVD diamond growth. This chapter reviews the effect of substrate temperature on diamond film properties (section 4.1), as well as existing methods for evaluating substrate temperature during growth (section 4.2), before describing experimental work developing a technique employing a dual-wavelength pyrometer coupled with a mirror galvanometer to map the substrate temperature during MPECVD diamond growth (section 4.3). Temperature maps generated are compared to plasma electron densities simulated using a finite element model, as well as the properties of nanocrystalline diamond films mapped using *ex-situ* Raman spectroscopy and SE.

This chapter is adapted from the manuscript published in [4].

4.1 Effects of Substrate Temperature on Diamond Film Properties

Along with methane concentration, substrate temperature is a hugely important parameter for nanocrystalline diamond growth by MPECVD. Typical substrate temperatures for nanocrystalline diamond growth by MPECVD are within the range of 700-900 °C [51]. Whilst low-temperature growth has been reported (in one case as low as 150 °C [106]), the quality of such material is often poor when compared to that grown at high temperatures, with the low growth rates at extremely low temperature often impractical [51].

Several SE studies have evaluated the level of sp^2 content within the film with varying growth temperature. Windischmann et al. grew several diamond films at temperatures between 600-900 °C, finding that the sp^2 fraction measured by SE decreased with increasing substrate temperature. Additionally, the level of intrinsic stress increased with deposition temperature, which was attributed to the lower levels of sp^2 content. The trends of these properties with temperature can be seen in Figure 4.1. *In-situ* SE study by Hong et al [2] indicated that increasing the substrate temperature from 626 °C to 841 °C reduced the peak sp2 fraction formed during coalescence from 45% of the bulk layer volume to 20%.

Similar observations have been seen in Raman spectroscopy. Fortunato et al. [108] grew a series of diamond films by MPECVD at substrate temperatures between 786-906 °C. Spectra (shown in Figure 4.2 were evaluated using the diamond/ graphite ratio (to evaluate phase purity), as well as the Full Width at Half Maximum (FWHM) (to evaluate crystalline quality). It was found that the highest phase purity and crystalline quality increased with increasing substrate temperature. The growth rate of diamond films has also been shown to vary with substrate temperature. Lee et al. [109] used real-time SE to measure the thickness of diamond layers grown by MPECVD on silicon at substrate temperatures between 461-841 °C, finding that the growth rate significantly increased with increasing substrate temperature (Figure 4.3).

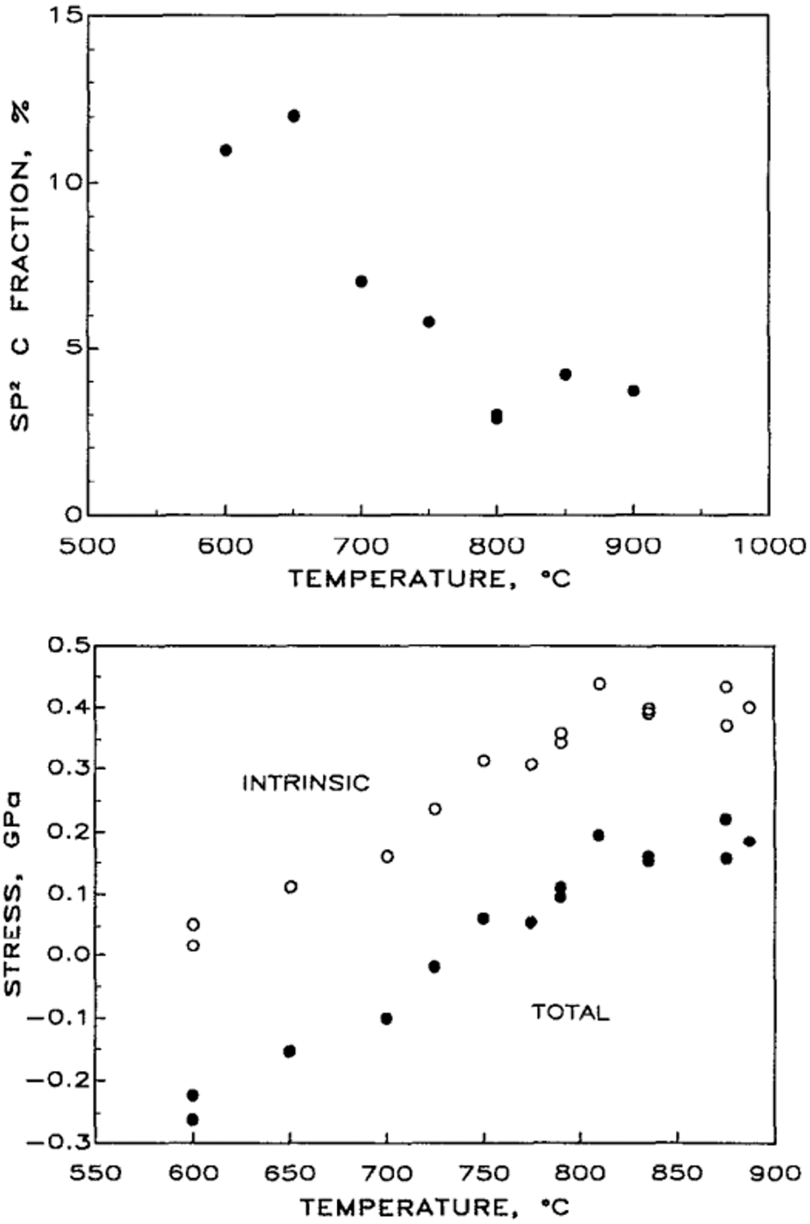

Figure 4.1: Top: Variation of absorbing sp² C fraction incorporated in diamond film on deposition temperature, measured by SE. Bottom: Total and intrinsic stress variation with deposition temperature. Used with permission of the American Institute of Physics, from H. Windischmann et al., "Intrinsic stress in diamond films prepared by microwave plasma CVD", Journal of Applied Physics **69**, 2231–2237 (1991). Permission conveyed through Copyright Clearance Center, Inc.

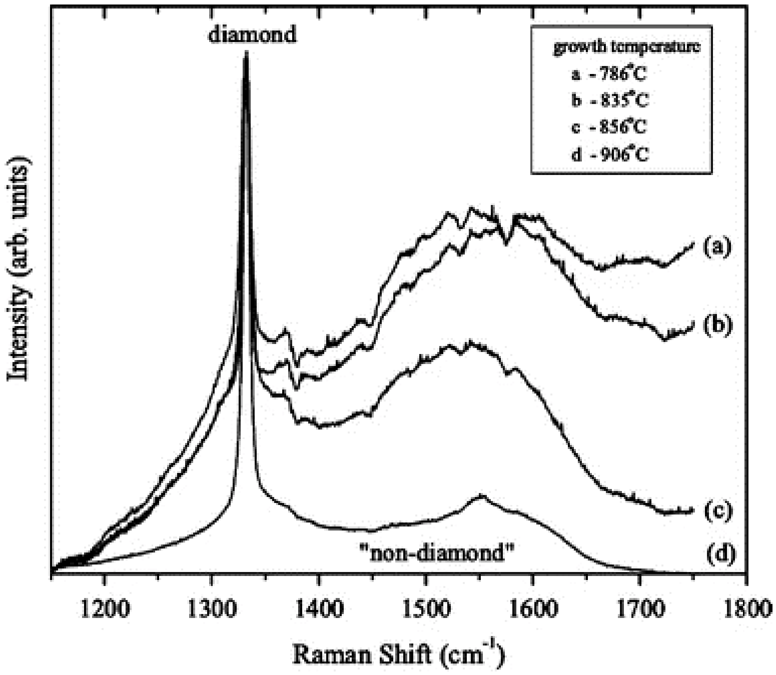

Figure 4.2: *Ex-situ* Raman spectra of samples grown by MPECVD at various deposition temperatures. Reproduced with permission from Springer Nature from [108].

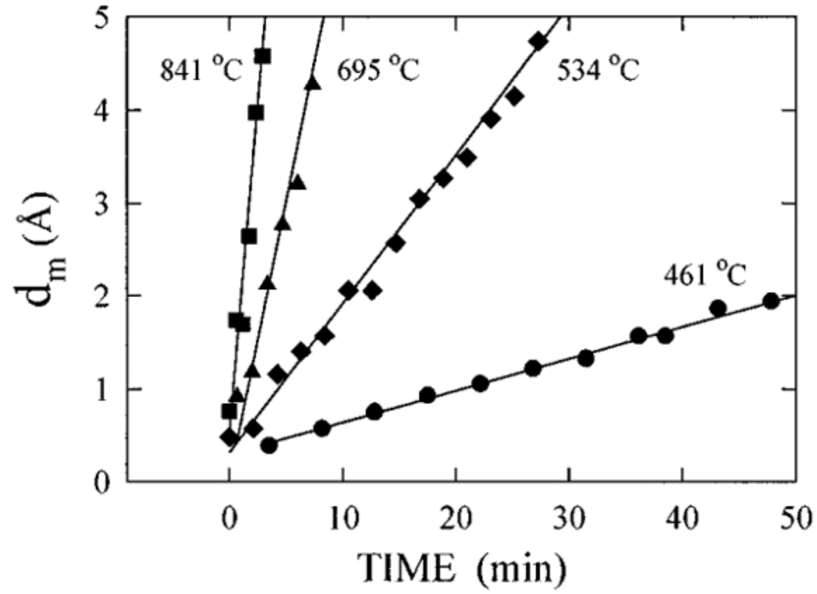

Figure 4.3: Diamond mass thickness, defined as the physical thickness times the diamond volume fraction, plotted vs time during nucleation for diamond films prepared on separate seeded Si wafers at selected temperatures. Used with permission of the American Institute of Physics, from J. Lee et al., "Nucleation and bulk film growth kinetics of nanocrystalline diamond prepared by microwave plasma-enhanced chemical vapor deposition on silicon substrates", Applied Physics Letters **69**, 1716–1718 (1996). Permission conveyed through Copyright Clearance Center, Inc.

4.2 Substrate Temperature Measurement During Diamond Growth

With such variance in film properties with substrate temperature during growth, it is clearly of great interest to be able to measure this. Thermocouples have frequently been used to attempt to measure the substrate temperature under growth conditions [107, 110–112]. In HFCVD growth, these can be placed atop the substrate. Such an approach was employed by Zimmer et al., who used 12 thermocouples bonded to the surface of a silicon wafer to measure the substrate temperature uniformity during growth, with observed temperature variations corresponding with the non-uniformity of film thickness (Figure 4.4). Whilst slightly limited by the small number of points at which the temperature is measured, this approach is undeniably useful. Unfortunately, the harsh plasma environment during MPECVD diamond growth makes it impractical to place thermocouples on the surface of the substrate. It is possible to avoid this issue by placing them on the back of the substrate, but this presents its own problems as it results in thermocouples sitting between the substrate and water-cooled stage, adding a significant source of uncertainty in the temperature measurement.

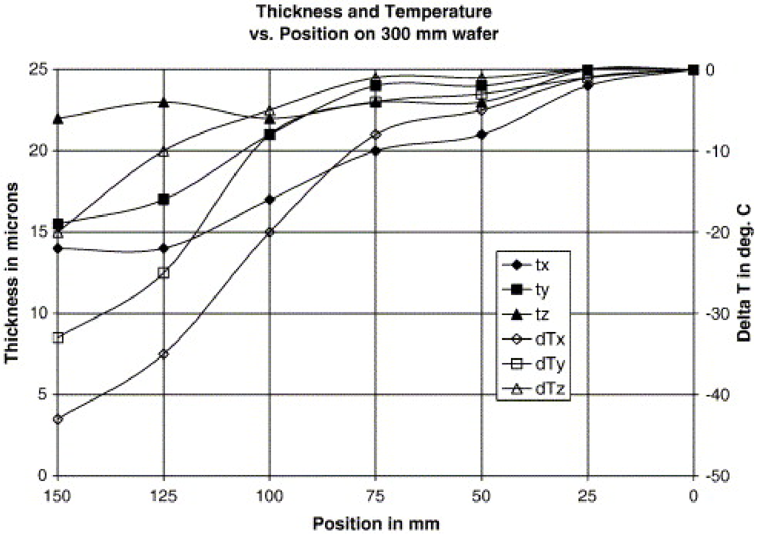

Figure 4.4: Film thickness (t) and corresponding radial temperature deviation (dT) for three different reactor configurations. tx, ty and tz are film thicknesses for three different reactor configurations with the corresponding radial temperature deviations (dTx, dTy and Tz). Reproduced with permission from Elsevier from [110]. © 2005 Elsevier BV.

The limitations of the thermocouple method mean that the predominant substrate temperature measurement technique during MPECVD is pyrometery, typically single colour or dual-wavelength. A more detailed background of the theory of thermal radiation can be found in Chapter 3, so only a brief overview will be included here. Single-colour pyrometers determine the temperature of a sample using Wien's approximation:

$$T = \frac{C_2}{\ln\left(\frac{C_1 \varepsilon_\lambda}{\lambda^5 I_\lambda}\right)} \tag{4.1}$$

where T is the temperature of the sample, C_1 and C_2 are the first and second radiation constants, I_λ is the intensity of the sample at the effective wavelength of the pyrometer λ, and ε_λ is the emissivity of the sample at wavelength λ. The use of pyrometry does produce some additional sources of uncertainty; the effective wavelength must be carefully selected in order to avoid emission from the plasma, and windows can result in absorbance of the emitted radiation from the substrate, particularly if dirty. Even so, it is possible to use single-wavelength pyrometry to both measure the substrate temperature and evaluate its uniformity during growth. With the emissivity of a single-colour pyrometer set to 0.6, Zuo et al. [113] investigated the temperature uniformity in a MPECVD reactor consisting of a 2.45 GHz cavity applicator inside a 12 cm diameter fused silica bell jar, probing temperature variation at a range of microwave power and chamber pressure conditions. It was found that both temperature variation and absolute temperature at the centre of the substrate increased with increasing power and pressure (Figure 4.5).

However, this method has a further disadvantage as a result of its dependence on the emissivity of the substrate. The changes in emissivity of the substrate seen during the growth process can result in significant errors in the measured temperature [114, 115]. The problem of changing emissivity can be circumvented by employing a dual-wavelength (or two-colour) pyrometer. This uses readings at two different wavelengths to determine the substrate temperature, which is mea-

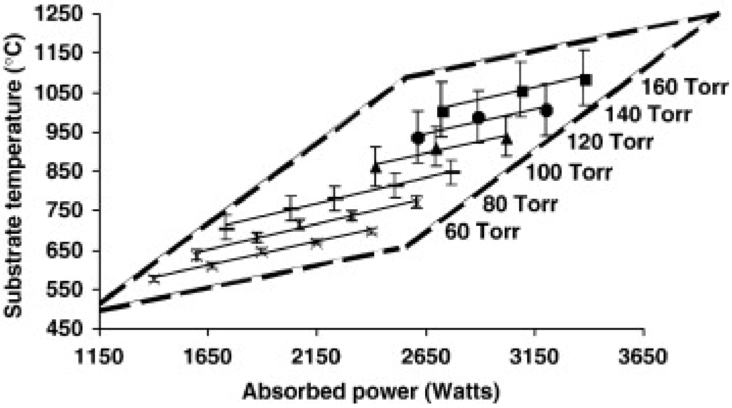

Figure 4.5: Substrate center temperature vs. pressure and absorbed microwave power for the deposition plasma without argon. The vertical bars represent the minimum/maximum variation of temperature across a 75 mm diameter wafer. Reproduced with permission of Elsevier from [113]. © 2008 Elsevier BV.

sured using the ratio of the two intensities R_{12}:

$$T = \frac{C_2(\lambda_2 - \lambda_1)}{\lambda_1\lambda_2\left(5\ln\left(\frac{\lambda_1}{\lambda_2}\right) - \ln(R_{12}) + ln\left(\frac{\varepsilon_1}{\varepsilon_2}\right)\right)} \tag{4.2}$$

Assuming the emissivity at the two wavelengths used is the same, the emissivity term will equal zero and therefore temperature measurement becomes independent of emissivity:

$$T = \frac{C_2(\lambda_2 - \lambda_1)}{\lambda_1\lambda_2\left(5\ln\left(\frac{\lambda_1}{\lambda_2}\right) - \ln(R_{12})\right)} \tag{4.3}$$

Such an approach was employed by Mallik et al. [116, 117] to investigate the substrate temperature uniformity in a MPECVD reactor, with a dual-wavelength pyrometer used to measure the substrate temperature across nine different points of the substrate (Figure 4.6). Figure 4.7 shows the variation in substrate temperature with the change in reactor parameters. It was found that changes in microwave power, chamber pressure, stage height, and short position had a significant impact in plasma uniformity, whilst the methane fraction did not have as significant an impact on temperature distribution. Differences in thickness observed using cross-section SEM correlated with the observed temperature gradient, whilst Raman spectra did not appear to correlate with growth temperature. Whilst the insight of this work is obvious, it is somewhat limited by the small number of points of the substrate measured; with only three points from edge to edge of the wafer in any particular axis measured, it is difficult to properly evaluate the shape of the substrate temperature distribution. A more thorough mapping of the temperature of the entire substrate is necessary to achieve this.

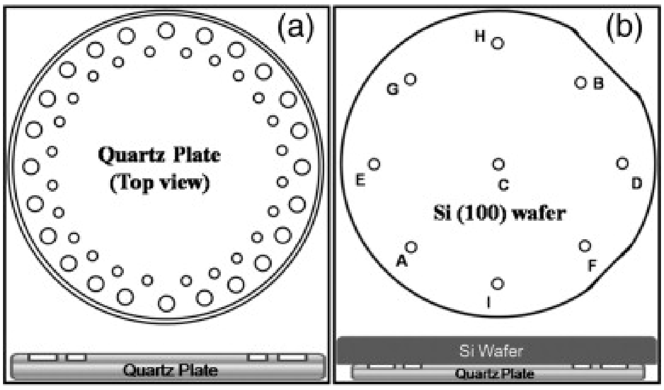

Figure 4.6: Schematic of (a) the design of the insulating quartz plate used to hold the sample during growth (b) the top view of the distribution of substrate surface points at which temperatures were measured, along with the plan view of Si wafer and quartz plate assembly. Reproduced with permission from Elsevier from [116]. © 2012 Elsevier BV.

As the properties of diamond films are dependent on the substrate temperature during growth, it is possible to investigate the temperature uniformity through mapping of film properties alone. Ayres et al. [118] investigated the variance of electrochemical properties of boron-doped diamond wafers grown at varying methane fractions, finding a radial variation in sp^2 content from centre to edge of the wafer. The notable disadvantage of this approach is that it is reliant on the growth of diamond films, which is time-consuming when evaluating the impact of changing growth parameters on substrate temperature uniformity. Other work has combined this property mapping with a computational approach. Cuenca et al. [3] employed a finite element model to investigate the impact of changing the height of the molybdenum substrate holder on plasma distribution during growth, comparing simulation results with Raman spectra and SEM images of various regions of the sample, finding good agreement between the two. However, the authors note that the ability to monitor the temperature distribution of a substrate under growth conditions is needed to allow for further optimisation of holder design.

Whilst considerable work into evaluating the uniformity of substrate temperature during growth has been carried out, up to this point any probing of the substrate temperature distribution under growth conditions has either focused on a small number of isolated points on the substrate, with no ability to map the temperature across the entire substrate, or is reliant on the time-consuming process of growing diamond films for post-growth characterisation. The ability to quickly evaluate the impact of changing growth parameters on substrate temperature would be very powerful as a tool to improve substrate temperature uniformity. The next section of this chapter details the development of an inexpensive and simple to implement non-contact method of measuring of the temperature variation across a substrate under growth conditions, combining existing pyrometric techniques with a mirror galvanometer to produce two-dimensional substrate temperature maps.

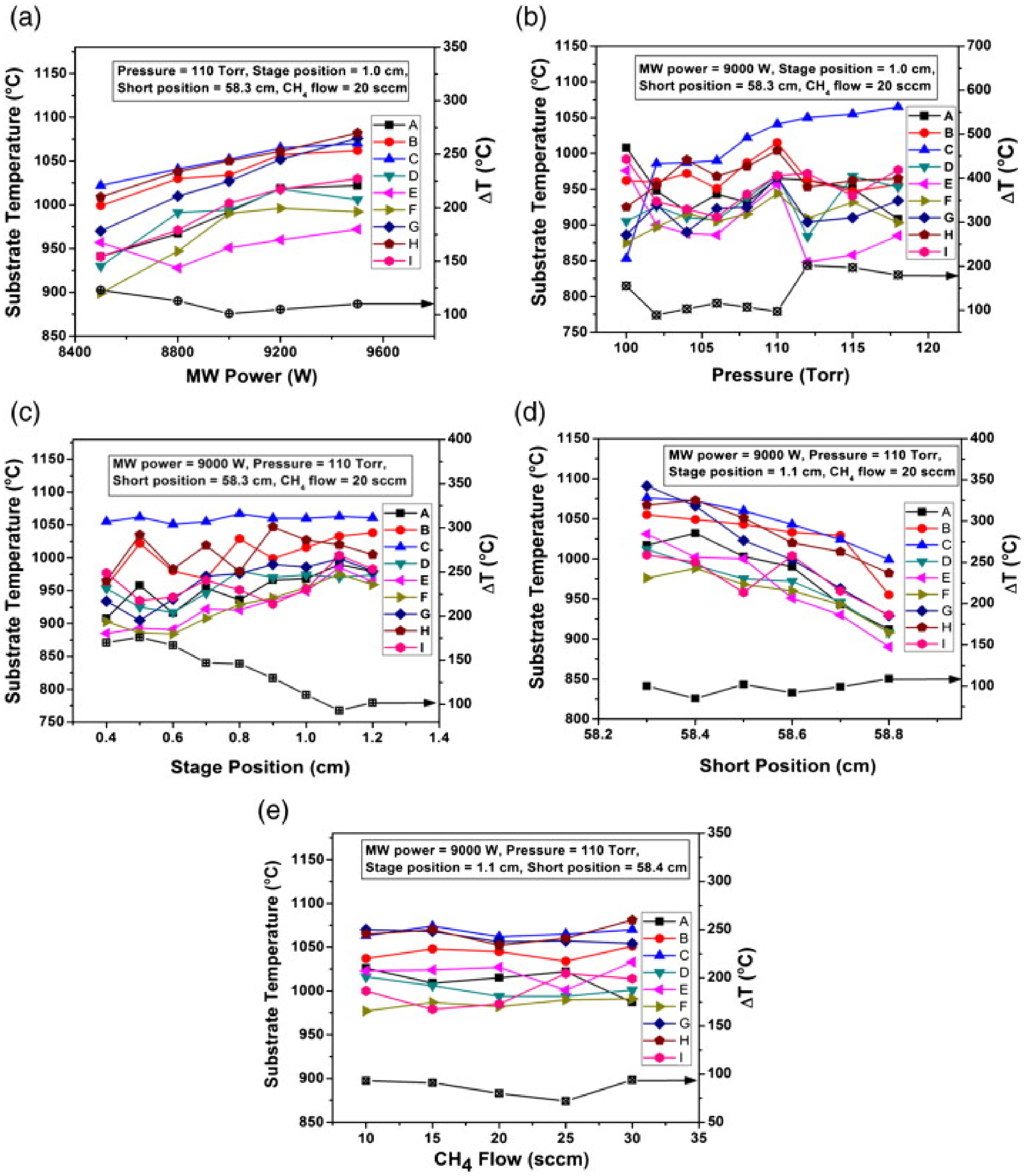

Figure 4.7: Graphs showing the variation of the substrate temperature and the arising temperature difference ($\Delta T = T_{max} - T_{min}$) among nine different surface points, with change in (a) microwave power, (b) chamber pressure, (c) stage position, (d) short position, and (e) methane flow rate. Reproduced with permission from Elsevier from [116]. © 2012 Elsevier BV.

4.3 Mapping the Effect of Substrate Temperature Inhomogeneity During Diamond Growth

4.3.1 Experimental Methodology

A two-dimensional gold mirror galvanometer (galvo) system (Figures 4.8 and 4.9) was used to scan the field of view of a WilliamsonIR Pro 92 dual-wavelength pyrometer of nominal spectral response 2 µm through a top-down 2.75” ConFlat viewport in a Carat Systems CTS6U clamshell-type microwave CVD reactor, producing temperature maps of three different molybdenum substrate holders that are typically used for diamond growth at varying microwave power and chamber pressures. The dimensions and details regarding the typical usage of the three holders are summarised in Table 4.1 and Figures 4.10 and 4.11. The three holders were selected to ensure that the temperature mapping system can evaluate substrate temperature for various holder designs, as a wide range of holder morphologies are typically used for diamond growth on different substrates. All temperature maps were taken using the maximum extents of the field of view of the galvanometer, which was limited by the geometry of the reactor.

Table 4.1: Summary of the three molybdenum substrate holders used.

Holder	Dimensions	Typical Usage
1	Cylinder of diameter 40 mm and height 10 mm	Growth on small samples, typically less than 20 × 20 mm.
2	58 mm diameter, height of 5 mm with 1.5 mm deep recess on top surface and 0.1 mm recess on underside	Thick film growth on 2" wafers of thickness 2 mm or greater.
3	76.2 mm diameter, height of 4.2 mm. 51.3 mm diameter 0.4 mm deep recess on top surface, 1.5 mm deep recess on underside	Thin film growth on 2" wafers of thickness 500 µm.

Holder 1 was mapped under a hydrogen plasma with a range of forward microwave power and chamber pressure conditions, summarised in Table 4.2. Temperature maps were taken in two scan directions; "Y", in which all positions of a single Y-value were mapped before moving on to the next row, and "X", in which

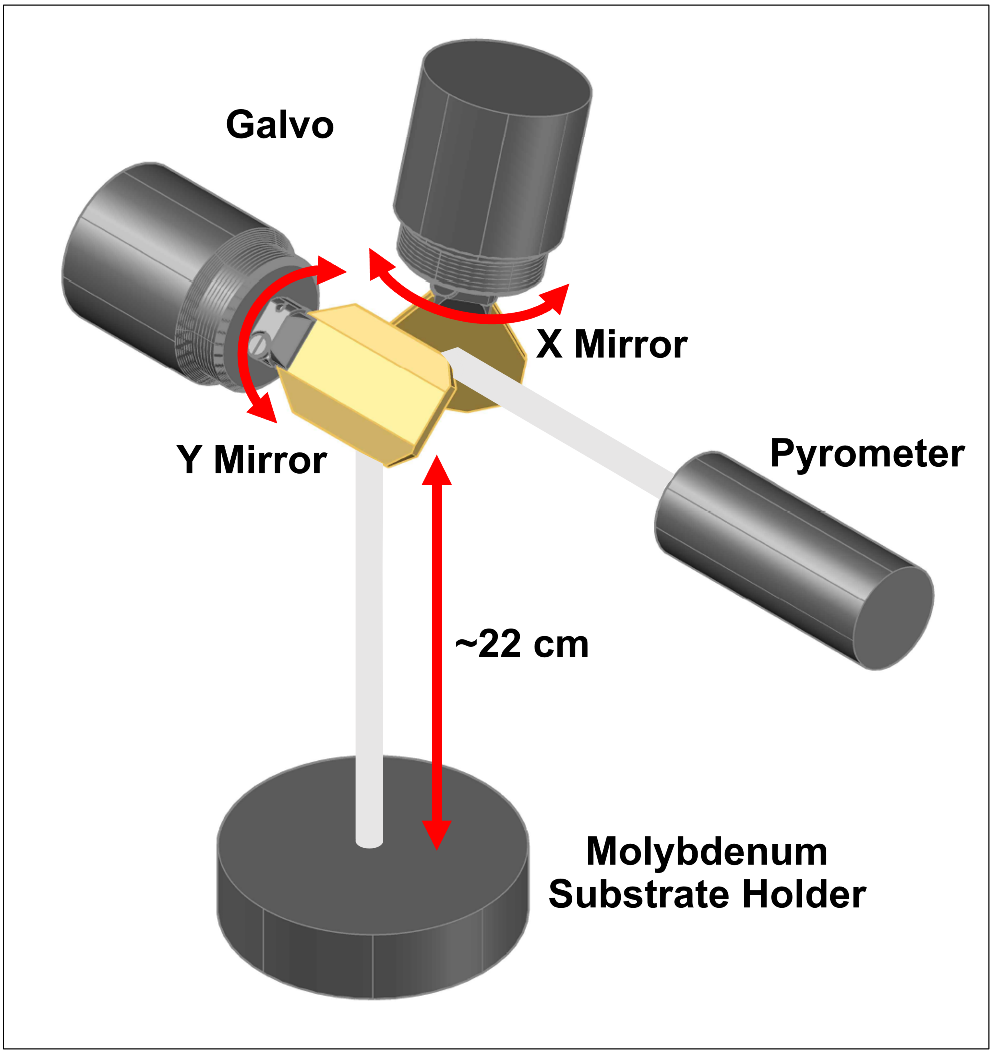

Figure 4.8: Schematic of galvo scanning system. The white beam illustrates the field of view of the pyrometer.

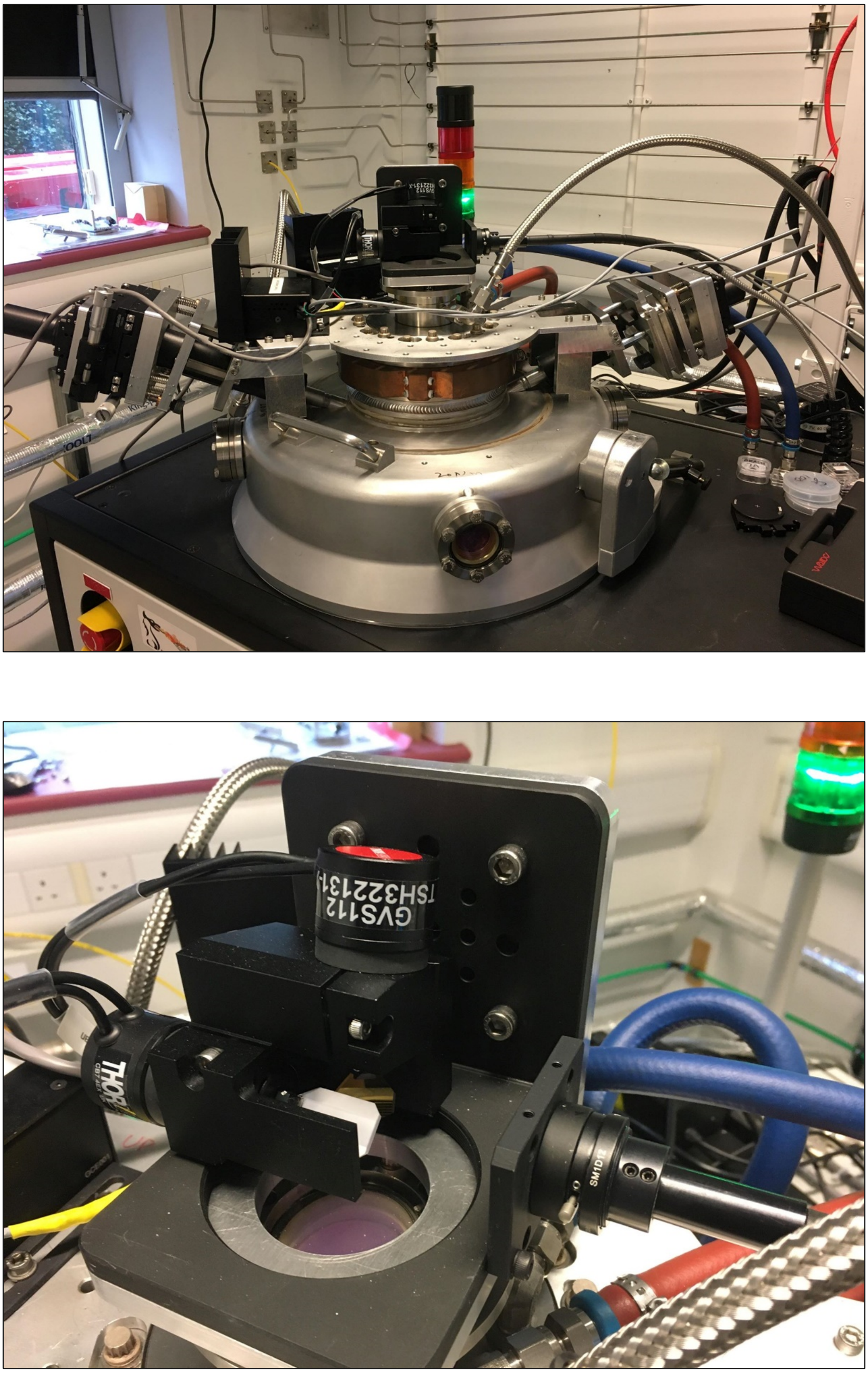

Figure 4.9: Top: Clamshell-type reactor with galvo mounted to the top window. Bottom: Closer look of galvo mounting system. The pyrometer is visible on the right hand side.

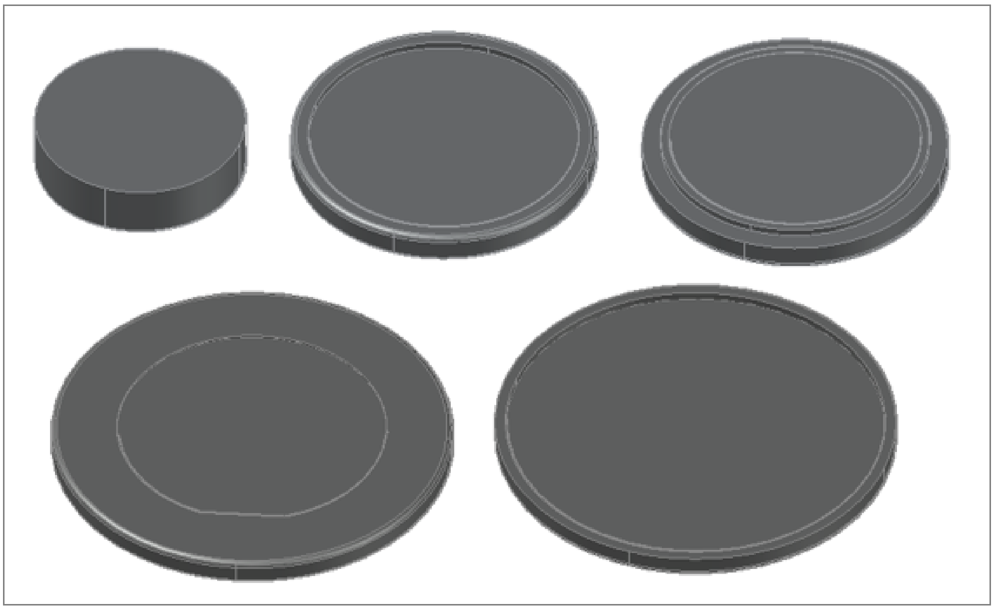

Figure 4.10: Schematics of the three molybdenum substrate holders used. Top row, from left: Holder 1; top side of holder 2; bottom side of holder 2. Bottom row, from left: Top side of holder 3; bottom side of holder 3.

all positions of a single X-value were mapped before moving on to the next column. Unless stated otherwise, all scans were taken in the "Y" direction, with the step size for all scans set to 0.2°.

Table 4.2: Conditions used for temperature mapping of holder 1.

Microwave Power (kW)	**Chamber Pressure (Torr)**	**Substrate**
3	45	None
3.5	75	None
5	90	None

Seeding of silicon substrates is necessary to ensure sufficient nucleation densities for the growth of coalesced films [51, 119]. This was carried out by immersing substrates in a monodisperse hydrogen-terminated nanodiamond/deionised H_2O colloid and placing them in an ultrasonic bath for 10 minutes. This technique is known to produce seeding densities in excess of 10^{11} cm^{-1} [120].

The second holder was mapped under a hydrogen plasma at various power and pressure conditions, both empty and containing a 2 mm thick, 2" diameter seeded silicon (100) wafer. The conditions used for mapping are summarised

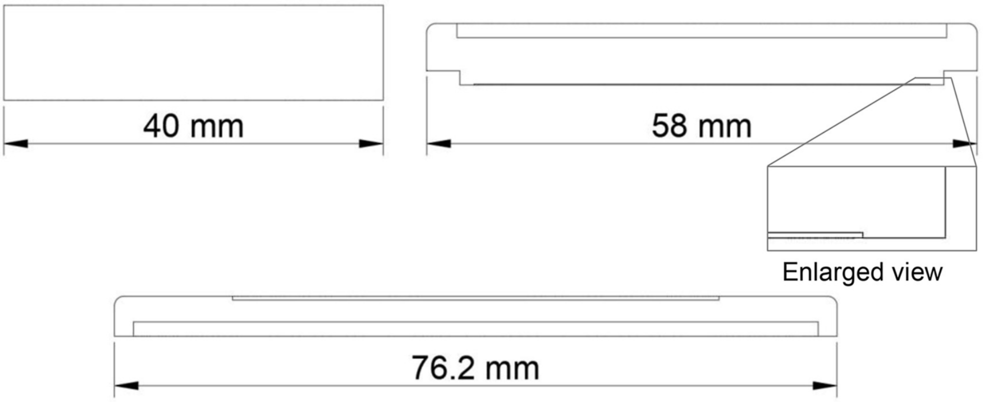

Figure 4.11: Cross-sections of the three molybdenum substrate holders used. Top left: Holder 1. Top right: Holder 2 with enlarged view of the 0.1 mm recess underneath. Bottom: Holder 3.

in Table 4.3. To evaluate the effect of the inclusion of methane in the plasma on temperature distribution, a temperature map of the second holder containing an unseeded 2 mm thick, 2" diameter silicon wafer was taken under a hydrogen plasma at 4 kW 65 Torr. The wafer was unseeded to eliminate the convolution of temperature readings of the pyrometer with the constructive and destructive interference associated with film growth [6, 121]. The feed gas composition was changed to 3% methane diluted in hydrogen and a second temperature map was taken. The flow of methane was then ceased, with the system left for 16 hours in a hydrogen plasma to ensure the elimination of plasma from the reactor, with a third temperature map then taken. A polycrystalline diamond wafer for *ex-situ* Raman characterisation (sample 1) was grown on a seeded silicon wafer of 2 mm thickness in a plasma containing 3% methane diluted in hydrogen, at forward power of 5 kW and chamber pressure of 90 Torr for a period of 86 minutes. The centre thickness of this wafer was estimated at approximately 600 nm using pyrometric interferometry.

The third holder was used to grow a thin wafer for ex-situ SE characterisation (sample 2). The film was grown on a 500 μm thick, 2" diameter seeded silicon (100) wafer, at 4.5 kW and 57 Torr, with a 3-min incubation period at 5% methane to prevent etching of the seeds. The methane level during growth was set to 0.4% to maintain a slow growth rate, and therefore reduce the impact of pyrometric interferometry on the temperature maps generated. Temperature was mapped

Table 4.3: Conditions used for temperature mapping of holder 2.

Microwave Power (kW)	**Chamber Pressure (Torr)**	**Substrate**
3	45	None
4	65	None
4.5	70	None
5	90	None
3	45	Seeded 2 mm thick 2" Si (100) wafer
4	65	Seeded 2 mm thick 2" Si (100) wafer
4.5	70	Seeded 2 mm thick 2" Si (100) wafer
5	90	Seeded 2 mm thick 2" Si (100) wafer

in the "Y" scan direction, with a second scan in the "X" direction taken to evaluate whether pyrometric interferometry had significantly impacted the measured apparent temperature. Attempts to map the holder containing a 500 µm thick silicon wafer under a purely hydrogen-fed plasma resulted in fracturing of the wafer, likely the result of etching of the wafer by the plasma.

A J. A. Woollam M-2000D rotating compensator ellipsometer was used for SE characterisation of the sample grown in holder 3, at an incidence angle of 70° and wavelength range between 193-1000 nm. Sample mapping was carried out using a motorised tilt/translation stage. An iterative fitting procedure was used within the CompleteEASE software, iterating modelled sample structure to minimise the MSE between measured and modelled spectra.

Ex-situ Raman spectroscopy was performed using a HORIBA LabRAM spectrometer at an excitation wavelength of 532 nm. A motorised XYZ stage was used to map the intensity of the diamond Raman peak at 1333 cm^{-1}. A line scan of the intensity of the same peak across the thin sample grown in holder 3 was also taken.

To investigate the plasma distribution during growth, a FEM of the reactor was used. Built in COMSOL Multiphysics®, the model simulates the electric field distribution of the cavity, the plasma fluid distribution and the heat transfer solution for a simplified hydrogen plasma model [122] using a cross section from the Itikawa database. Full details of the model are given in [3].

4.3.2 Temperature Mapping of Holder 1

Figures 4.12 and 4.13 show temperature maps of the first holder at under a hydrogen plasma at a range of power and pressure conditions. Unsurprisingly, higher power and pressure resulted in greater substrate temperatures. It is worth noting that temperatures measured with the galvanometer did not differ substantially from those measured with it. The greatest temperature was observed around the edges of the holder for all conditions, consistent with observations of the edges of the holder glowing under plasma conditions due to the formation of a secondary plasma around the edge of the holder (see Figure 4.14). If these glowing edges are used as a reference, a significant limitation is highlighted in that there is an obvious spatial distortion; the sample holder is observed to be approximately 30 mm in diameter as opposed to the actual diameter of 40 mm. This is due to the spot size of the pyrometer (10 mm at the distance used). With the system aimed at the edge of the holder, there is only partial view of the target. In this case, the apparent temperature can read artificially low.

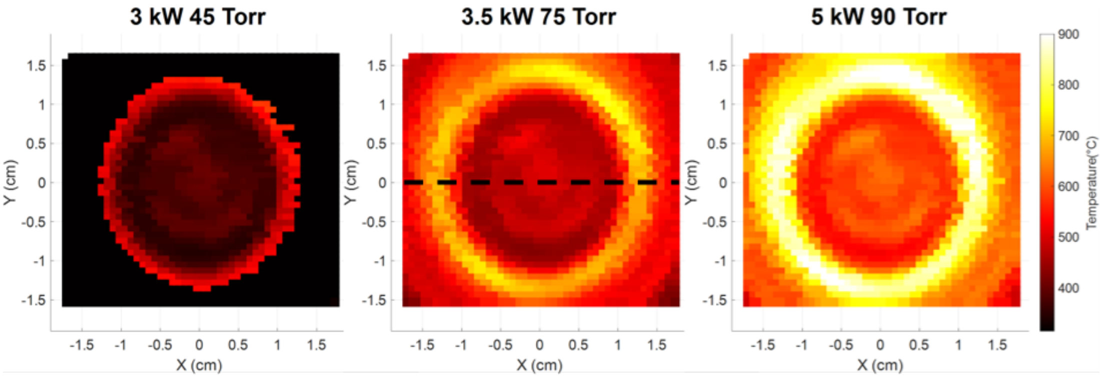

Figure 4.12: Temperature maps of the first holder under a hydrogen plasma at different power and pressure conditions. The dashed line indicates the region of the holder used for line scans of temperature.

The observed spatial distortion becomes obvious when compared with the FEM result under the same conditions. This limitation aside, a similar effect is seen in the model where the edges of the sample holder are hotter than the centre. This

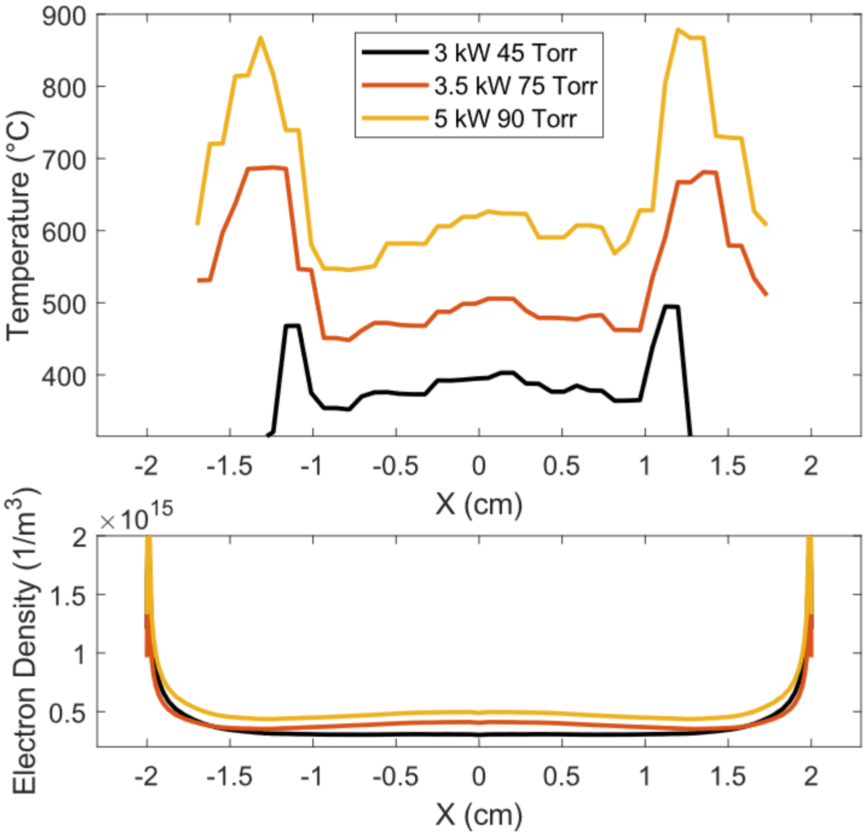

Figure 4.13: Above: Line scans across the centre of the first holder at Y=0 (region indicated by the dashed line in Figure 4.12) at varying power and pressure conditions. Below: Simulation of the plasma density across the same region.

Figure 4.14: Photograph of the first holder under a hydrogen plasma from above, with the glowing edge due to the formation of a secondary plasma visible.

is attributed to the high electric field at the edges of the puck, thereby focusing the plasma around here. Additionally, the centre of the sample is at a marginally elevated temperature which is also corroborated with the model and is simply due to the plasma ball being centred in the middle of the cavity.

4.3.3 Temperature Mapping of Holder 2

Figure 4.15 shows temperature maps of the second holder under a hydrogen plasma at a range of power and pressure conditions, with scans of both the empty holder and the holder containing a 2" diameter, 2 mm thick silicon wafer, seeded with hydrogen terminated nanodiamond. Figure 4.16 shows a comparison of temperature distribution along a line across the centre of the holder at Y = 0, as well as plots of plasma electron density simulated by the FEM across the same region.

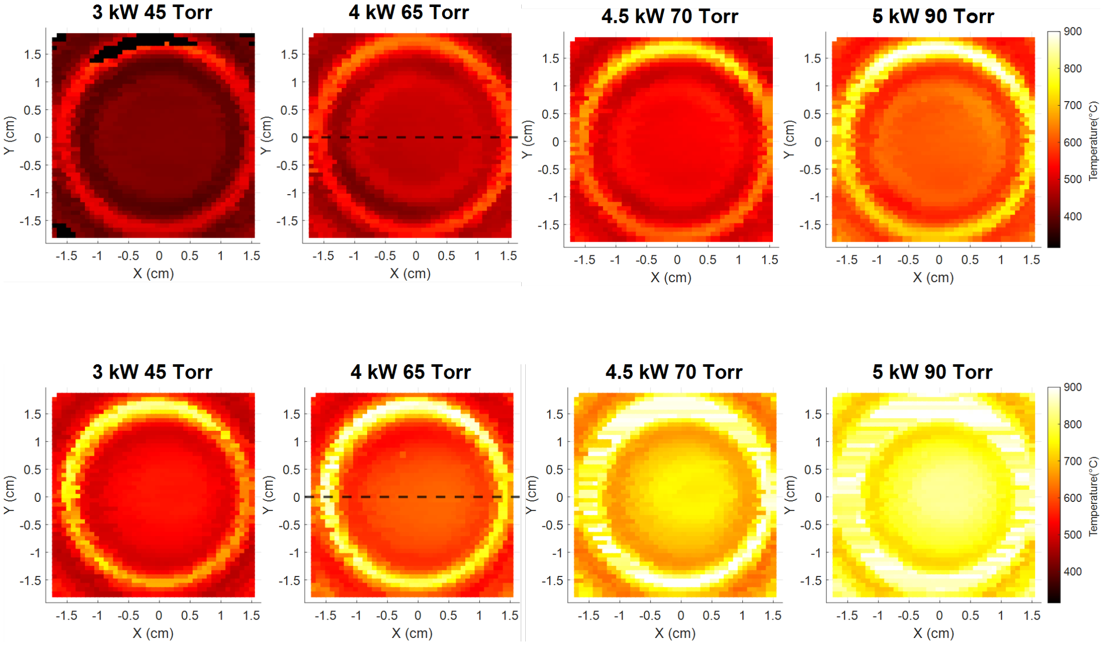

Figure 4.15: Top: Temperature maps of the empty second holder under a hydrogen plasma at different power and pressure conditions. Bottom: Temperature maps of the larger wafer holder containing a seeded 2 mm thick, 2" diameter Si (100) wafer at various power and pressure conditions under a hydrogen plasma. The dashed line indicates the region used for line scans.

As with holder 1, the greatest temperatures were seen around the edges of the holder, consistent with observations of the edges of the holder glowing. Again, these observations were attributed to the higher electric field at the edge of the

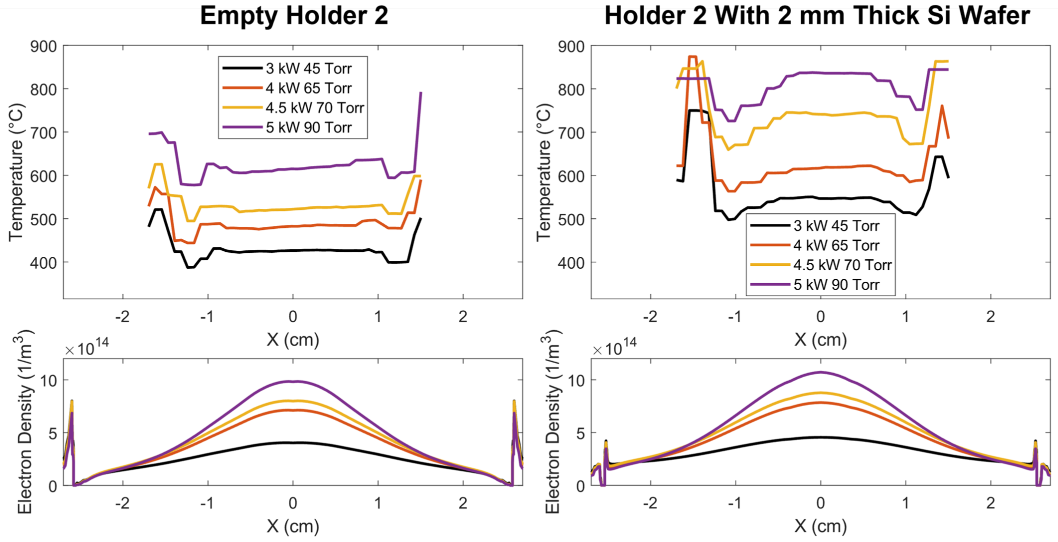

Figure 4.16: Top: Comparison of temperature line scans across the centre of the empty second holder (left) and the second holder at Y = 0 (region indicated by the dashed line in Figure 4.15) containing a 2 mm-thick seeded 2" silicon wafer (right) at various power and pressure conditions under a hydrogen plasma. Bottom: Simulation of the plasma density across the same region of each holder.

holder resulting in the formation of a secondary plasma around the edges of the holder. Unlike holder 1, there was no region of elevated temperature at the centre of the holder, despite an increase in simulated plasma density in this region. It is believed that this is a result of the morphology of the holder. It contains a 1.5 mm deep recess at the centre, and therefore does not protrude as much towards the centre of the plasma ball, resulting in less heating. Also seen is a region of lower temperature towards the edges of the holder, just before the spike in temperature at the edge. This is also believed to be an artefact of holder shape. Holder 2 does not contact the water-cooled reactor stage throughout its entire diameter in order to reduce cooling and allow for the high substrate temperatures at lower power and pressure (in excess of 700 °C) typically required for high quality diamond film growth [2, 121, 123–125]. As contact with the reactor stage is only through a narrow, 1.5 mm wide, ring near the edge of the base of the holder, the cooling of the holder will non-uniform. Such non-uniform cooling is thought to be responsible for this aspect of the observed temperature distribution.

With the placement of a 2 mm-thick seeded 2" silicon wafer in the recess of the holder, a region of elevated temperature was again seen in the centre of the substrate. As the recess in the holder is 1.5 mm deep, the wafer stands 0.5 mm proud from the top surface of the holder, and therefore protrudes further towards the plasma ball, resulting in more heating. At the centre, the temperature increase between an empty and non-empty holder was between 120 and 222 °C, greater for higher power and pressure, with a similar increase in temperature seen at the edges of the holder. A similar increase in temperature was seen at the edges of the holder. Whilst simulated plasma density across the central region is very similar for both the empty and non-empty holder, there is a divergence around the edges; whilst an increase in plasma density is seen at the edge of the holder containing a silicon wafer, this is less pronounced than with the empty holder.

Up to this point, temperature mapping was carried out under a plasma containing only hydrogen to prevent diamond film growth. During film growth, the apparent pyrometer temperature measured will oscillate over time due to interference from varying thickness of the film [6, 89], and film growth will therefore result the production of in an inaccurate temperature map. It is therefore important to evaluate the effectiveness of a hydrogen plasma to approximate MPECVD diamond growth conditions.

To evaluate this, a sequence of temperature maps of holder 2 containing an unseeded 2 mm-thick 2" Si (100) wafer were taken; the first of which under a hydrogen plasma, the second in a plasma comprising 3% methane diluted in hydrogen (typical for MPECVD diamond growth [121, 123–125]) for 55 minutes, and the third after being left in a hydrogen plasma for 16 hours to ensure the elimination of methane from the chamber. Figure 4.17 shows temperature maps from this sequence along with the differences in temperature between these maps, whilst Figure 4.18 shows line scans across the centre of the temperature maps. The addition of methane resulted in an increase in temperature across the centre of the substrate of approximately 50 °C as a result of heat released by the reaction between CH and H species [126]. A greater increase in temperature was seen around the edge of the holder. It is important to note that whilst the measured temperature increased, across the central region of the substrate this increase was uniform. As a result, the temperature maps generated under a hydrogen plasma are a suitable approximation for the shape of the temperature distribution under growth conditions.

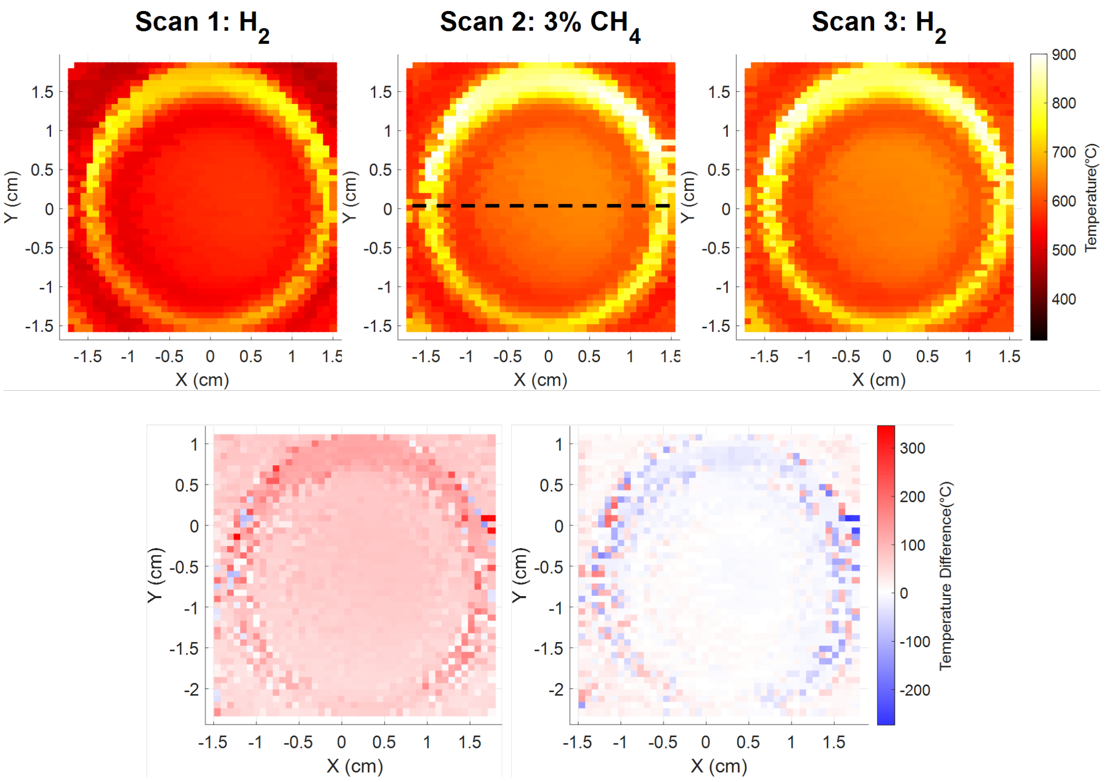

Figure 4.17: Top, from left: Sequential temperature maps of holder 2 containing an unseeded 2 mm thick 2" Si wafer under a hydrogen plasma, under a plasma consisting of 3% methane diluted in hydrogen, and after 16 hours in a hydrogen plasma. Bottom, from left: Temperature distribution difference between map 1 and 2, temperature difference between map 2 and 3.

Interestingly, removal of methane from the plasma did not result in a significant decrease in temperature across the centre of the substrate, although a decrease was seen around the edge of the holder. Given that nucleation density on untreated substrates is too low for the growth of coalesced films [51, 119], it is unlikely that this is the result of any significant film growth. Instead, it is likely due to the observed etching of the substrate. The emissivity of silicon is influenced by surface roughness [127], and as the dual-wavelength pyrometer measurement is dependent on this remaining constant the apparent temperature will change.

Ex-situ Raman spectroscopy was used to evaluate the effect of temperature inhomogeneity during growth on both the thickness and quality of the film. As de-

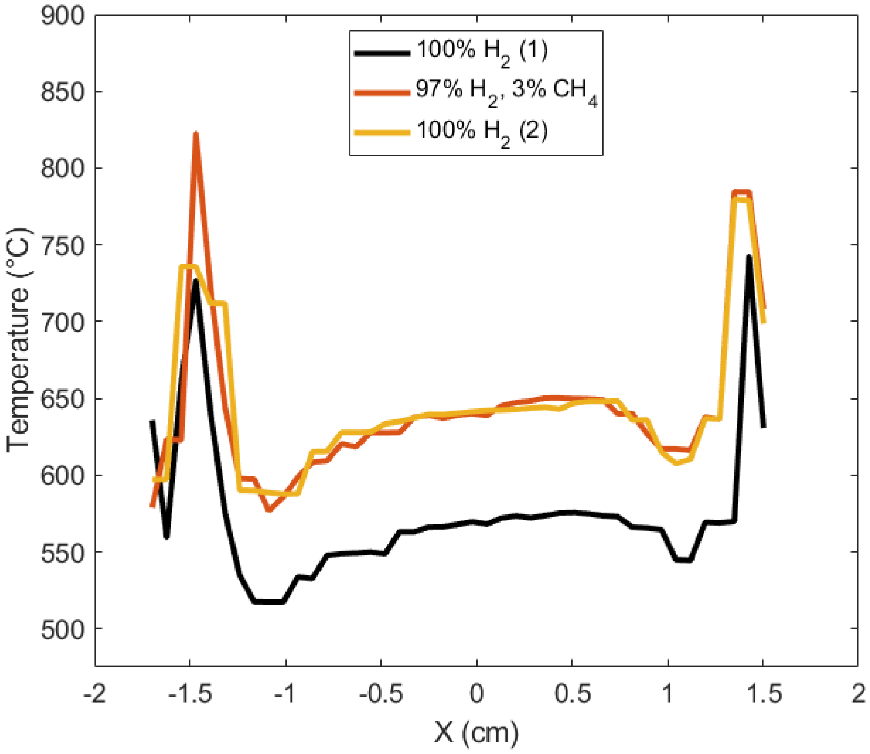

Figure 4.18: From left: Sequential line scans scans of holder 2 containing an unseeded 2 mm thick 2" Si wafer under a hydrogen plasma at Y = 0 (region indicated by the dashed line in Figure 4.17), under a plasma consisting of 3% methane diluted in hydrogen, and after 16 hours in a hydrogen plasma.

tailed earlier in this chapter, previous studies have shown that higher growth temperatures can result in both a faster growth rate and a lower sp^2 volume fraction [1, 2]. Figure 4.19 shows a comparison of substrate temperature with the intensity of the diamond Raman peak for a film grown at the same power and pressure (sample 1), whilst Figure 4.20 shows representative Raman spectra at various points across the sample. The first order diamond Raman peak was visible as a sharp peak across the entire wafer at 1333 cm^{-1}, with a FWHM of 7.7 ± 0.2 cm^{-1} at the centre of the film, indicative of a high-quality diamond film [128]. The measured intensity of this peak displayed a similar trend to the substrate temperature, with the greatest Raman intensity seen in the higher temperature central region of the film, decreasing towards the edge. The Raman intensity alone cannot be used to evaluate film quality; with the film thickness estimated at 600 nm by pyrometric interferometry, the laser is capable of penetrating the entire film, and as such this greater intensity is the product of both a higher quality and thicker film in this region. For a better indication of film quality without convolution with the effects of film thickness, FWHM can be used. A higher level of defects within the film will result in broadening of the peak [129, 130]. The lowest FWHM was seen at the centre of the film, increasing towards the edge, indicating that the greater substrate temperature in the centre has resulted in a higher quality film.

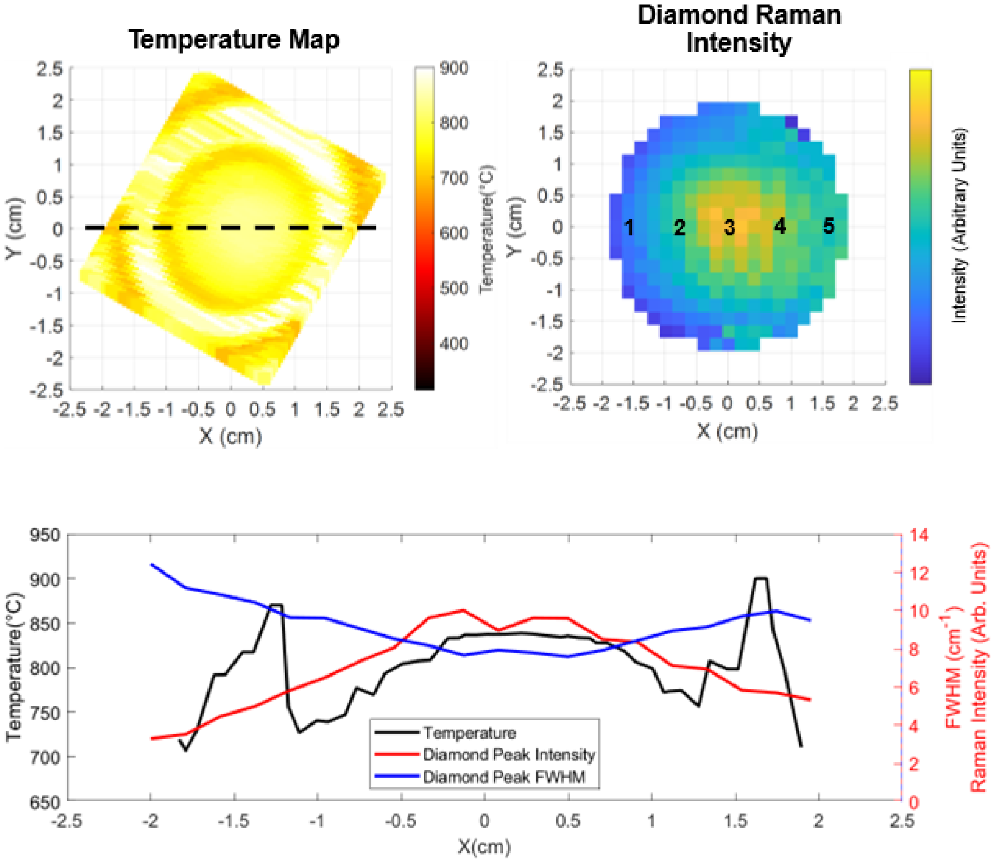

Figure 4.19: Top, from left: Temperature map of the substrate holder containing a 2 mm thick 2" Si wafer under a hydrogen plasma at 5 kW 90 Torr, rotated to match the orientation of the property maps; Map of the intensity of the first order diamond Raman peak at 1333 cm^{-1}. Bottom: Line scans across the region of the film indicated by the dashed line in the temperature map: Temperature line scan under a hydrogen plasma; Intensity of the first order diamond Raman peak at 1333 cm^{-1}; FWHM of the first order diamond Raman peak at 1333 cm^{-1}. All Raman spectra were taken *ex-situ* after growth.

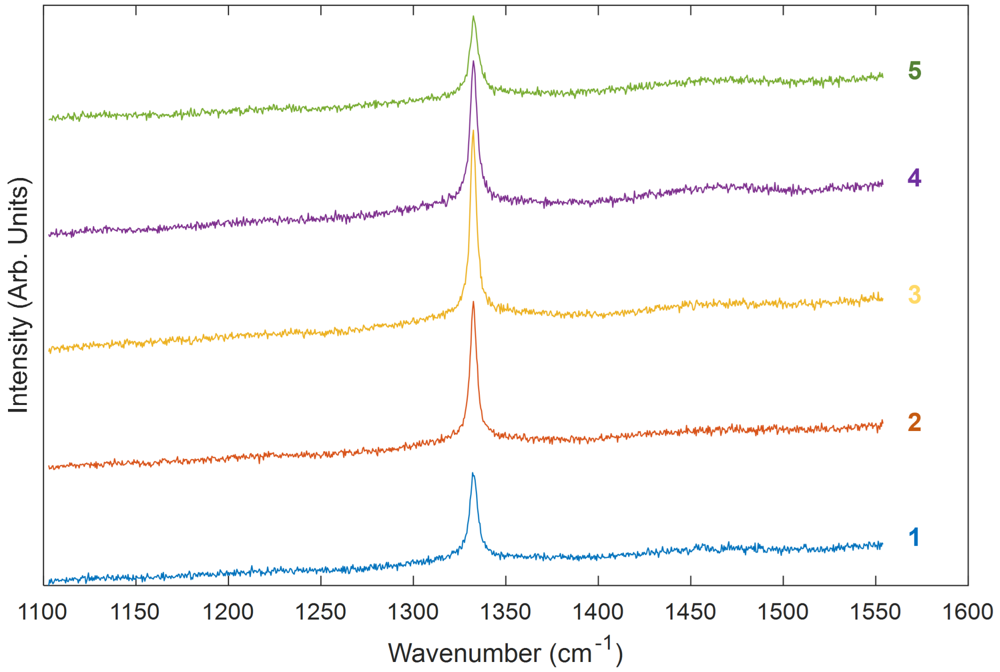

Figure 4.20: Representative Raman spectra from the positions of sample 1 indicated in Figure 4.19

4.3.4 Temperature Mapping of Holder 3

Whilst attempts were made at mapping the temperature of the third holder containing a seeded 500 µm-thick 2" silicon wafer under a solely hydrogen-containing plasma, wafers fractured before any temperature maps could be completed. This was the result of etching of the wafer by the plasma, with etch pits visible on the wafer shards. As a result, mapping was carried out at a low methane concentration, resulting in slow diamond film growth to prevent etching of the silicon substrate. Figure 4.21 shows sequential temperature maps in both the "Y" and "X" scan directions, as well as line scans across the centre of the holder. Taken immediately after the "Y" scan, the "X" scan results in an almost identical temperature map, indicating that pyrometric interferometry has not resulted in a substantial distortion of the temperature mapping.

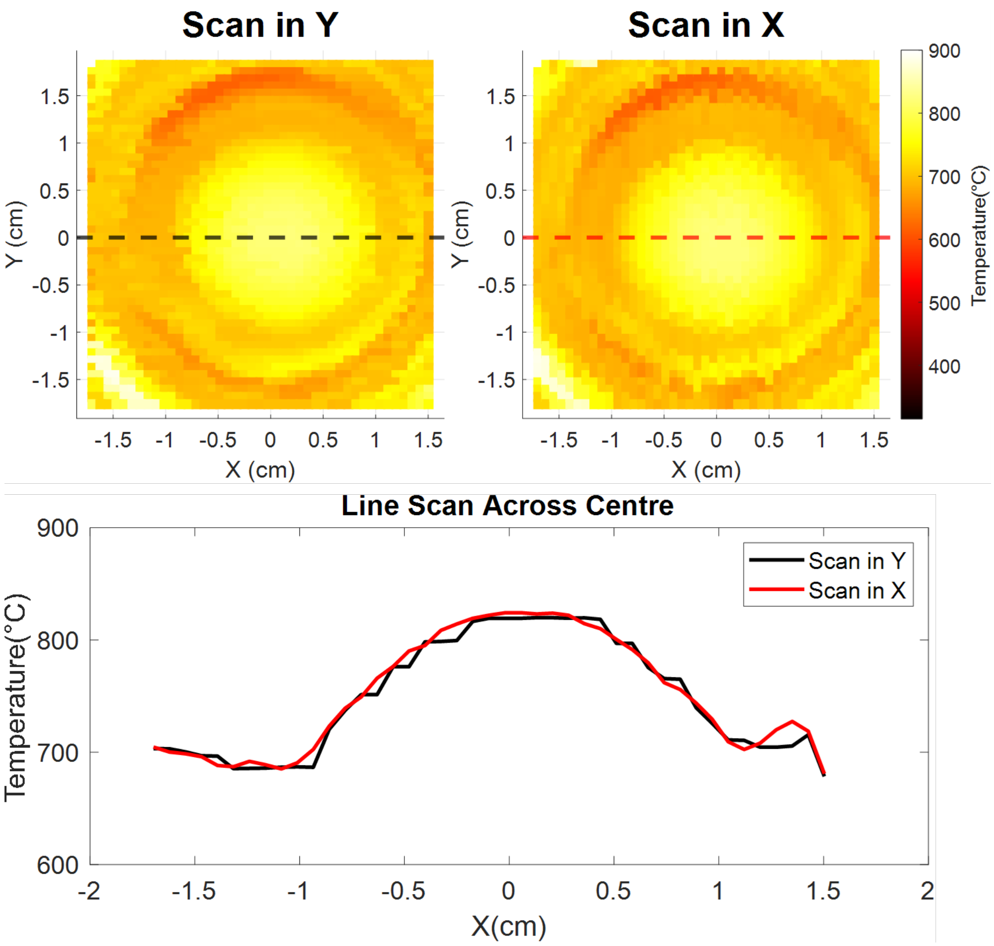

Figure 4.21: Top:Sequential scans of holder 3 containing a seeded 500 µm thick 2" Si wafer in a plasma consisting of 0.4% methane diluted in hydrogen, in the "Y" (left) and "X" (right) scan directions. Bottom: Line scans at Y = 0 (regions indicated by the dashed line).

When compared to holders 1 and 2, holder 3 exhibits a rather substantial hot spot in the centre. This holder is substantially wider than the other two, with the only contact with the water-cooled copper stage occurring around the outside; there is no contact between the centre of the holder and the stage, preventing any conductive cooling here. As a result, the non-uniform cooling is a lot more pronounced than with the second holder. The width of this holder also illustrates an additional limitation of the temperature mapping method, with the geometry of the reactor meaning that the edges of the third holder extend out of the field of the view of the temperature mapping system. The area of greatest temperature around the edge seen with the other two holders was only visible in the bottom left corner of the temperature map. Whilst this prevented mapping of the edges of the holder, the recessed region in the centre holding the silicon wafer was entirely within the field of view of the mapping system.

The slow rate of growth resulted in a very thin sample (approximately 60 nm in the centre), allowing for characterisation using SE. Most previous use of SE for the characterisation of diamond films involves the use of a Bruggeman Effective Medium Approximation (EMA) to approximate the bulk layer, combining optical constants of anticipated components of the film [2, 11, 131, 132]. Typically, optical constants of diamond, void and sp^2 carbon are employed in this bulk layer, although those of sp^2 carbon within polycrystalline films are not easily quantifiable, so it is necessary to use those of another material, such as glassy carbon to approximate them. A more detailed review of previous use of SE for characterisation of diamond films can be found in chapter 5.

Characterisation of nanocrystalline diamond films outside of the very early stages of growth presents several difficulties. The effective medium approximation used to model the bulk layer is only valid where the size of phases are smaller than one tenth of the probing wavelength [85]. Furthermore, surface roughness resulting from the overgrowth of competing crystallites can lead to scattering of the incident light, causing depolarisation [85, 133]. Such issues were particularly evident in the initial analysis of spectra taken between 193 and 1000 nm. Analysis of these using a model previously shown to effectively characterise early-stage diamond film growth [131] resulted in significant MSE between measured and modelled spectra. The model is made up of a three layer stack atop a silicon substrate modelled using reference optical constants of silicon [134]. The next layer accounts for the carburisation of silicon substrates that typically observed under MPECVD diamond growth conditions [58, 135] using the optical constants of silicon carbide [136]. The polycrystalline diamond film was represented using an EMA mixing the optical constants of three components; a general oscillator matched to reference optical constants of diamond [136], glassy carbon to approximate sp^2 content [137], and void. The top layer of this stack was an EMA made up of 50% bulk and 50% void to approximate surface roughness. It was observed that there was a high level of parameter correlation between the thickness of the SiC layer and other parameters, including surface roughness and bulk layer thickness. As a result of this, the thickness of this layer was not allowed to vary across the whole film and was instead fixed at the 1.75 nm measured in the centre of the film.

The films previously characterised using this model were thinner than the film characterised in this work, and therefore exhibited lower surface roughness and smaller crystallites [131]. In this work, a significant degree of depolarisation was observed at the shortest wavelengths, resulting in an increase in MSE. To reduce the impact of scattering due to surface roughness, the minimum wavelength was increased to 300 nm, resulting in a significant reduction in MSE. In the final iteration of the model, the only quantities allowed to vary through the fit process were the surface roughness and the thickness and composition of the bulk layer. An instrument bandwidth of 5 nm was incorporated into the model to account for depolarisation. This final iteration of the model, shown in Figure 4.22, produced a good fit between measured and simulated spectra.

Figure 4.23 compares maps of the SE-derived properties and MSE with the temperature map of the sample during growth, whilst Figure 4.24 shows line scans of the same parameters, comparing them with the intensity of the first-order Raman peak in the same region. Representative Raman spectra from various regions of the sample are shown in Figure 4.25. Due to the limited thickness of sample 2, very long laser exposure times were required to generate sufficient signal for Ra-

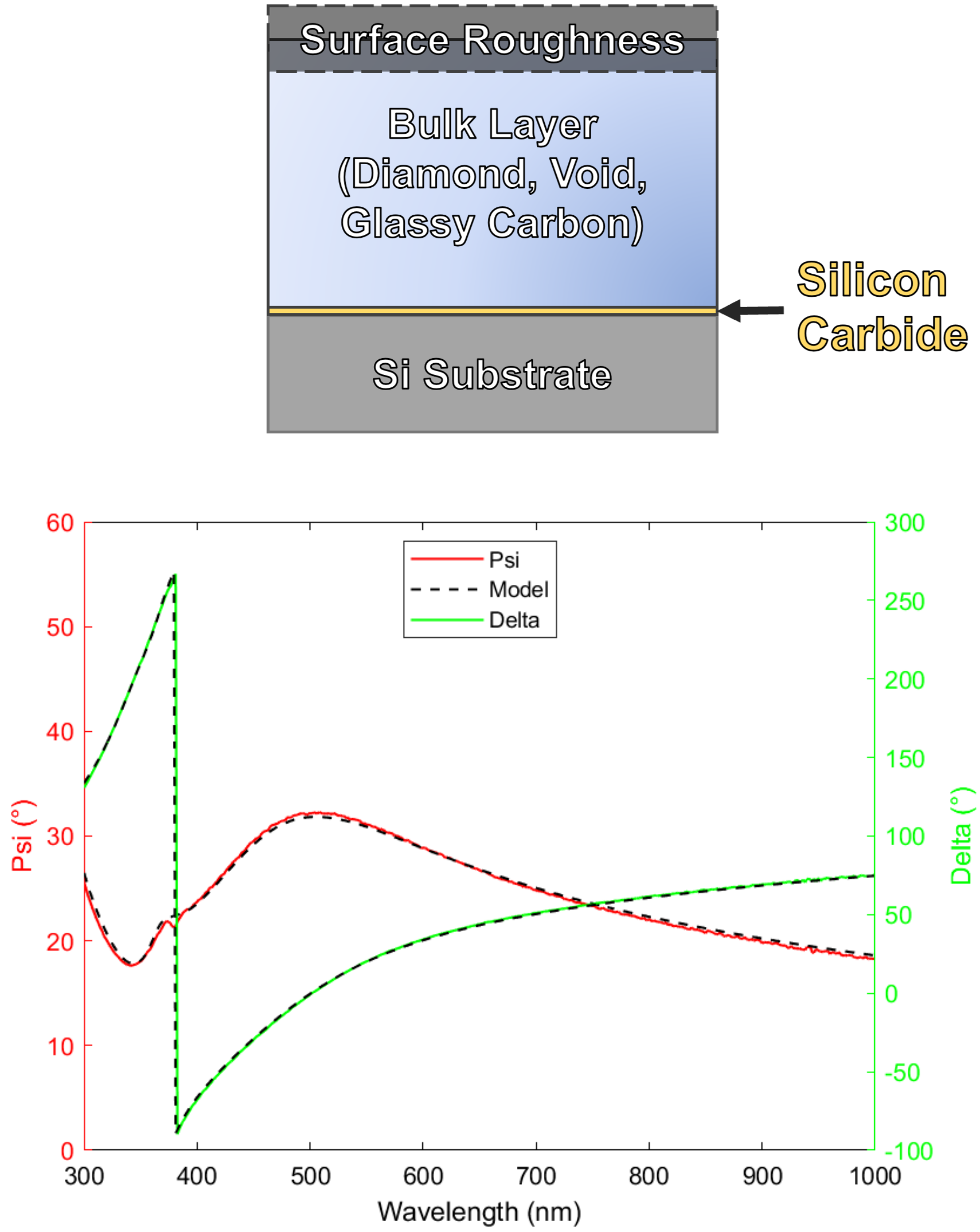

Figure 4.22: Top: Schematic of the SE model used to fit sample 2. Bottom: Comparison of measured and modelled spectra at the centre of sample 2.

man characterisation. As a result of this, Raman mapping of the sample was restricted to a line scan across the centre. The region of greatest temperature in the centre of the wafer corresponded with the greatest SE-measured bulk thickness. As noted earlier, it has previously been seen that higher substrate temperatures result in faster growth rates [1]. The opposite trend was seen seen in the levels of bulk impurity in the diamond film; the glassy carbon (approximating sp^2 material) and void fractions were lowest in the centre, increasing towards the edges. This is consistent with previous SE measurements suggesting that a greater proportion of sp^2 material is incorporated in the early stages of film growth at lower substrate temperatures [2]. The area of very low bulk thickness in the top left of the sample is the result of slight delamination of the film here.

As seen in sample 1, the intensity of the first-order diamond Raman peak was greatest in the high-temperature central region, decreasing towards the edge. Given that sample 2 is very thin, the intensity of this peak will be impacted by the thickness as well as the quality of the film, as the laser is easily capable of penetrating through the entire film. A thicker film will result in a more intense peak, as will a higher-quality film. This observation correlates with the SE model showing both greater bulk thickness and a greater proportion of sp^3 (and therefore higher quality film) in the centre. It is notable that the diamond Raman peak is broader in the thinner sample 2, with broadening occurring as is typical with smaller crystallite size [138].

4.4 Conclusion

Substrate temperature inhomogeneity under MPECVD growth conditions was investigated *in-situ* using a mirror galvanometer, scanning the field of view of a dual-wavelength pyrometer to produce temperature maps. An increase in temperature was seen towards the centre of the holder, matching FEM simulations of a greater plasma density in this region. Similarly, the observation of high temperature around the edge of the holders was validated with high plasma density in this area. The properties of diamond films were mapped using *ex-situ* Raman spectroscopy and SE and compared with temperature maps at the same

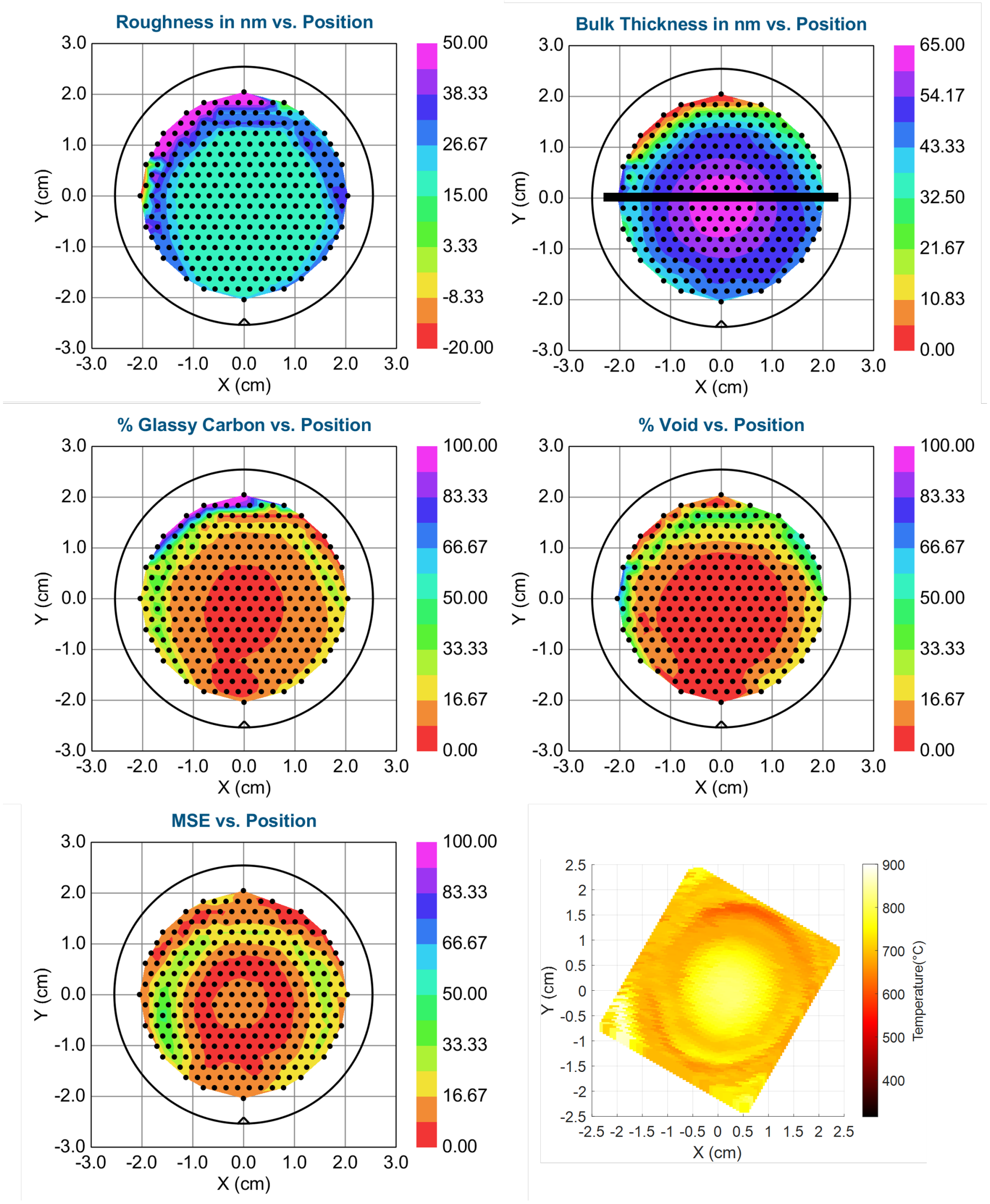

Figure 4.23: Property maps of sample 2, with black dots indicating the locations SE spectra were taken. Top, from left: Thickness of surface roughness layer in the SE model across sample 2; thickness of the bulk EMA layer. Middle, from left: Bulk EMA glassy carbon fraction; bulk EMA void fraction. Bottom, from left: MSE of the model; temperature map of the sample during growth, rotated to match the orientation of the SE spectra.

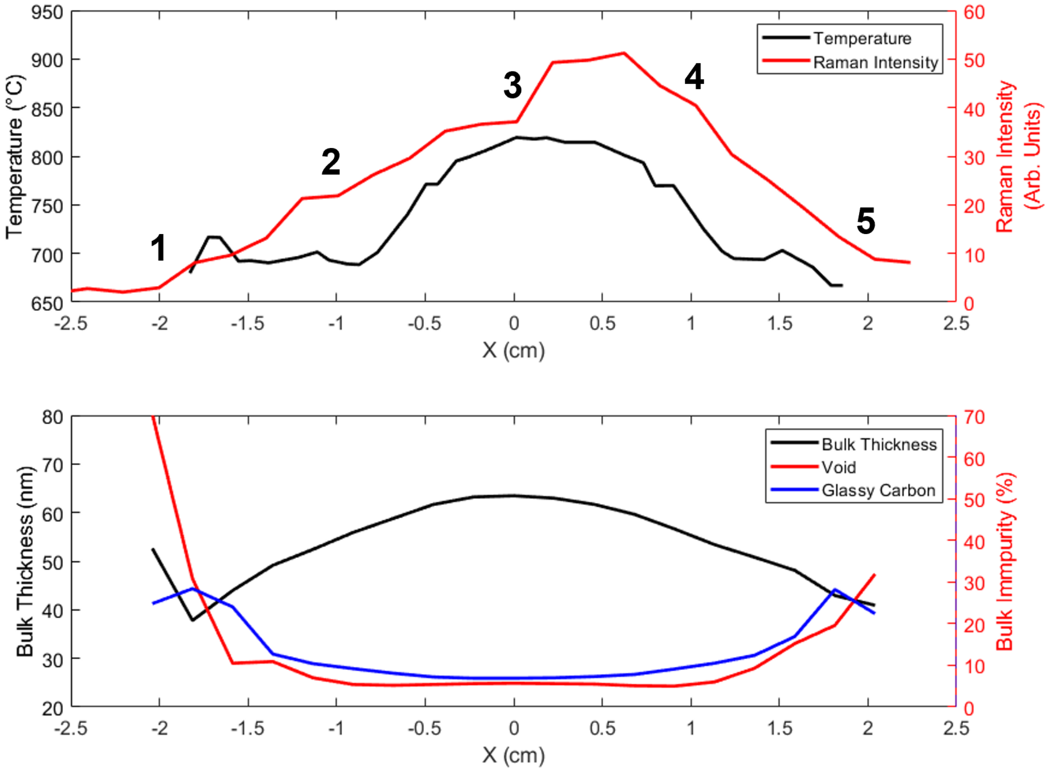

Figure 4.24: Line scans across the centre of sample 2 at Y = 0 (region indicated by the solid line in Figure 4.23. Top: Temperature during growth and intensity of the first order diamond Raman peak. Bottom: SE-derived bulk layer thickness and impurity fractions.

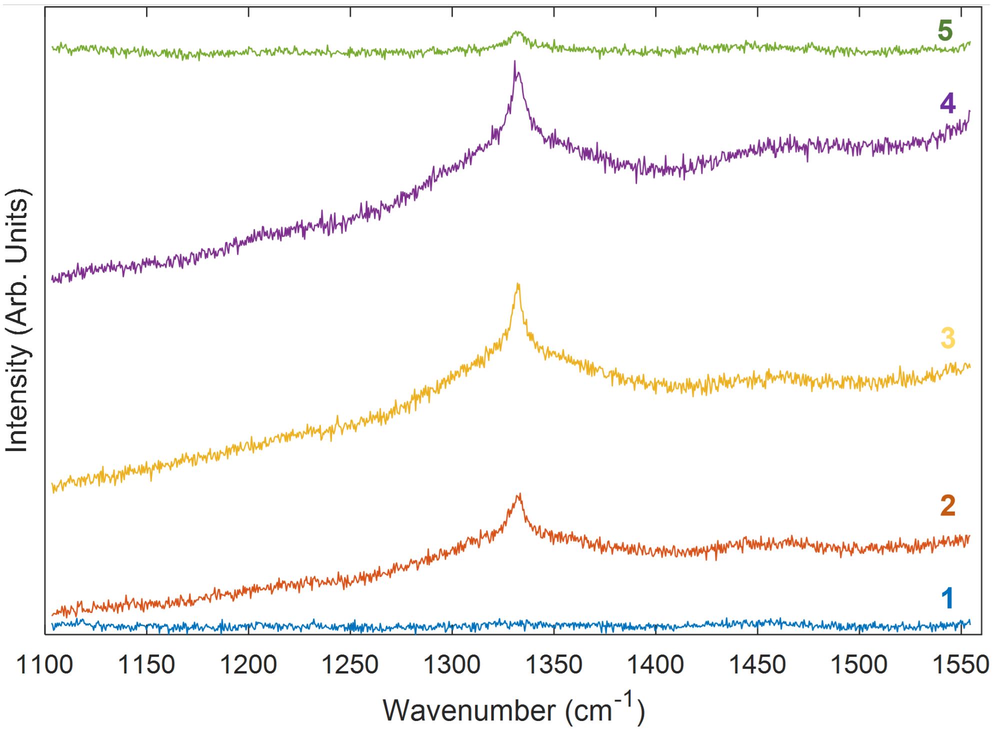

Figure 4.25: Representative Raman spectra from the positions of sample 1 indicated in Figure 4.24

power and pressure. A greater SE-measured bulk thickness and bulk sp^3 fraction were seen in the central region of higher temperature, as was a greater intensity and lower FWHM of the first-order diamond Raman peak, indicative of a thicker and higher-quality film. The correlation between mapped temperature, simulated plasma density and thickness and composition of diamond films demonstrates that this technique is an effective measurement of substrate temperature distribution. Given that ensuring film uniformity is a significant challenge to diamond growth, the ability to map the substrate temperature is a powerful tool to evaluate the impact of substrate holder design, microwave power and chamber pressure allowing for further optimisation of growth conditions.

Chapter 5

In-Situ Monitoring of Diamond Growth on Silicon

The quality of polycrystalline diamond films grown by MPECVD is heavily dependent on the nucleation and early stages of growth. However, the harsh plasma environment and relatively high pressure during growth largely restrict *in-situ* characterisation to optical methods. Whilst laser and pyrometric interferometry have previously been used for this purpose, they are limited in resolution and do not provide any compositional information. SE can be used to provide real-time monitoring of the thickness, composition and microstructure of early-stage MPECVD diamond growth with sub-nanometre resolution, although previous attempts have been limited by damage to the substrate caused by substrate preparation using mechanical abrasion with diamond grit. This chapter reviews previous use of SE for the characterisation of diamond films in section 5.1 before detailing experimental work utilising SE to monitor early-stage diamond growth in section 5.2. *Ex-situ* SE spectra are used to develop an optical model for film characterisation, which is then applied to *in-situ* spectra. The model is validated with *ex-situ* AFM images and Raman spectra, and is also used to evaluate the impact of varying the methane concentration on early-stage growth.

This chapter is adapted from the manuscript published in [13].

5.1 Previous Use of Spectroscopic Ellipsometry For Characterisation of Diamond Films

With polycrystalline diamond exhibiting many of the extreme properties of bulk diamond, this allows for exploitation of such properties over large areas at significantly lower cost [51], presenting applications such as microelectromechanical systems [34], boron-doped diamond electrodes [29] and thermal management solutions [18, 28]. With the quality of these films heavily dependent on the seeding and early stages of growth [5], the ability to monitor these early stages is crucial to optimise growth conditions. However, the relatively high pressure during MPECVD growth prevents the use of electron-based techniques such as reflection high-energy electron diffraction, with the harsh plasma environment largely limiting characterisation to optical techniques [2]. Whilst pyrometric and laser interferometry are typically used to monitor film thickness during growth [6, 7], these are limited in resolution and provide no compositional information. Raman spectroscopy is commonly used to characterise diamond films, it is significantly more sensitive to non-diamond carbon than to diamond material, and is completely insensitive to void [10]. In comparison with these techniques, SE presents a number of advantages, with an ability to determine the thickness and diamond, void and sp^2 content (with equal sensitivity) of films as thin as 4 nm [11].

5.1.1 Bulk Layer Characterisation

If the grains and interfacial regions of the polycrystalline diamond film are significantly large so as to retain bulk optical constants and the mixing is homogeneous on the scale of the wavelength of the probing light, the film can be modelled using an effective medium approximation (EMA):

$$\frac{\tilde{N}_e^2 - \tilde{N}_h^2}{\tilde{N}_e^2 + 2\tilde{N}_h^2} = f_1 \frac{\tilde{N}_1^2 - \tilde{N}_h^2}{\tilde{N}_1^2 + 2\tilde{N}_h^2} + f_2 \frac{\tilde{N}_2^2 - \tilde{N}_h^2}{\tilde{N}_2^2 + 2\tilde{N}_h^2} + \ldots \tag{5.1}$$

Where $\tilde{N}_e$, $\tilde{N}_h$, $\tilde{N}_1$, and $\tilde{N}_2$ are the complex refractive indices of the effective medium, host medium, and inclusions of type 1 and 2 respectively. f_1 and f_2 are the volume fractions of inclusions 1 and 2 [87]. The main assumption of this model is that the inclusions and dipole interactions are spherical [139]. Whilst this is not always satisfied, it proves to be a reasonable approximation [87]. Further approximations are required to define the host medium. The Maxwell-Garnett approximation describes inclusions in a host material. For a single inclusion in a single host, the equation is:

$$\frac{\tilde{N}_e^2 - \tilde{N}_h^2}{\tilde{N}_e^2 + 2\tilde{N}_h^2} = f_1 \frac{\tilde{N}_1^2 - \tilde{N}_h^2}{\tilde{N}_1^2 + 2\tilde{N}_h^2} \tag{5.2}$$

This model breaks down when used to model surface roughness, or in other cases where the volume fractions of inclusion and host are similar [140]. To prevent such breakdown, the Bruggeman approximation sets the complex refractive index of the host material to that of the effective medium. For two materials, the EMA is:

$$f_1 \frac{\tilde{N}_1^2 - \tilde{N}_e^2}{\tilde{N}_1^2 + 2\tilde{N}_e^2} + f_2 \frac{\tilde{N}_2^2 - \tilde{N}_e^2}{\tilde{N}_2^2 + 2\tilde{N}_e^2} = 0 \tag{5.3}$$

This equation can be extended for additional inclusions.

5.1.2 Early Stage Growth

Using a Bruggeman EMA, Cong et al. [10] performed *ex-situ* SE on polycrystalline diamond films between 100 and 400 nm thick, grown on silicon substrates seeded by polishing with diamond powder. Using regression analysis, an iterative fitting process was applied (see Figure 5.1). An initial model using optical constants of bulk diamond from literature resulted in a poor fit, with the MSE greatly improved by the addition of glassy carbon, representing sp^2 material in grain boundaries, and void. A further decrease in MSE was observed from the inclusion of second EMA, consisting of a mixture of diamond and void, to represent the surface roughness. The addition of an sp^2 component to the surface roughness layer did not significantly reduce MSE, whilst reducing the predicted sp^2 volume fraction in the bulk layer. These two volume fractions were found to be highly correlated. As it was anticipated that much of the sp^2 content in the film is located in grain boundaries, it was suggested that the high sp^2 volume fraction found in the roughness layer was a result of model inaccuracy or experimental error, and thus the inclusion of a three-component roughness layer was unwarranted. The model was later used to investigate the impacts of substrate temperature and methane concentration during growth on sp^2 content, finding that this increased with greater methane concentration and lower substrate temperature.

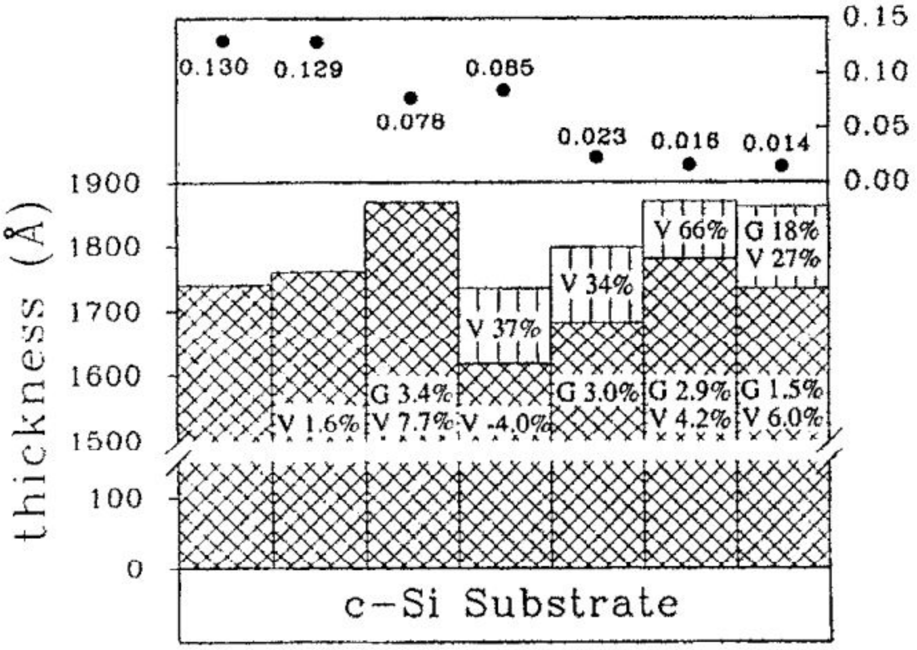

Figure 5.1: The evolution of the fitting process used by Cong et al, showing the changes in mean square error (σ) with the inclusion of diamond, void (V) and sp^2 carbon (G) components. Reprinted from Y. Cong et al., “Spectroellipsometry characterization of optical quality vapor-deposited diamond thin films”, Applied Physics Letters **58**, 819–821 (1991), with the permission of AIP Publishing.

Collins et al. [141] used SE to investigate the effects of the growth environment on the silicon substrate. Untreated silicon wafers were mounted on a graphite holder, then exposed to a microwave plasma optimised for diamond growth for varying duration between 2 minutes and one hour. The plasma heater the substrate and holder, and an equilibrium temperature of 980 °C was reached after 5 minutes of exposure to the plasma. Using SE, a damaged surface layer approximately 10 nm thick was identified on top of the substrates exposed for less than 5 minutes. This surface layer was best approximated as an EMA mixture of crystalline silicon, amorphous silicon, and void. On top of this, a weakly absorbing surface layer of approximately 7 nm thickness was observed, consisting of silicon carbide with a 63% void fraction. In those samples exposed in excess of 5 minutes, annealing of the the damaged layer was observed. It displayed a much lower void fraction, along with no detectable amorphous silicon phase. The damaged layer remained relatively constant in thickness, between 10 and 20 nm. The weakly absorbing surface layer also decreased in void fraction, with its thickness remaining within the range of 4-7 nm and not showing any trend with increasing exposure time.

Accurate determination of the composition of the weakly absorbing surface layer was difficult, as whilst the best fit employed a silicon carbide/void mixture, it could also be modelled using other materials. 3 possibilities were identified: A discontinuous diamond layer, a silicon oxide layer, and the aforementioned low density silicon carbide layer. The possibility of a diamond layer was ruled out due to the thickness remaining constant with increasing exposure time; if diamond had nucleated, the thickness of the layer would increase with increasing exposure time. Whilst SiO_2 is unstable in the plasma environment [142], it is possible that post-oxidation had occurred. In order to identify the composition of the surface layer, several chemical etches were performed. Following treatment with HF in methanol, a known etch for SiO_2 [143], the thin layer remained intact with some surface roughening, ruling out the possibility of an oxide layer. A second treatment with a 50/50 mixture of $K_3Fe(CN)_6$ and NaOH, a mixture known to etch SiC [144], was performed. SE analysis revealed this treatment reduced the thickness of the layer by 2 nm, suggesting a defective carbide layer.

As detailed earlier in this thesis, the nucleation density of diamond on untreated silicon substrates is too low for the growth of coalesced films, necessitating a pretreatment step [51, 119]. Several SE studies have investigated the seed layer formed by these processes in detail. Notably, attempts at using SE for this purpose on substrates treated by mechanical abrasion with diamond grit have proved unable to determine any diamond content due to the resultant surface damage [2, 145]. More recently, SE studies of substrates treated using alternative seeding methods that cause less substrate damage have proved more fruitful.

Mistrik et al. [146] used silicon substrates seeded with monodispersed nanodiamond particles with a mean diameter of 4-6 nm, resulting in surface densities of approximately 10^{10} cm^{-2}. A series of nanocrystalline diamond films were deposited at different substrate temperatures (520, 550 and 600 °C and pulsed plasma frequencies (2.7, 4.5 and 14.3 kHz). SE spectra were taken between 0.7-5.5 eV (225-1770 nm). A seed layer was modelled using a Bruggeman EMA, using optical constants of diamond and amorphous carbon taken from literature. Over the sample set, the inclusion of this seed layer, between 15 and 32 nm thick, reduced the MSE from approximately 15 to approximately 13. The addition of the seed layer did not significantly impact the modelled bulk thickness. AFM scans of seeded substrates showed a discontinuous nanodiamond seed layer, with a mean thickness of 12.3 nm, corresponding with the SE modelled seed layer thickness. Micro-Raman was carried out to determine the non-sp^2 content, estimating between 92-97% diamond content. This value was close to the SE-obtained value of between 84-93%.

Pinter et al. [147] carried out SE silicon substrates cleaned in a hydrogen plasma and seeded by BEN. The seeded substrates were exposed to diamond growth conditions for various times between 8 and 180 minutes. After plasma cleaning and 8 minutes of BEN, SE models predicted a 3.5 nm thick layer, consisting of 95% diamond, 0.6% graphite (to account for sp^2 material) and 7% SiO_2. Following an hour of growth, SE indicated a 20.5 nm thick seed layer, consisting of 50% graphite, 43% void and 7% SiC, underneath a 189 nm thick bulk layer with 2% graphite content. Rutherford backscattering spectroscopy and elastic recoil detection were performed, estimating a 3% graphite content in the bulk layer, which corresponded well with the SE-predicted 2% graphite content.

Lohner et al. [148] performed SE on diamond films grown on BEN-treated silicon substrates by MPECVD. SE was performed between 0.7-6.5 eV (190-1700 nm) at angles between 55 and 70°. Using linear regression analysis and effective medium approximations with optical constants taken from literature, a three-layer optical model of the deposited film was constructed. Closest to the substrate was a seed layer, approximately 41 nm thick, containing 69% sp$_3$ and 31% sp^2 carbon (approximated using glassy carbon), with a small void component. Directly above this layer was a 278 nm thick bulk layer, containing upwards of 99% sp^3 carbon, with small amounts of sp_2 and void. The third and final layer was a 11-16 nm thick surface roughness layer. This study extended the SE measurement further into the UV region than previous work, and observed a deviation between modelled and measured Ψ between 190 and 220 nm. In order to account for this, a second model was constructed, using a Tauc-Lorentz optical model to more accurately describe the changing dielectric function of the sp_3 component of the three layers with the loss of long range order. This revised model, shown in Figure 5.2, also indicated the existence of a 41 nm seed layer, containing 21.6% glassy carbon, as well as a bulk nanocrystalline layer containing 0.77% sp^2 carbon.

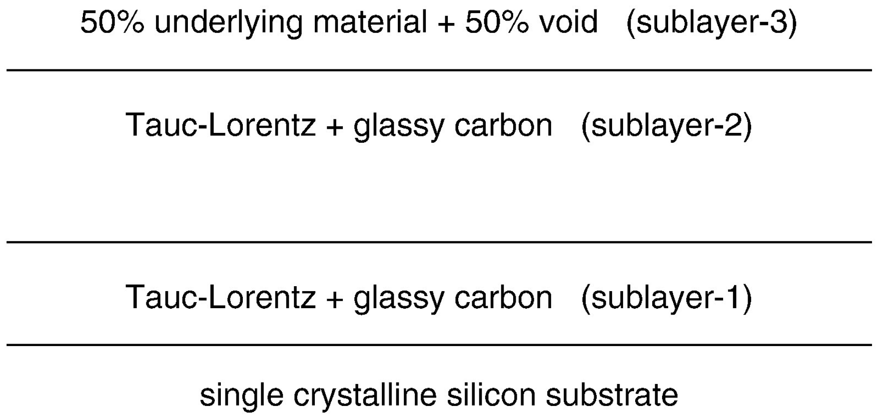

Figure 5.2: Final iteration of the model used by Lohner et al. to fit spectra. Reproduced with permission from [148].

Thomas et al. [131] performed SE of a series of 25-75 nm thick nanocrystalline diamond films grown on silicon wafers seeded with a hydrogen-terminated monodispersed nano-diamond/DI H_2O colloid. Films were grown by MPECVD in a methane/hydrogen plasma for between 4 and 123 minutes. A 1.64 nm native oxide layer was identified on top of the substrate with refractive index between Si and SiO_2 due to incomplete oxidation. A bulk layer consisting of two oscillators matched to optical constants of type 1 and type 2 diamond was added on top of this, with a final surface roughness EMA layer consisting of 50% bulk and 50% void. It was found that use of optical constants from a Tauc-Lorentz oscillator fitted to polished thicker films had minimal impact on the simulated composition and absolute values. An iterative fitting process as detailed in Figure 5.3 was applied. Addition of a void and glassy carbon component to the bulk EMA layer resulted in a reduction in MSE, as did removal of the native oxide and addition of a silicon carbide layer, attributed to the etching of the native oxide and carburisation previously observed in hydrogen and methane containing plasmas [135, 142].

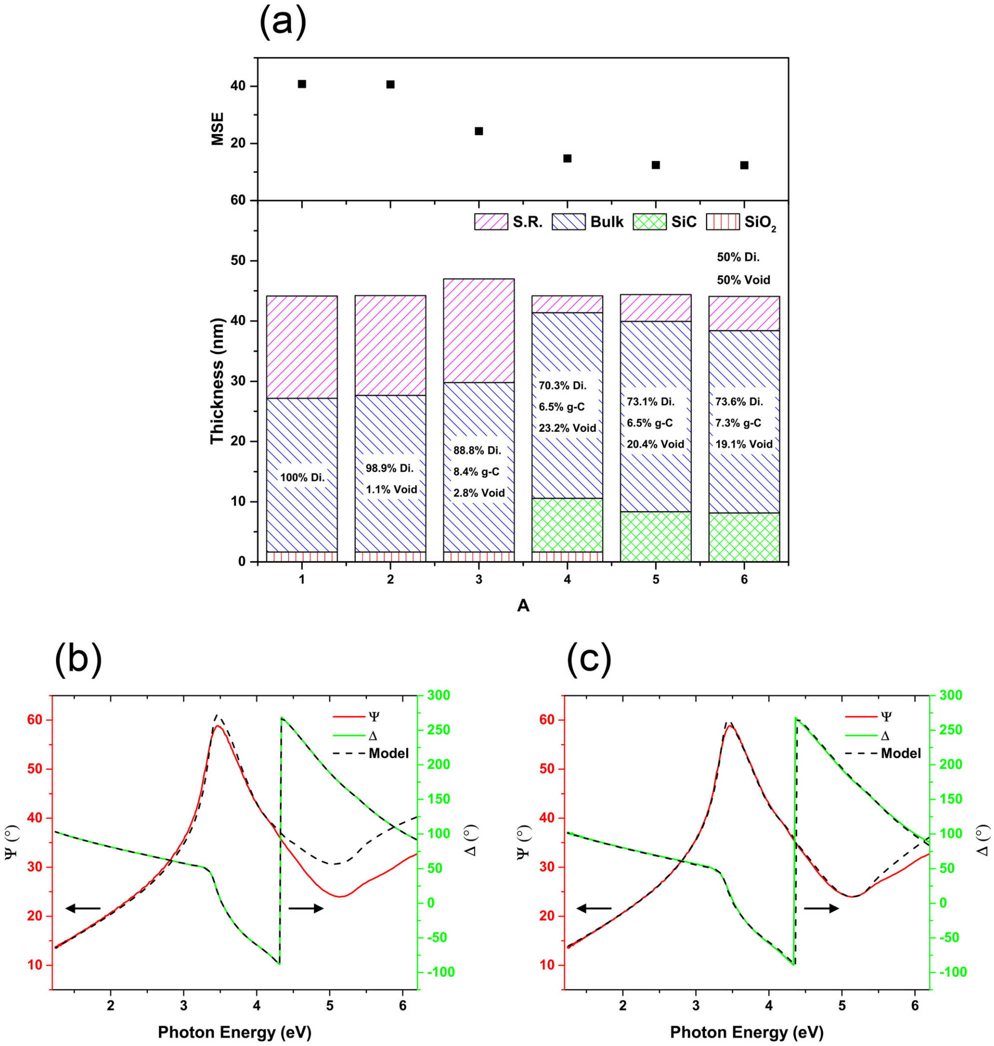

Figure 5.3: a) The iterative fitting process applied to the SE data, featuring the evolution of the model composition and illustrating the decreasing mean square error (MSE) with improvement of the model. b) Simulated spectra of the first model fitted to SE data c) Simulated spectra of the final model fitted to SE data. Reproduced with permission from [131].

After the optimal structure had been identified, optical constants of the carbide and non-diamond content were varied using reference dielectric functions of amorphous SiC, alpha-SiC, various forms of diamond-like carbon, tetrahedral amorphous carbon, and graphite from literature. Changes to the optical constant of the non-diamond material in the bulk EMA resulted in variance of the concentration of non-diamond material in the samples, as previously observed by Cella et al. [132]. The trend with growth duration remained the same, and changes in the MSE were relatively minor, although it was found that that the glassy carbon optical function best followed the composition trends identified through Raman spectroscopy, so this was used to approximate sp^2 content in the final model. During variance of the SiC optical constant, all except the beta-SiC optical constant demonstrated inconsistent trends in surface roughness compared with AFM data.

The seed layer was found to be best modelled by an EMA layer of 4.38 nm thickness, with 54.9% void content 4.5% glassy carbon content, on top of a 1.64 native oxide layer. Trends in SE-derived parameters for samples grown at different duration are shown in Figure 5.4. Over the first 8 minutes of exposure to growth conditions, the thickness of the top layer increased to approximately 30 nm whilst decreasing in void content to 28.8%, suggesting lateral Volmer-Weber island growth. The ratio of glassy carbon to diamond content remained constant over this period. After 13 minutes of growth, the SE model required the addition of a surface roughness layer. This correlated with a peak in roughness observed by AFM. After this point, the bulk thickness began to rapidly increase. Such a peak in SE roughness has previously been observed in in-situ studies of nanocrystalline growth and has been deduced to be a result of crystallites reaching a maximum size prior to the coalescence and formation of a complete film [2, 11].

5.1.3 Microcrystalline and Thicker Nanocrystalline Films

Whilst a Bruggeman EMA allows for calculation of optical constants of diamond films comprised of multiple phases, it is only valid under the following conditions: The size of phases in a composite material must be significantly greater than atomic sizes, but smaller than one tenth of the probing wavelength, and the dielectric functions of phases must be independent of size and shape [85]. As the thickness of nanocrystalline films increases, overgrowth of the competing crystallites can lead to values of surface roughness in excess of 100 nm. If this roughness is greater than 30% of the probing light wavelength, multiple scattering from

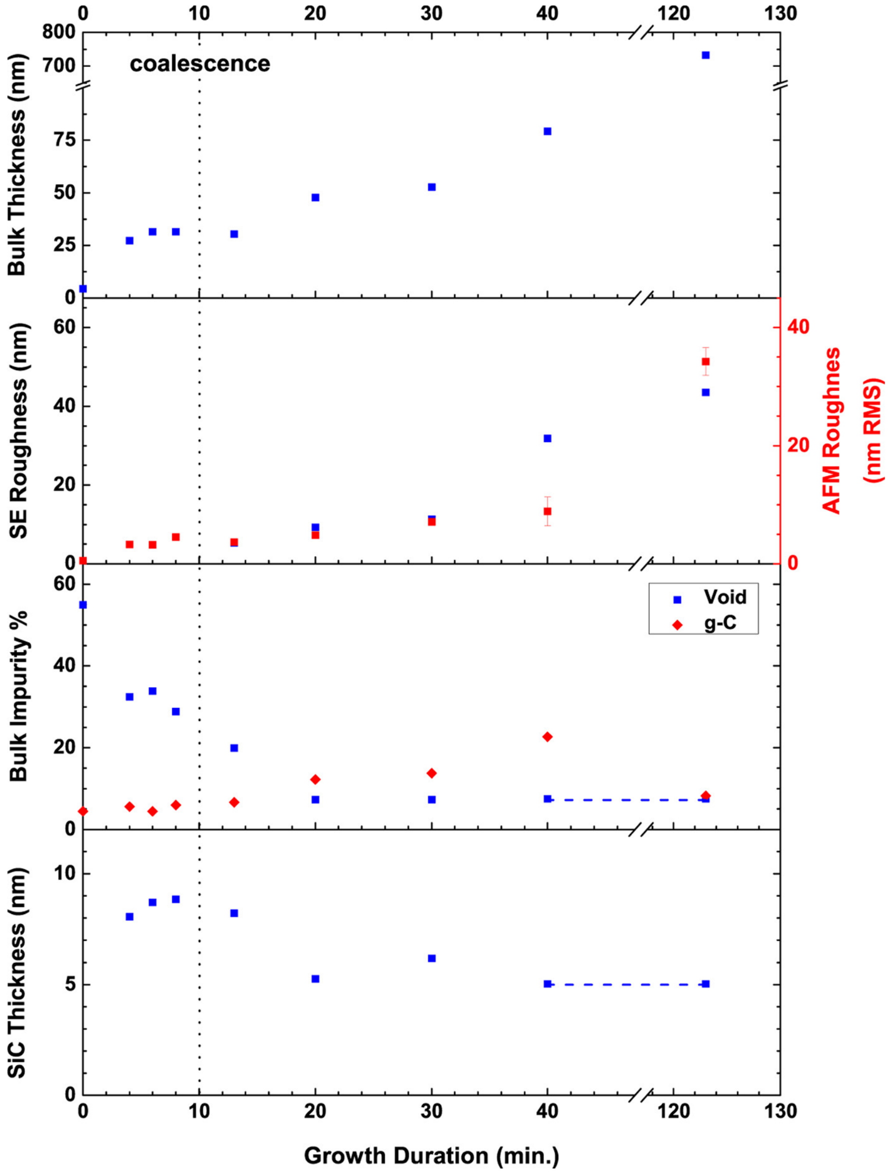

Figure 5.4: Trends in the SE-derived parameters for the seeded substrate and samples grown for 4-123 minutes. The dashed line indicates the point of coalescence, after which a second EMA layer was required to model the surface roughness. Reproduced with permission from [131].

the crystallite peaks can cause significant depolarisation of the reflected light [85, 133].

Cella et al. [132] performed SEon a series of films between 0.6 and 2 μm thick, grown using MPECVD on silicon substrates seeded using a 45 μm diamond powder in alcohol solution in an ultrasonic bath. AFM measurements indicated a relatively thin surface roughness with some deeper canyons. To account for this, an SE model was constructed involving two surface roughness layers consisting of diamond and void: A layer consisting of 38% void atop a layer with 9% void content. The average thickness of these layers was 27 and 47 nm respectively.

The impact of scattering of incident light and EMA breakdown can be avoided by extending wavelengths into the infrared region of the spectrum. Such an approach was taken by Wang et al. [149], who carried out SE at wavelengths between 3-12 $/mu$m for films approximately by hot filament CVD and MPECVD. SE modelling using reference optical constants from literature indicated the presence of a 879 nm surface layer, comprised of an EMA mixture of diamond on void atop a 12 μm bulk diamond layer. This long-wavelength SE displayed limited sensitivity to thin layers, and the inclusion of a SiO_2 layer did not significantly impact the error of the fit, making it very difficult to characterise the interfacial region between film and substrate. Fang et al. [150] also carried out infrared SE on films grown on silicon substrates, identifying a 12 μm thick bulk diamond layer, with a rough surface layer of approximately 870 nm thickness and 28% void content.

Cifre et al. [151] avoided the issues posed by surface roughness by carrying out SE of the much smoother substrate side of the film (Figure). The front surface of the film was embedded in a polyester resin. The silicon substrate was then removed by chemical etching with a hydrofluoric acid/nitric acid/acetic acid solution, exposing the smoother nucleation side of the film. This side of the film turned out to have a roughness sufficiently low so as to avoid depolarisation due to scattering. SE, in combination with x-ray diffraction, allowed for the detection of a 25 nm thick seed layer comprised of beta-SiC, glassy carbon and air on top of an approximately 5 μm thick bulk layer.

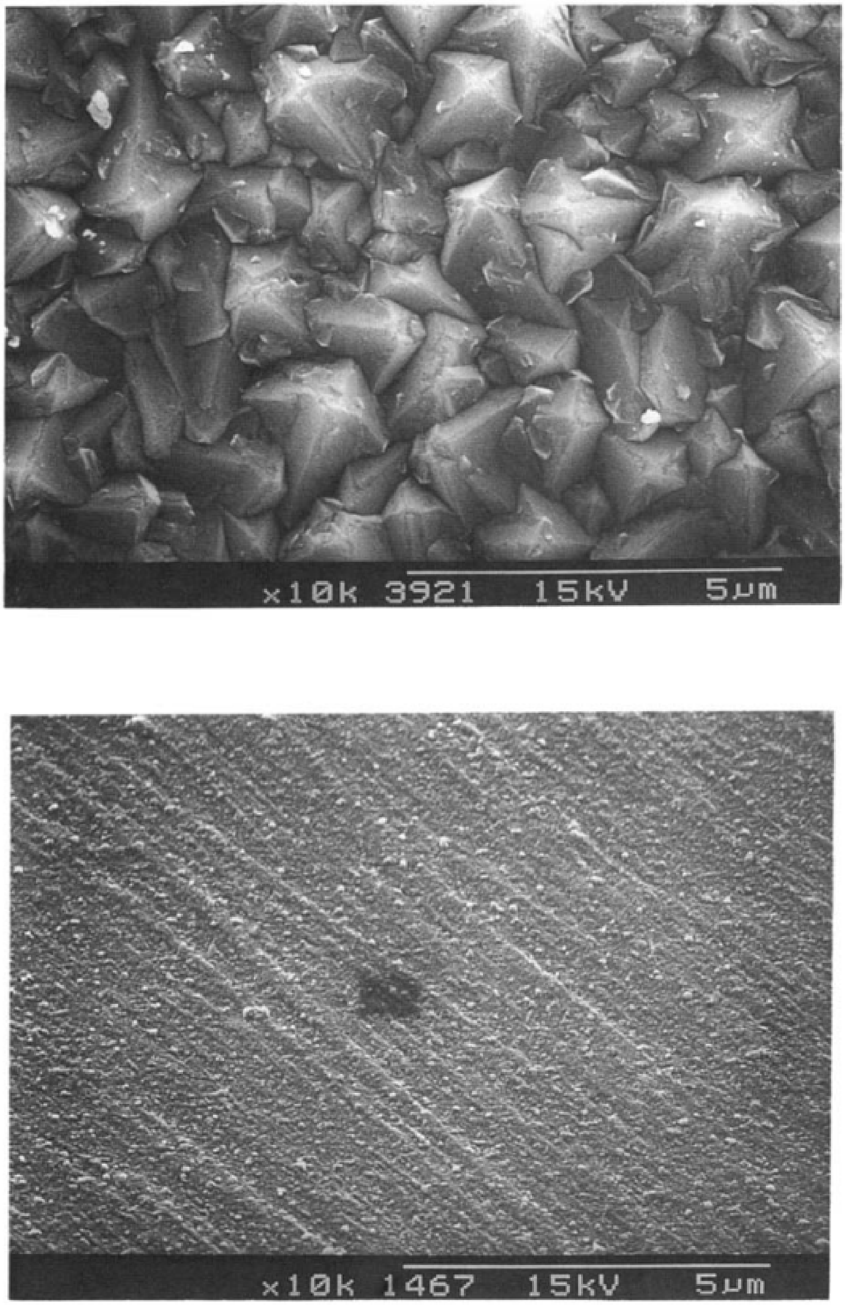

Figure 5.5: SEM images of the front surface of the film (top) and the much smoother substrate side of the film (bottom). Reprinted from J. Cifre et al., “Spectroscopic ellipsometry measurements of the diamond-crystalline Si interface in chemically vapour-deposited polycrystalline diamond films”, Diamond and Related Materials, Diamond 1992 **2**, 728–731 (1993). © 1993 by the American Physical Society.

Whilst it has been demonstrated that SE can be performed to some degree of success on thicker nanocrystalline and microcrystalline films, the issues encountered with such an approach indicate that the technique is more suited to the characterisation of early stage diamond growth, prior to the development of significant surface roughness.

5.1.4 *In-Situ* Characterisation

Ex-situ work has provided insight into the diamond growth process by CVD, but ultimately real-time monitoring is necessary to allow for greater control over the early stages of growth. Although the resolution of such monitoring is limited by the acquisition time of the ellipsometer, With acquisition times as short as 1 s demonstrated [13] (corresponding to approximately 0.3 nm of growth at a typical growth rate of 1 μm hour^{-1}) SE is clearly suitable for real-time growth monitoring.

The elevated substrate temperature at diamond growth conditions will affect the optical constants of the silicon substrate. To obtain the dielectric function of the substrate at high temperatures, Hong et al. [2] subjected an unseeded silicon wafer to growth conditions. With the very low nucleation density of diamond on unseeded wafers [51, 55], diamond growth did not impact SE spectra prior to thermal equilibration. Temperature calibration of the substrate was possible useing a well-defined feature in the silicon substrate optical function, found at approximately 3.37 eV at 25 °C. This feature caused by the E_1 transition along the Λ direction in the band structure [140, 152]. The energy position of this transition decreases linearly with increasing temperatures, from 3.23 eV at 36 °C to 3.04 eV at 830 °C [152] (see Figure 5.6). From this, the temperature of the substrate can be calculated using critical point analysis to extract the position of the E_1 peak. Such a method extracts the temperature within approximately $3\alpha^{-1}$ of the surface. α^{-1} is the absorption coefficient of the substrate at the E_1 energy, approximately 20 nm, so the temperature measured is within 60 nm of the surface [2, 11].

Hong et al. [2] applied *in-situ* SE to silicon substrates seeded by mechanical scratching at growth temperatures of 626 and 841 °C, with a gas flow ratio of 1%

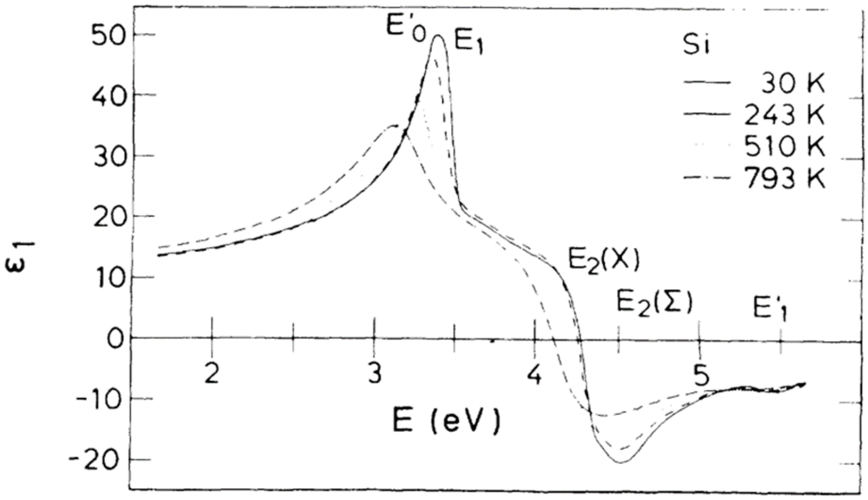

Figure 5.6: Dielectric function of silicon at various temperatures. Used with permission from the American Institute of Physics, from P. Lautenschlager et al., "Temperature dependence of the dielectric function and interband critical points in silicon", Physical Review B **36**, 4821–4830 (1987). Permission conveyed through Copyright Clearance Centre, Inc.

$[CH_4]/([CH_4]+[H_2])$. A four layer model was developed (Figure 5.7). The first layer was a crystalline silicon substrate, with a disordered amorphous silicon layer on top of this. A low-density roughness EMA layer made up of amorphous silicon, crystalline silicon and void was added to simulate damage to the substrate by the seeding process. Finally, a surface oxide layer was added atop the stack. This model was validated with AFM measurements. The proposed model was able to describe the seeded substrates without the inclusion of any carbon material in the simulation. This is because the complex nature of the damaged substrate surface layers, and the similarity of low density a-Si and sp^2 optical functions made the detection of sp^2 material impossible. Similarly, any diamond layer is difficult to discern from a surface dielectric layer, voids or surface roughness. The maximum potential volume fraction of carbon was estimated to be 0.08, which was not anticipated to be optically detectable.

Using dielectric constants of the silicon substrates at elevated temperatures, in-situ SE data was analysed using regression analysis with one and two layer models of the diamond film, with an EMA made up of optical constants of diamond, void, and glassy carbon. At the point of coalescence, a surface roughness

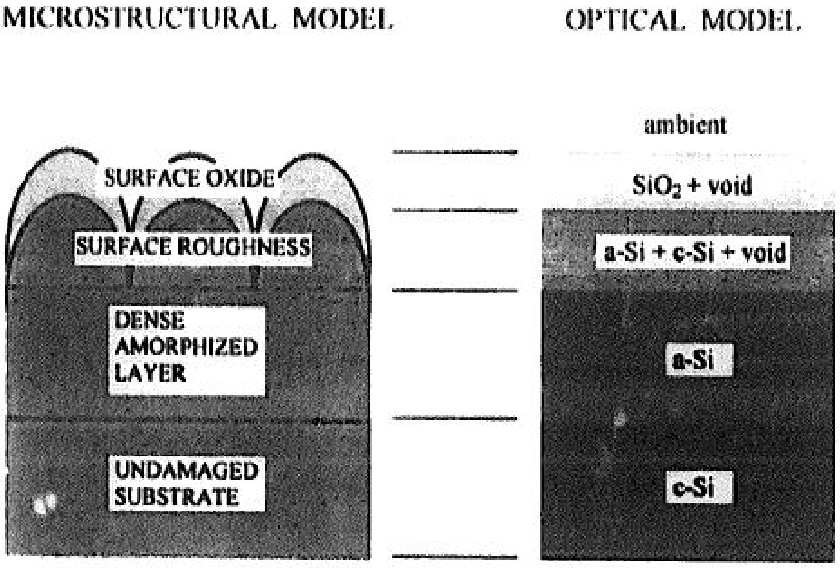

Figure 5.7: The microstructural model developed for the seeded silicon wafers, and the optical model used by Hong et al. to simulate this during fitting of SE data. Reprinted from Diamond and Related Materials 6, B. Hong et al., "Effects of processing conditions on the growth of nanocrystalline diamond thin films: real time spectroscopic ellipsometry studies", 55–80, © 1997, with permission from Elsevier.

layer made up of 50% diamond and 50% void was added. Parameters derived from this model are shown in Figure 5.8. Films were grown to approximately 220 nm thickness. In the initial stages of growth, the damage to the substrate from the seeding process made it impossible to determine volume fractions of void and sp^2, requiring these to be fixed. In the early stages of growth, the nucleation layer increased in thickness. The rate of this growth increased by a factor of approximately 12 with the temperature increase from 626 to 841 °C. By comparison, the rate of bulk layer growth only increased by a factor of 1.4. Coalescence was identified to occur at the point at which the void fraction in the nucleation layer dropped to 50%, predicted by modelling of hemispheres on a square grid. The contact thickness of the film grown at 841 °C predicted by SE matched grain sizes determined by cross-sectional transmission electron microscopy.

Following coalescence, a number of changes in composition were observed. Most notably, the sp^2 volume fraction significantly increased, suggesting that this non-diamond content is formed in between grains during the coalescence pro-

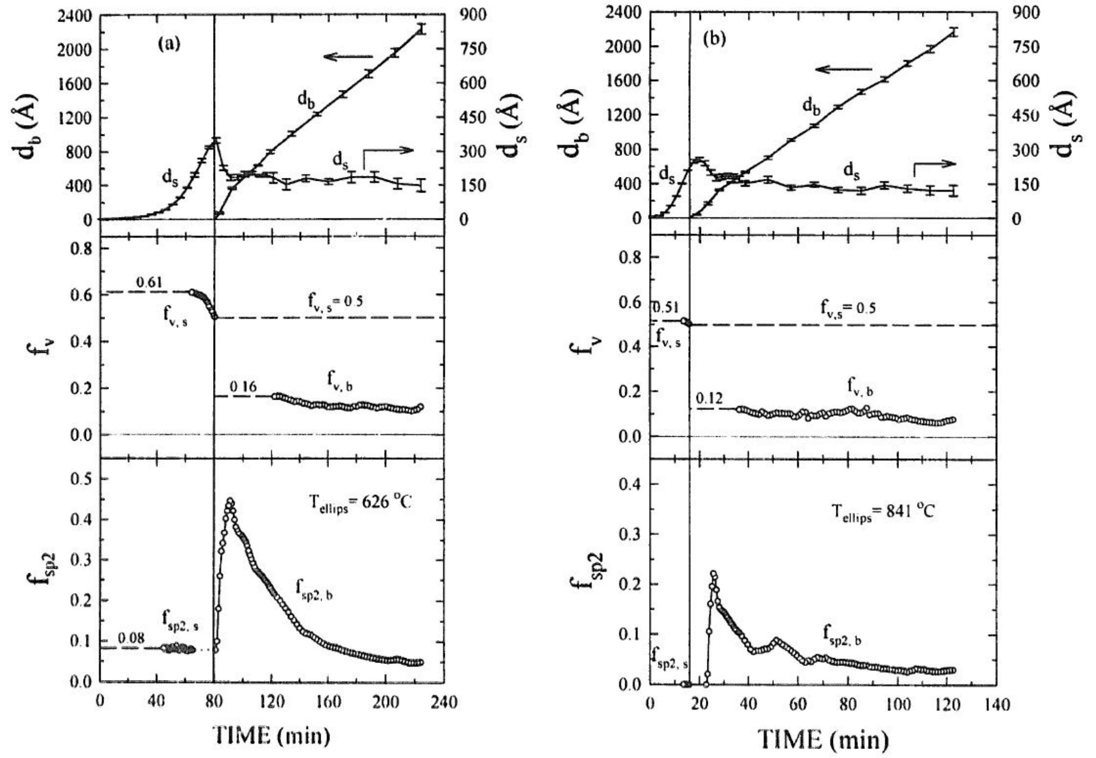

Figure 5.8: The changing SE-derived composition of the deposited nanocrystalline diamond film at substrate temperatures of 626 °C (left) and 841 °C (right). The vertical line indicates the point of coalescence, at which point a second EMA layer was required to model the bulk growth. The top panels show the thicknesses of the nucleation/surface roughness (d_s) and bulk (d_b) layers, whilst the bottom two panels show the volume fractions of void (f_v) and sp^2 (f_{sp2}) content in the nucleating (s) and bulk (b) layers. Horizontal dashed lines indicate times for which the composition could not be determined and so was fixed to allow for calculation of the thickness. Reprinted from Diamond and Related Materials 6, B. Hong et al., "Effects of processing conditions on the growth of nanocrystalline diamond thin films: real time spectroscopic ellipsometry studies", 55–80, © 1997, with permission from Elsevier.

cess. The volume fraction of sp^2 increase during coalescence was observed to be temperature dependent, with the peak sp^2 content decreasing from approximately 45% in the 626 °C growth to about 20% in the 841 °C growth. Surface roughness was seen to decrease by 10-20 nm due to the joining of islands into a complete film. After this, the bulk film thickness linearly increased, whilst surface roughness remained relatively stable and the sp^2 content decreased rapidly. This decrease in sp^2 volume fraction with increasing thickness suggests that most of the sp^2 content exists in the first 30 nm of the film.

A number of films were grown using different gas concentrations. As anticipated, an increase in the ratio of $[CH_4]$ to $([CH_4]+[H_2])$ from 1% to 6% resulted in an increase in the volume fraction of sp^2 in grain boundaries close to the interface from 23% to 34%. In addition to this, the rate of decrease in sp^2 content over time was lower, and the proportion of sp^2 in the final film increased from 2% to 16%. The authors suggested that the slower decay of sp^2 with increasing $[CH_4]$ to $([CH_4]+[H_2])$ ratio indicated that the sp^2 propagates throughout the film during growth. In films grown with higher levels of CH_4, a slight increase in contact thickness was observed, although this was at least partly attributed to the limited reproducability of the the seeding process.

In-situ SE has proved successful for the study of early-stage diamond growth by MPECVD. However, analysis of the seeding and nucleation has been limited by the substrate damage by mechanical abrasion process used to seed the substrate prior to growth, preventing determination of bulk volume fractions prior to coalescence. More recent developments in seeding techniques have produced methods that do not cause damage to the substrate, such as seeding with diamond nanoparticles [120]. In the next section of this chapter, these seeding methods are combined with *in-situ* SE to provide insight into the nucleation and early stages of diamond film growth.

5.2 *In-situ* Spectroscopic Ellipsometry of Diamond Growth on Silicon

5.2.1 Experimental Methodology

All samples were grown on 15 × 15 mm, 0.5 mm thick polished P-type Si {100} wafers. To ensure a uniform oxide layer thickness and remove any organic contaminants, wafers were cleaned using the RCA SC-1 process [153, 154]. Silicon substrates require pre-treatment to result in sufficient nucleation densities for the growth of coalesced diamond films [51, 119]. This was done by immersing substrates in a hydrogen-terminated/DI H_2O colloid for 10 minutes, a technique known to result in seeding densities in excess of 10^{11} cm^{-1} [120].

Growth was carried out in a Carat Systems CTS6U clamshell-type MPECVD reactor, at a microwave power of 3 kW and a chamber pressure of 55 Torr. Substrate temperatures were measured at approximately 710 °C using a WilliamsonIR Pro92 dual-wavelength pyrometer. This relatively low substrate temperature was chosen to result in a slower growth rate and therefore greater resolution for the in-situ SE monitoring. 5 samples were grown for durations of 5–30 minutes at 3% methane diluted in hydrogen. 2 further growths were carried out to investigate the effect of a variance in methane flow rate, one for 30 minutes at 5% methane, the other for 90 minutes at 1% methane. The plasma was sparked at a microwave power of 1.5 kW and chamber pressure of 15 Torr, with microwave power and chamber pressure ramped up to growth conditions over a period of 3 minutes. This ramp up in power and pressure was software-controlled to ensure that the process was uniform for all samples. The growth timer was started at the conclusion of this ramp as soon as the microwave power and chamber pressure reached growth conditions. Methane concentration remained constant throughout the spark, ramp up and growth process. At the end of each growth, samples were cooled in a purely hydrogen-fed plasma to reduce the formation of non-sp^3 material.

SE was performed both *in-situ* and *ex-situ* with a J. A. Woollam M-2000D rotating compensator ellipsometer and CompleteEASE software over a wavelength range of 300-1000 nm. *In-situ* spectra were taken through fixed fused silica viewports at an angle of incidence of approximately 66 °, with an acquisition time of 1 s. Figure 5.9 shows the experimental setup used for collection of *in-situ* data. *Ex-situ* spectra were taken at incidence angles of 65, 70 and 75 °. An iterative fitting process within the CompleteEASE software was used, with various sample structures iterated to minimise the difference between simulated and measured spectra. This fitting process is detailed later on in the chapter.

Raman spectroscopy was performed using a HORIBA LabRAM spectrometer using an excitation wavelength of 473 nm, chosen to maximise sensitivity to both sp^3 and sp2 carbon [95]. AFM was performed using a Bruker Dimension Icon microscope equipped with a ScanAsyst tip in peak force tapping mode.

5.2.2 Model Development

Ex-Situ spectra of the 20-minute growth duration sample were used to develop an optical model for characterisation of other samples, with an iterative fitting process used to minimise the MSE between measured and modelled spectra. Figure 5.10 shows the development of this model through the fitting process.

The first iteration of the model consisted of a bulk layer comprising two oscillators matched to optical constants of type I and II natural diamond [136] atop a silicon substrate [134], resulting in an MSE of over 100. This model was therefore unsuitable for the characterisation of this sample. Addition of a layer to account for surface roughness, a Bruggeman EMA made up of 50% void and 50% bulk layer, resulted in a huge reduction in MSE to 25.72. A further reduction in MSE by almost 50% to 13.66 was achieved by changing the bulk layer to a second EMA, mixing optical constants of diamond and void, with the bulk void fraction allowed to vary. The optical constants of glassy carbon [137] have previously been shown to be a good approximation for sp^2 material within the bulk layer [131]. Addition of this third component to the bulk EMA again reduced the MSE to 10.18.

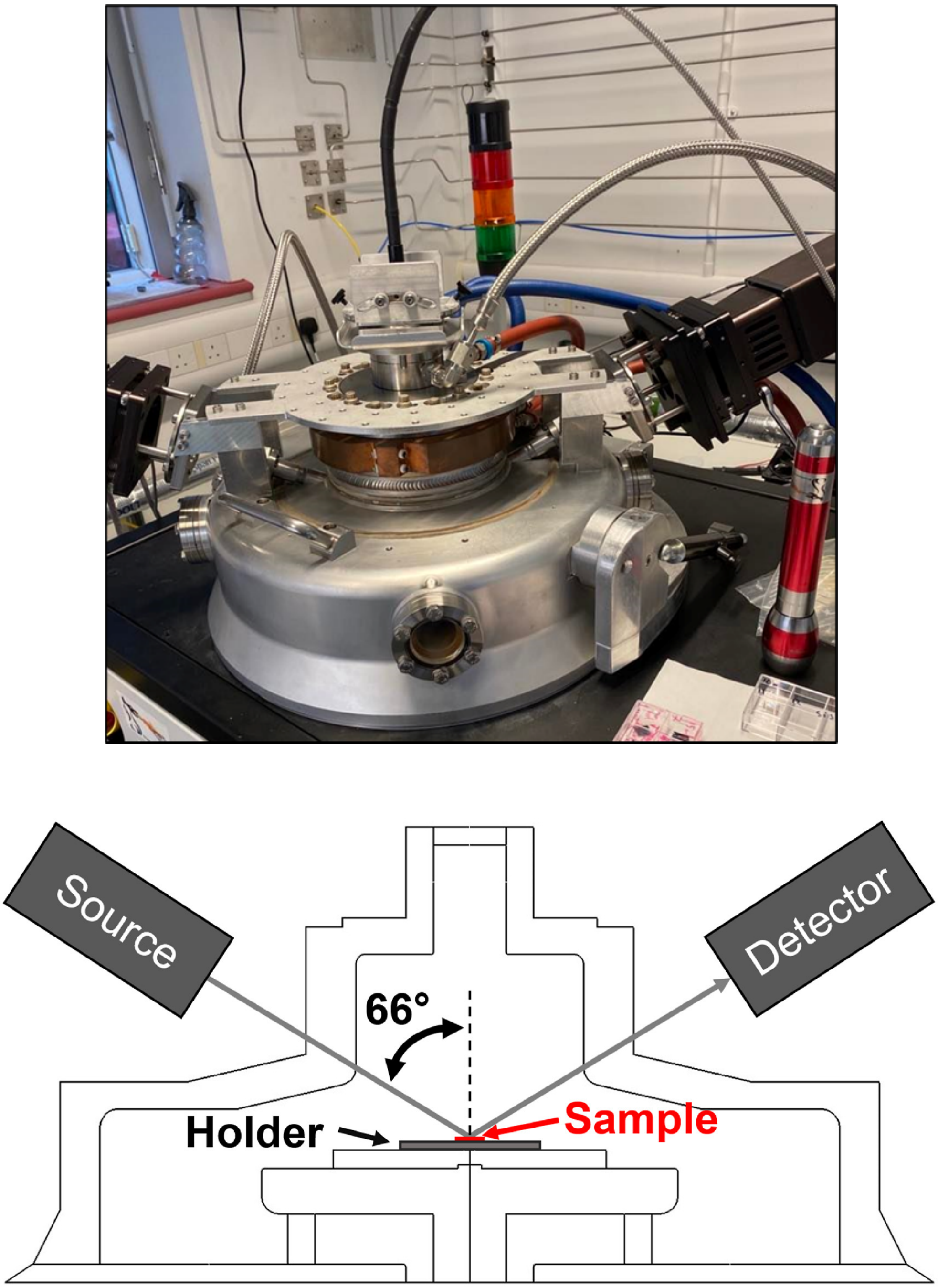

Figure 5.9: Top: Reactor with SE mounted for collection of *in-situ* spectra. Bottom: Schematic of the reactor setup, with the thickness of the sample exaggerated for visibility.

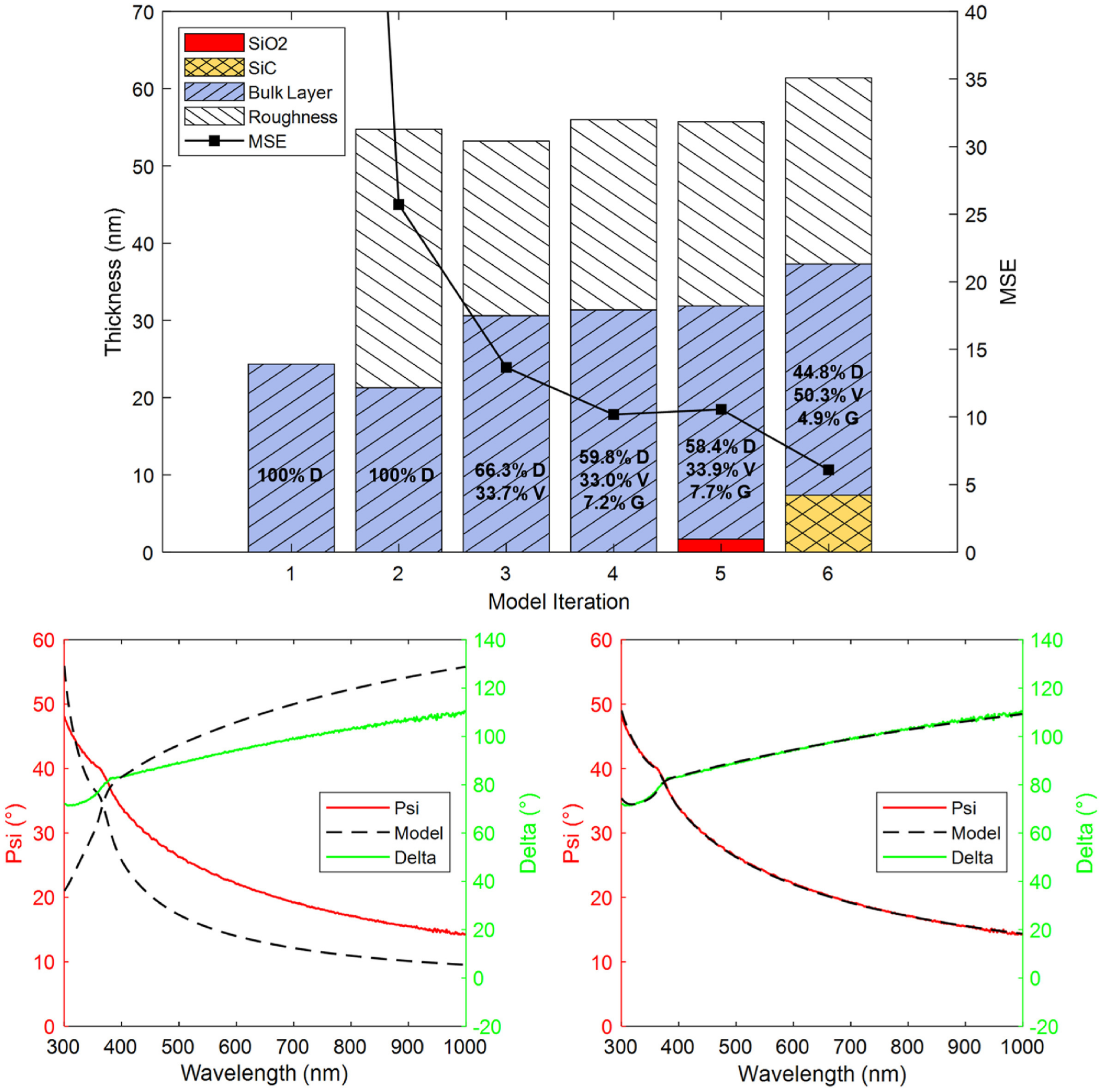

Figure 5.10: Top: Development of the model fitted to the 20-minute growth duration sample, showing MSE, layer thicknesses, and bulk layer diamond (D), void (V) and glassy carbon (G) content for each iteration of the model. Bottom: Comparison of the modelled parameters with measured parameters at an incidence angle of 70 ° for the first iteration (left) and final iteration (right).

Prior to seeding, a 1.69 nm-thick native oxide layer was observed on the surface of the silicon substrates by SE. However, addition of this to the optical model of the 20-minute sample increased the MSE, so this was not included in future iterations. Such etching of the native oxide layer is typical of H_2 and H_2/CH_4 plasmas [142, 155]. Previous XPS and SE studies have also identified the existence of a sub-10 nm amorphous SiC layer in the early stages of diamond growth, resulting from carburisation of the silicon substrate [58, 131, 135]. The inclusion of such a layer (modelled using optical constants of cubic SiC [136]) reduced MSE to 6.09. The thickness of this SiC layer was 7.38 nm. When applied to samples with a growth duration of 15 minutes or less, removal of the surface roughness layer did not significantly impact MSE, so was unnecessary to include when characterising these samples.

5.2.3 Application to *In-Situ* Spectra

The application of the model to in-situ data required several additional considerations. The in-plane window effects were accounted for using spectra of a reference sample as detailed in [156]. Substrate temperatures routinely exceed 700 °C at MPECVD growth conditions [2, 51, 121, 123], influencing the optical properties of the substrate. However, as the refractive index of nanocrystalline diamond films does not vary substantially with temperature [157], it was not considered necessary to vary the optical constants of the film components. Similarly, the optical constants of the SiC layer were not varied because the trajectories of ellipsometric parameters are very close together for extremely thin films [87].

The substrate temperature at growth conditions was extracted using a library of temperature-dependent optical constants of silicon within the CompleteEASE software, built by interpolating optical constants at known temperatures using an algorithm based on the critical point shifting algorithm detailed in [158]. Whilst this method proved effective at accounting for the changes in optical constants of the substrate in the ramp up and very early stages of growth, a high level of parameter correlation between the temperature and bulk glassy carbon fraction was observed as the film approached coalescence. Parameter correlation is the result of the data fitting process where the sensitivity of multiple parameters (in this case bulk glassy carbon fraction and temperature) exhibits the same spectral signature, meaning that the parameter values determined are not unique; there are multiple combinations of substrate temperature and bulk glassy carbon fraction values that provide the same quality of fit. As a result of this, it was necessary to fix the substrate temperature parameter. This was fixed from a point 1 minute after the completion of the ramp up in power and pressure, to allow the temperature time to equilibrate. This was justified by comparing the SE-derived temperature to the temperature measured by the dual-wavelength pyrometer. In the case of the latter, the apparent temperature remained constant following the initial ramp. It is therefore significantly more likely that the changes in the SE spectra are the result of compositional changes in the film than the result of substrate temperature changes. A constant substrate temperature is to be expected at this point, as the microwave power and chamber pressure conditions remained constant following the ramp up to growth conditions.

As with the *ex-situ* modelling process, the addition of a surface roughness layer to the model was unnecessary in the early stages of growth. This was included from 18 minutes onward, the point at which its inclusion reduced MSE by more than 10%. This was consistent with *ex-situ* characterisation, which did not require a roughness layer after 15 minutes but did after 20 minutes. The two different models and the differing morphology of the samples they are fit to are shown in Figure 5.11.

Figure 5.12 shows parameters from the *in-situ* SE model for a sample of growth duration 30 minutes at a methane concentration of 3%. A high level of parameter correlation between the bulk layer thickness and void content was evident in the first 4 minutes of growth. This resulted in a model that suggested an unrealistically thick bulk layer with very high void content, illustrating the importance of validating SE models of complex sample structures with alternative measurement techniques. After 4 minutes, the level of parameter correlation decreased, resulting in a more realistic bulk thickness and void content. From approximately 18 minutes of growth, a parabolic decrease in the bulk void fraction is seen as the

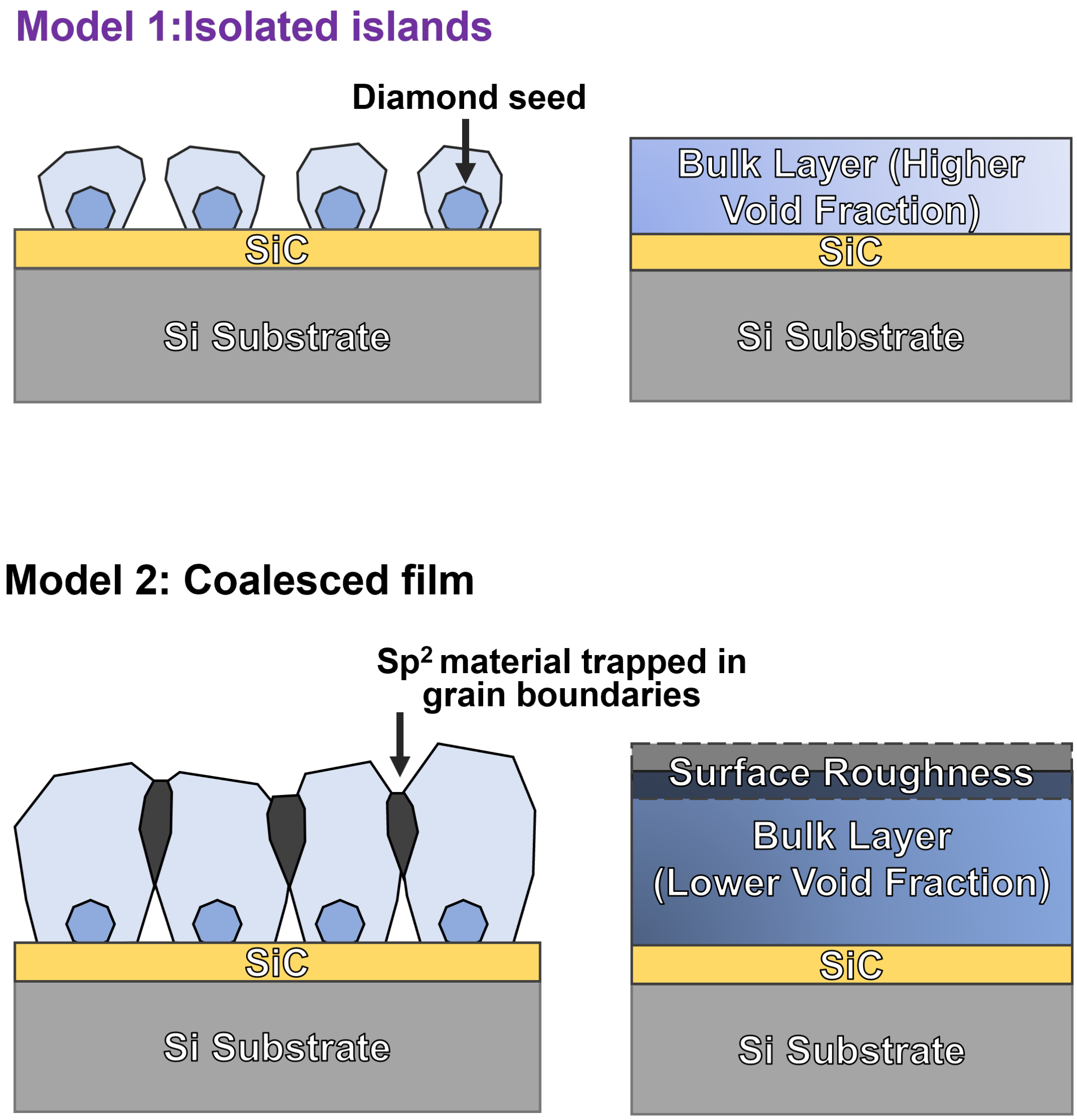

Figure 5.11: Schematic of sample structures (left) at different stages of the growth process and the optical models used to fit them (right).

individual islands expand laterally. Just before 25 minutes, a peak in glassy carbon content of approximately 23.5% is seen, due to the trapping of non-diamond carbon in grain boundaries following the coalescence of the individual crystallites into single film. The parabolic decrease in bulk void content followed by a peak in sp^2 content at the point of coalescence matches observations from previous studies [2, 11, 131]. The individual islands can be modelled as hemispheres on a grid. Assuming a hemispherical grid, a highly efficient spacing, contact between the islands would occur at a void fraction of 40%. In reality, the islands are not as efficiently spaced or perfectly hemispherical. The contact between islands, marked by the beginning of a steep increase in void fraction and corresponding increase in sp^2 fraction, occurs at approximately 50% void fraction. This is closer to the contact point of 48% void fraction predicted by modelling the islands as hemispheres on a square grid, which is a less efficient spacing.

The SiC layer increased in thickness up to the point of coalescence, before starting to decrease in thickness following coalescence. This trend matches previous SE analysis of early-stage diamond growth on silicon seeded with diamond nanoparticles [131]. When comparing *in-situ* and *ex=situ* data, it can be seen that the *ex-situ* model suggests a higher void fraction and lower glassy carbon fraction prior to coalescence. It is likely that this is at least partially the result of the process of cooling in a hydrogen plasma, which is known to preferentially etch non-diamond carbon [135, 159]. Immediately prior to and following coalescence, the reduction in this glassy carbon fraction is not seen. This is due to coalescence resulting in the trapping of sp^2 carbon within the grain boundaries, where it is not accessible to the plasma, so no etching occurs.

A peak in the thickness of the roughness layer was also seen around the point of coalescence, as the crystallites reach a maximum size prior to forming a coalesced film. This roughness decreased after coalescence, before again increasing due to the overgrowth of competing crystallites [160].

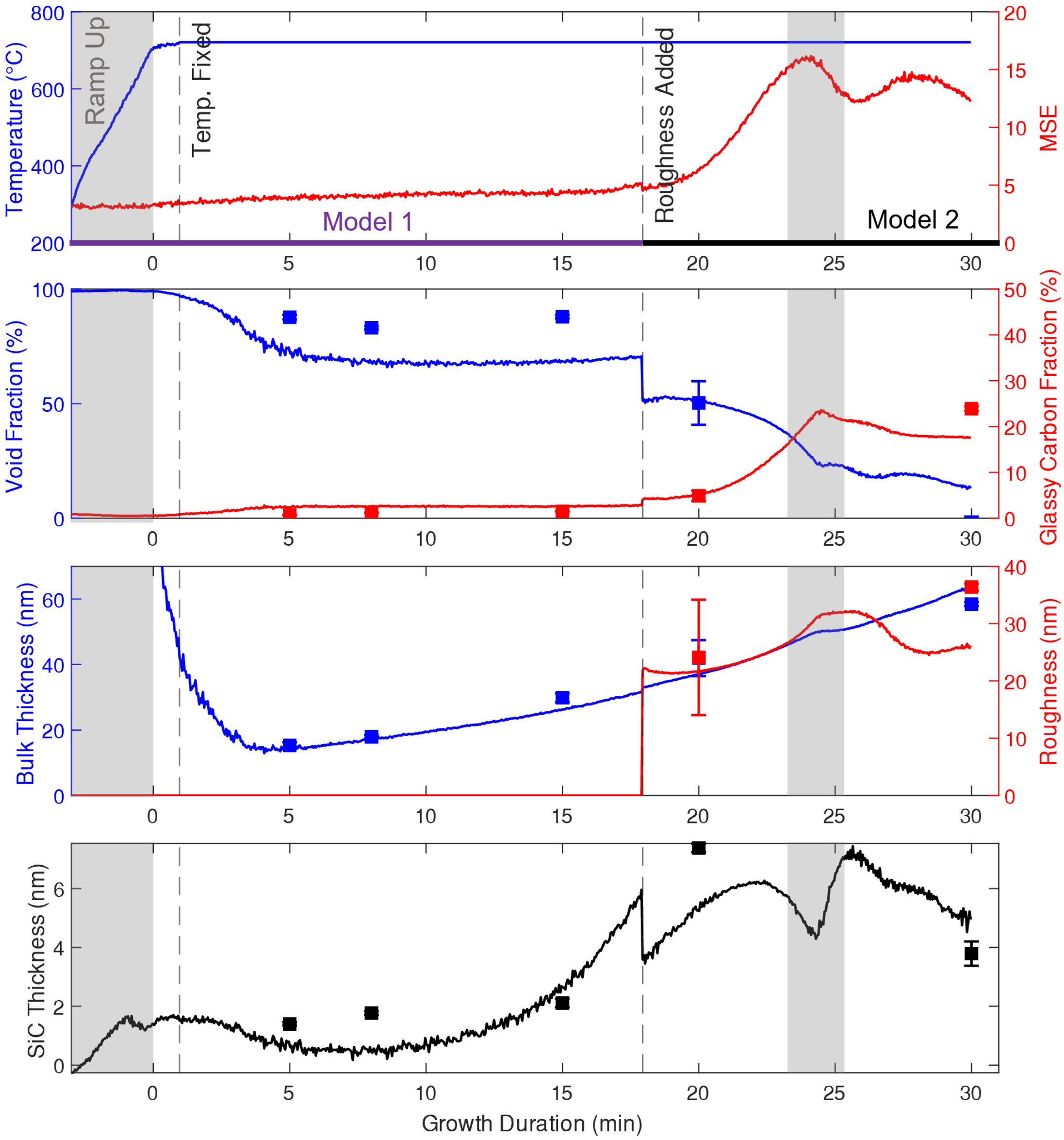

Figure 5.12: *In-situ* SE-derived data from a 30-minute growth at 3% methane concentration. From top panel: SE-measured temperature and MSE; bulk layer impurity fractions; bulk thickness and surface roughness; SiC layer thickness. X-axis colours in the top panel indicate the SE model used to fit the different stages of the growth process, with the two models used shown in Figure 5.11. The square points plotted in the bottom three panels are from *ex-situ* spectra of samples grown for the same duration.

5.2.4 Model Validation

Given that the quality of the parameters obtained from SE spectra are only as good as the model used to fit them, it is important to validate the accuracy of the model. In this case, the model was validated using Raman spectra and AFM images. Figure 5.13 shows *ex-situ* Raman spectra of several samples with growth duration from 5-30 minutes, normalised to the second-order silicon Raman peak at 950 cm^{-1}. The second-order Raman peak was used because the laser intensities and exposure times required to generate sufficient signal from the components of the diamond film resulted in an intensity of the first-order peak great enough to saturate the detector. As is to be expected for such early stage diamond growth, the most significant peaks in the spectrum are from the silicon substrate; the first and second-order Raman peaks at 520 and 980 cm^{-1} [161], with the minor peak at approximately 830 cm^{-1} also a component of the second-order silicon spectrum [162, 163]. The two peaks at 620 and 644 cm^{-1} result from local vibrational modes of boron atoms within the doped silicon substrate [164, 165].

Raman peaks from the diamond film are more visible in the magnified spectra. Note that these are offset for clarity. The first order diamond Raman peak at 1332.5 cm^{-1} is only visible from 20 minutes onward. This corresponds with the SE model, which indicates an increase in bulk diamond content from approximately 18 minutes. By 30 minutes, the diamond Raman peak intensity has significantly increased, consistent with the SE model indicating coalescence just before 25 minutes, with the corresponding increase in bulk layer diamond content at this point. As is typical for nanocrystalline films, the first-order diamond Raman peak exhibits broadening due to the limited thickness and crystallite size [9, 138].

In-plane stretching of pairs of sp^2 sites results in the G-band, which is seen in all samples at approximately 1450 cm^{-1}. Whilst this would be typically seen closer to 1560 cm^{-1} [9], the downshift in the position of this peak indicates an increased level of disorder within the sp^2 component of the film, suggesting that is more amorphous in nature [9]. The G-band is more intense in the 30-minute sample. The G-peak, the result of bond-stretching of pairs of sp^2 atoms rings and chains

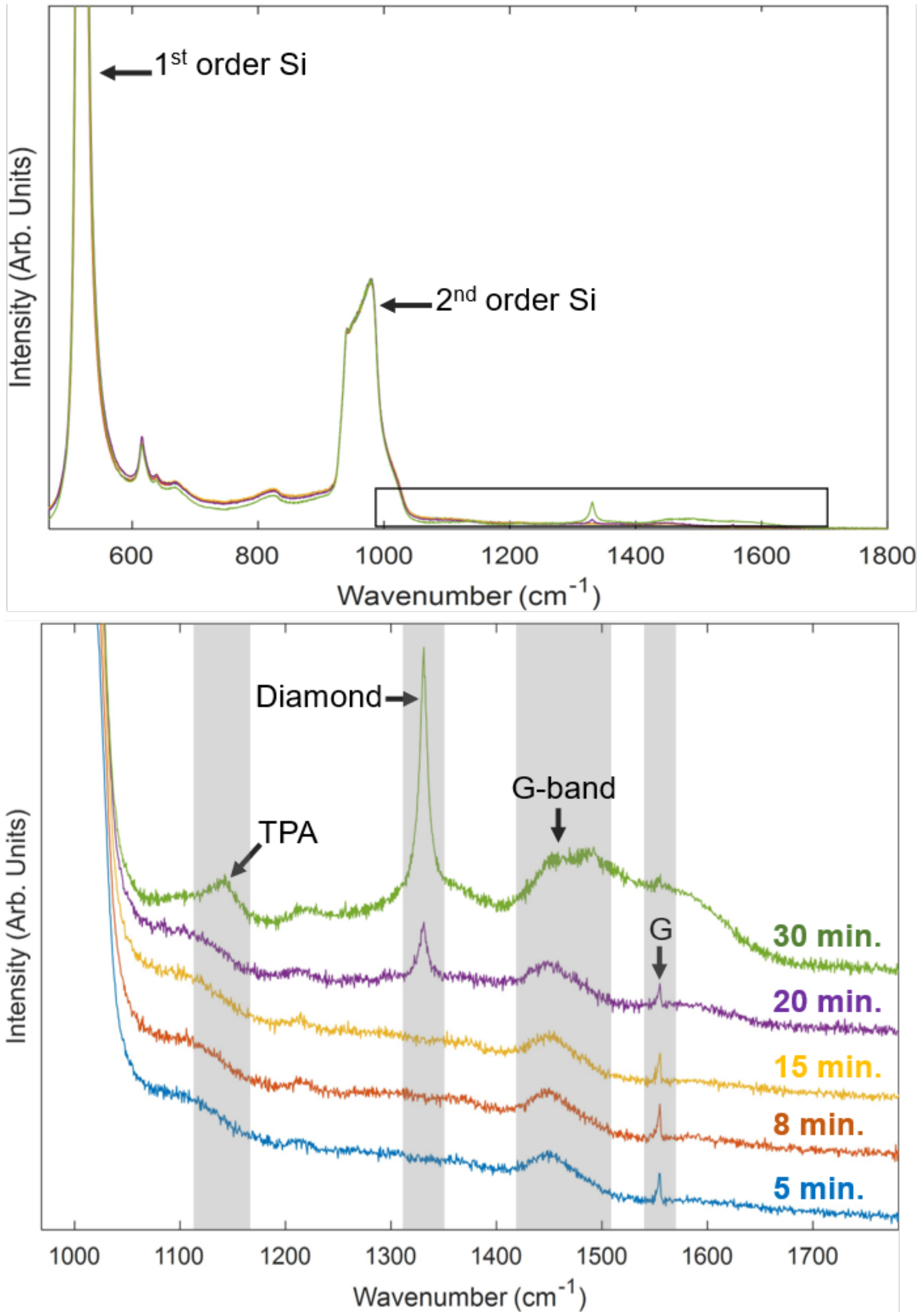

Figure 5.13: Top: *Ex-situ* Raman spectra of samples with varying growth duration, normalised to the second-order silicon Raman peak. Bottom: Magnified view of the same spectra (region indicated by the box above), offset for clarity.

[96] is seen in all samples at 1555 cm^{-1}.

Only visible in the 30-minute growth duration sample is a peak at 1140 cm^{-1}. This is assigned to *trans*-polyacetylene, which is present within the grain boundaries [8]. As this peak does not appear in the 20-minute sample, this suggests that coalescence (resulting in the formation of grain boundaries) occurs between 20 and 30 minutes, which is also consistent with the SE model's indication that this occurs just before 25 minutes. Whilst this peak is always accompanied by a second peak at 1450 cm^{-1}, the latter is obscured by the G-band in this case.

Figure 5.14 shows AFM images of samples grown for durations between 5-30 minutes, with Figure 5.15 showing the Root Mean Square (RMS) roughness and maximum roughness depth (R_{max}) of the same samples. In the 5-minute growth duration sample, individual islands are visible. It can be seen that as suggested earlier, these islands are not regularly shaped or evenly spaced. The lateral sizes of these islands increase with growth duration, with a coalesced film evident by 30 minutes, as suggested by the SE model and Raman spectra. As is expected, the RMS roughness increases with growth duration, with the rate of increase greater in the first 15 minutes of growth. The peak in RMS roughness immediately before coalescence seen in previous *ex-situ* SE work [131] is not seen in this case. When comparing this result with the *in-situ* model, the reason for this becomes clear. The spike in roughness occurs between approximately 22-27 minutes, whilst the closest two AFM images to this are from growth duration of 20 minutes, before the spike appears, and 30 minutes, after the spike has disappeared. The maximum roughness depth increases with growth duration up to 20 minutes, before decreasing by 30 minutes as the voids between crystallites are filled.

5.2.5 Impact of Methane Concentration

With an SE model developed, applied to *in-situ* data and validated using alternative techniques, the logical next step is to examine the impact of varying the growth conditions on the early stages of growth. Perhaps the easiest of these to control is the methane concentration, as varying the microwave power and

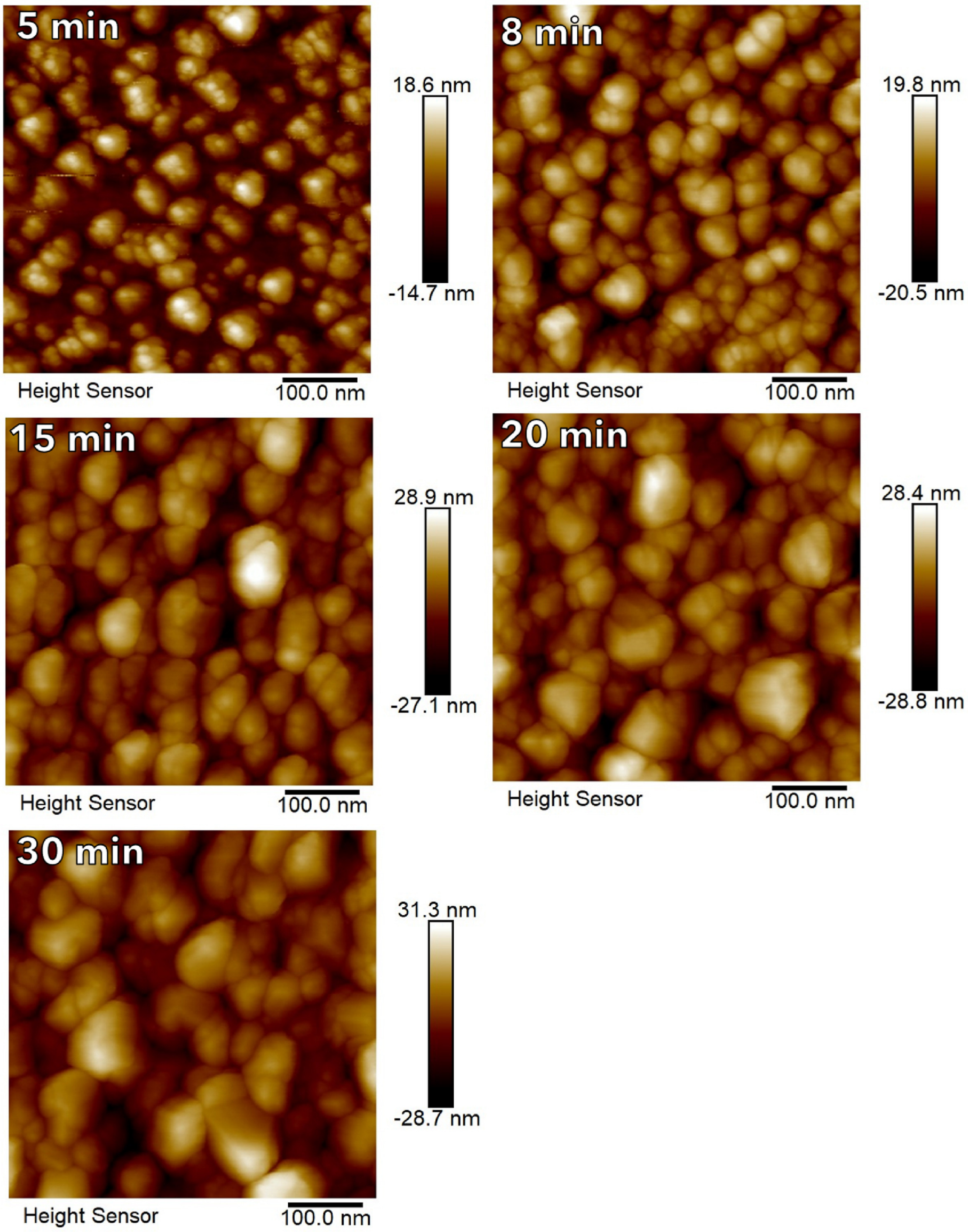

Figure 5.14: AFM images of samples grown for durations of 5–30 minutes.

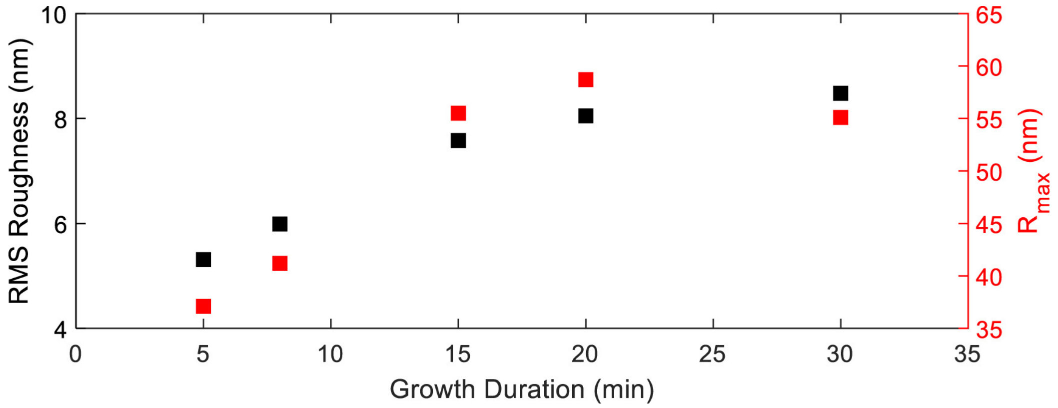

Figure 5.15: RMS roughness and maximum roughness depth for samples of varying growth duration.

chamber pressure can impact the substrate temperature distribution (this is examined in chapter 4). The methane concentration during growth is an important parameter, as it impacts the level of renucleation seen during film growth and therefore crystallite size and film sp^2 content [51].

Figure 5.16 shows *in-situ* SE-derived parameters for a sample grown for 20 min at a methane concentration of 5%. As seen in the 3% growth, high parameter correlation resulted in an unrealistically high bulk thickness and void fraction being suggested by the model in the first 2 minutes of growth. After 2 minutes of growth, the level of correlation decreased, with more realistic bulk thickness and void content values suggested by the model. As before, further parameter correlation between substrate temperature and glassy carbon fraction was eliminated by fixing the substrate temperature after 1 minute of growth. The SiC layer thickness parameter presented issues with parameter correlation not seen in the 3% growth, with a high correlation between this and the bulk thickness following coalescence. Due to this, the SiC thickness was fixed in the model prior to coalescence.

Perhaps the most obvious change with the increase in methane concentration was the point of coalescence; this occurred much earlier at around 7 min compared the almost 25 minutes seen with 3% methane. Additionally, the peak in glassy carbon content at the point of coalescence was higher with 5% methane (25.6% instead of 23.5%). It is important to note at this point that whilst the SE

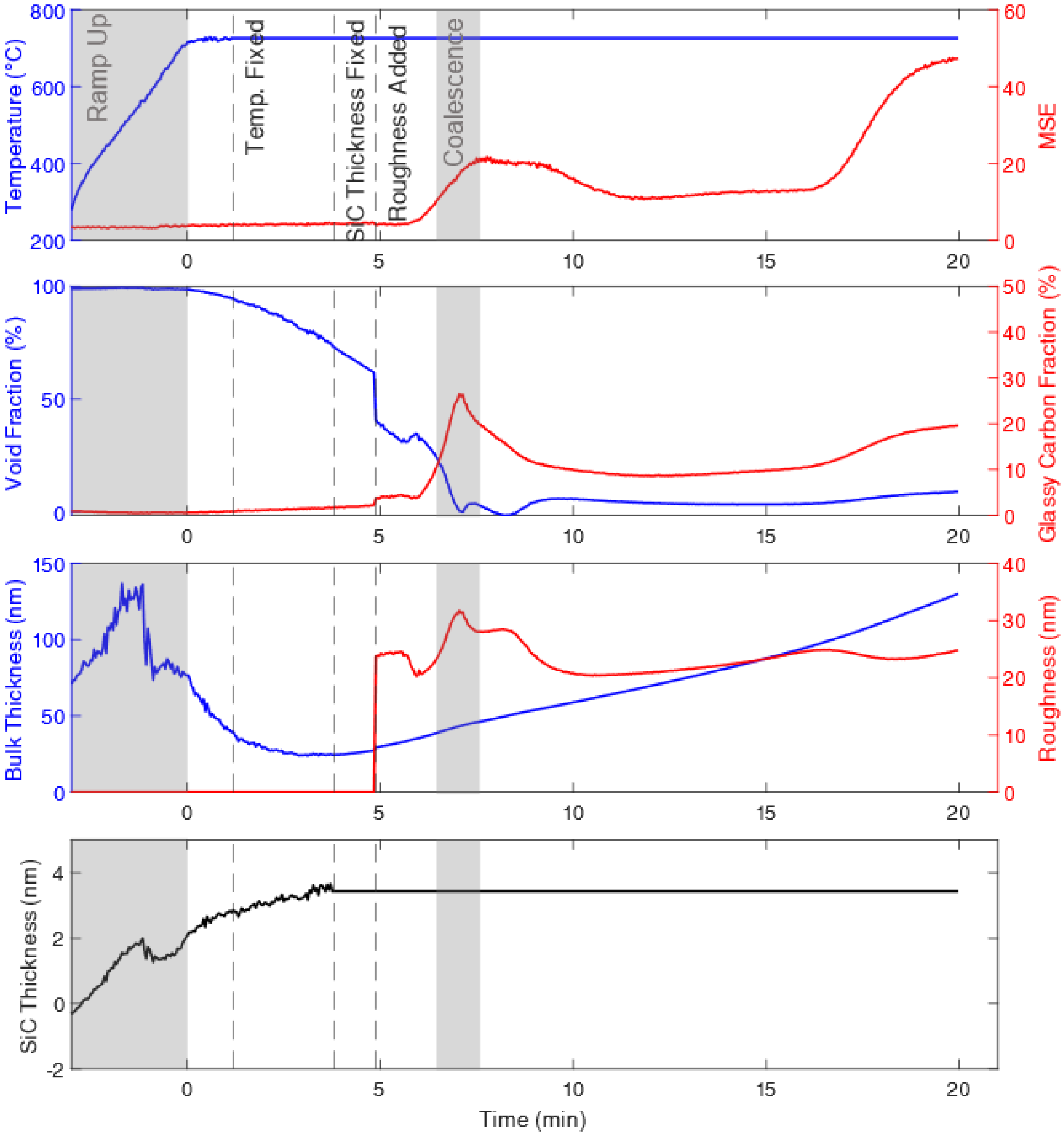

Figure 5.16: *In-situ* SE-derived parameters from a 20-min growth at 5% methane concentration. From top panel: SE-measured temperature and MSE; bulk layer impurity fractions; bulk thickness and surface roughness; SiC layer thickness.

model estimates sp^2 content within the bulk layer, the bulk composition values provided by the model are best used for comparison than as absolute compositional values. The use of glassy carbon here is only an approximation for sp^2 material within the film, as the optical constants of this are not possible to quantify. Previous work has observed that whilst changing the optical constants used to approximate sp^2 material changes the concentrations of bulk impurities, the trends seen are similar [131, 132]. The higher glassy carbon fraction seen in the model is the result of increased renucleation, a process enhanced by a greater methane concentration [51], which leads to increased levels of sp^2 bonding. The earlier coalescence and greater sp^2 fraction is consistent with previous *in-situ* observations by Hong et al. [2, 11].

Following coalescence, he growth rate at higher methane concentration was significantly faster than at 3%. From approximately 16 minutes onwards, the MSE began to increase as a result of depolarisation caused by the increase in surface roughness from overgrowth of crystallites. This roughness causes scattering of the incident light, and limits the use of SE for the characterisation of the later stages of growth.

Figure 5.17 shows *in-situ* SE data for a sample grown for 90 minutes at a methane concentration of 1%. Immediately obvious is that the point of coalescence is significantly later than in either of the other two growths. The peak in glassy carbon previously indicative of coalescence did not begin to appear until 60 minutes, with an initial peak at around 75 minutes taken to be the point of coalescence. Unlike the other two growths, an initial increase in void content is seen up to 30 minutes, and the bulk thickness at coalescence is greater. This is likely due to etching of the diamond seeds by the plasma, which can occur at low methane concentrations and results in a lower nucleation density [54]. These are not the only differences between the growths. At 1% methane concentration, the glassy carbon concentration continued to increase following coalescence, although there is some level of correlation between this parameter and the surface roughness layer thickness, which may explain the observation. A slightly greater MSE is seen following coalescence here. The slow growth rate as as result of the relatively low substrate temperature and methane concentrations makes an increase in gradient of the bulk thickness due to the switch to columnar growth particularly visible at around 70 minutes. Long incubation periods typically result in a slightly thicker SiC layer forming on the silicon substrate [55], and this is seen here with a slightly thicker SiC layer at the time of fixing than in the 5% growth.

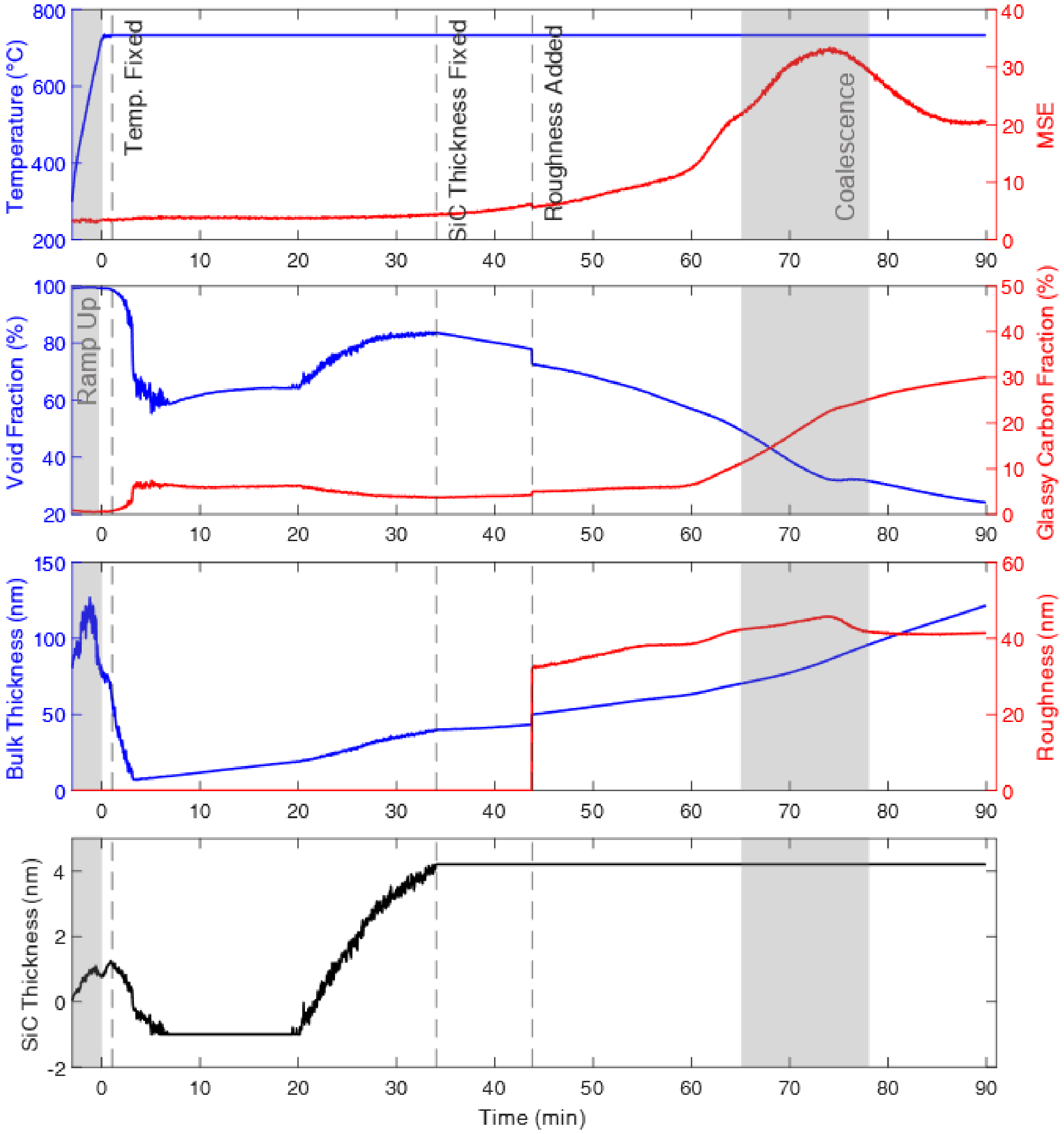

Figure 5.17: *In-situ* SE-derived parameters from a 90-min growth at 1% methane concentration. From top panel: SE-measured temperature and MSE; bulk layer impurity fractions; bulk thickness and surface roughness; SiC layer thickness.

5.3 Conclusion

SE was applied to the early stages of MPECVD diamond growth on silicon. *Ex-situ* spectra were used to develop an optical model of the substrate and diamond film, with an iterative fitting process used to refine the model, allowing a number of different parameters to vary. The model consisted of an EMA using optical constants of diamond, void and glassy carbon (approximating sp^2 content) to approximate the bulk diamond layer atop a silicon substrate, with a third layer made up of 50% void and 50% bulk to account for surface roughness. The model was modified for application to *in-situ* data, accounting for the effects of the elevated substrate temperature and reactor windows. A parabolic decrease in void content was seen, with the point of coalescence of the individual crystallites marked by a peak in bulk glassy carbon content and surface roughness. *Ex-situ* AFM images and Raman spectra of samples grown for varying duration displayed similar trends, validating the model. The impact of varying methane concentration on the initial stages of growth was also investigated using SE. An increase in the methane concentration to 5% resulted in earlier coalescence and a higher peak glassy carbon fraction, whereas decreasing the methane fraction to 1% significantly delayed coalescence.

Such application of SE to diamond growth presents a powerful tool for in-situ monitoring of the critical early stages of growth, with a sub-nanometre resolution and ability to identify changes in the composition of the film. Whilst growth on silicon is reasonably well understood, the growth on substrates such as gallium nitride and aluminium nitride is less understood, with the model of the diamond developed and validated here well-suited for application to growth on these materials, as these are often challenging to grow diamond layers on. The next chapter extends this work for SE characterisation of diamond growth on aluminium nitride.

Chapter 6

In-Situ Monitoring of Diamond Growth on Aluminium Nitride

High electron mobility transistors made from GaN display a significant reduction in device lifetime with increasing operating temperature. With the highest thermal conductivity of any known material, diamond is ideally suited as a thermal management layer. Whilst growth of thick diamond layers directly on GaN is very challenging, successful growth of thick diamond layers on AlN has been demonstrated, leading to potential diamond growth routes on an AlN interlayer atop the GaN stack. A significant limiting factor for the use of diamond in thermal management applications is the thermal barrier at the substrate-diamond interface, associated with the disordered transition region produced during the early stages of growth. The ability to monitor these early stages is therefore highly desirable to optimise growth conditions. As demonstrated in the previous chapter, SE is ideally suited to this purpose. This chapter reviews previous use of diamond thermal management layers on GaN devices, as well as diamond growth on AlN in section 6.1 and previous use of SE for characterisation of AlN films in section 6.2. Section 6.3 describes experimental work utilising SE for the monitoring of the early stages of diamond growth on AlN. *Ex-situ* spectra are used to develop an optical model of the diamond film, which is then applied to *in-situ* data and validated with AFM and Raman spectroscopy.

6.1 Diamond Thermal Management Layers on Gallium Nitride

Gallium nitride is a promising material for high electron mobility transistors in high-frequency and high-power applications [166–168]. However, increases in the operating temperature of these devices can result in a significant reduction in device lifetime [169]. Currently, thermal management solutions involve the manufacture of devices from GaN grown atop silicon carbide [170], which has a thermal conductivity of between 360-490 W/m.K [171]. The thermal conductivity of polycrystalline diamond is significantly higher, at approximately 1200 W/m.K for a 100μm thick layer [14].

In order to utilise diamond as a thermal management layer, the diamond film must be bonded to the GaN device. The bonding is incredibly important, because the thermal barrier resistance of the interface limits the thermal properties of the device [14]. Whilst wafer bonding has been utilised to realise GaN-on-diamond layers [172, 173], it has been calculated that this will result in a high thermal barrier resistance [174], necessitating an alternative approach. One such approach is through the growth of GaN on top of a single crystal diamond substrate. Hirama et al. [175] demonstrated the growth of a single-crystal AlGaN/GaN heterostructure (pictured in Figure 6.1) atop a single crystal diamond 111 substrate by Metalorganic Vapour-Phase Epitaxy (MOCVD). First, a 180 nm AlN buffer layer was deposited on the substrate, followed by the growth of 20 AlN/GaN multilayers, with the AlGaN/GaN heterostructure deposited on top of this. A thermal resistance of 4.1 K mm/W was measured, significantly lower than the 7.9 K mm/W measured for the same heterostructure grown on a SiC substrate. Whilst this approach is promising, the high cost and limited scalability of single crystal diamond are significant limitations [16].

A third approach involves the growth of diamond films on top of GaN. As with almost all heterogeneous substrates, growth of diamond on GaN results in polycrystalline films [16, 51]. Pomeroy et al. [14] deposited a 50 nm thick dielectric interlayer on top of a GaN device, with a 120 μm thick diamond film grown by

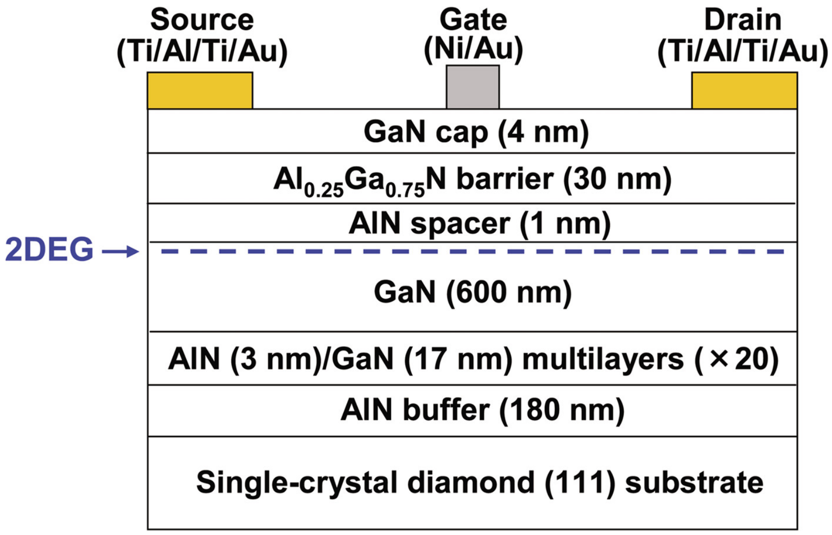

Figure 6.1: Heterostructure grown by Hirama et al., showing a GaN device grown atop a diamond substrate. Used with permission from the American Institute of Physics K. Hirama et al., “AlGaN/GaN high-electron mobility transistors with low thermal resistance grown on single-crystal diamond (111) substrates by metalorganic vapor-phase epitaxy”, Applied Physics Letters **98**, 162112 (2011). Permission conveyed through Copyright Clearance Centre, Inc.

MPECVD. However, the interlayer used acted as a thermal bottleneck, reducing the effectiveness of the diamond as a thermal management layer. A similar approach was taken by Zhou et al. [176], who utilised a 50 nm-thick layer of amorphous Si_3N_4. Polycrystalline diamond films of thicknesses between 155-1000 nm were successfully grown atop this layer, with the structure of the resulting stack shown in Figure 6.2. However, as before increased thermal resistance was introduced by the passivating Si_3N_4 layer.

A potential solution to the thermal issues presented by the interlayer is by attempting growth directly atop the GaN layer. After measuring the zeta potential of GaN films, Mandal et al. [16] achieved seeding densities in excess of 10^{11} cm^{-2} using hydrogen-terminated nanodiamond seeds on the GaN surface, which resulted in the successful growth of thin diamond films. However, the lack of a carbide bond between the GaN and diamond film as well as the differences in thermal expansion coefficients between the two makes the growth of thick diamond films directly on GaN incredibly challenging [17]. For this reason, an interlayer is still necessary, although there is room for optimisation of the interlayer material. One example of a potential interlayer material is aluminium nitride.

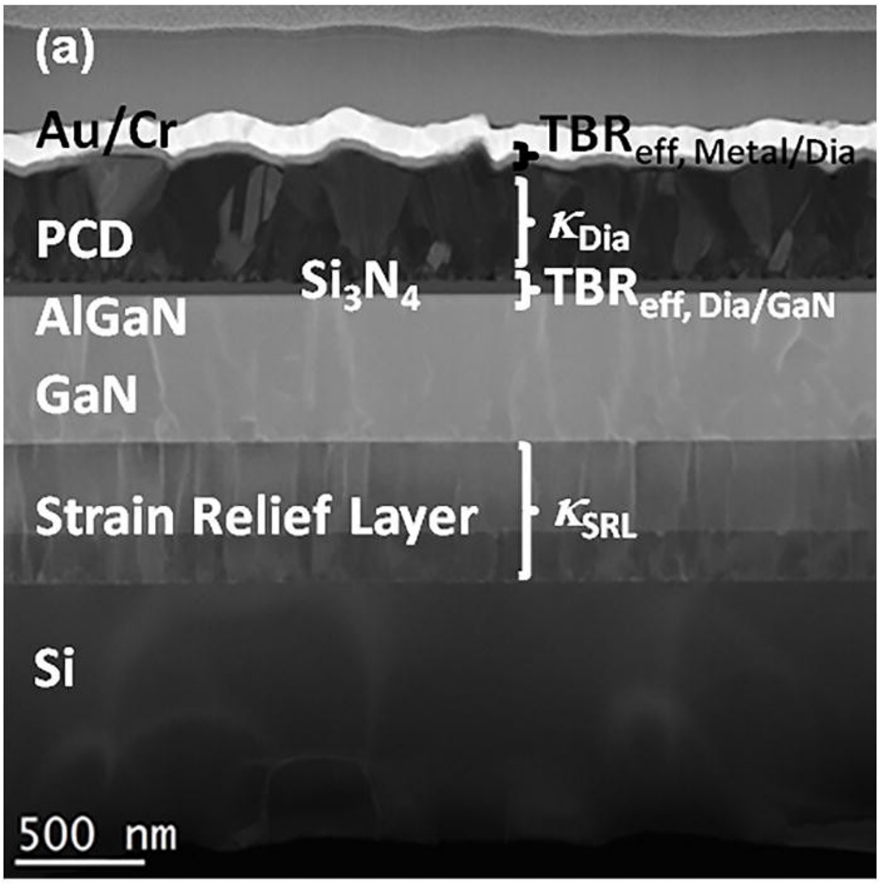

Figure 6.2: Cross-sectional TEM image of the GaN stack grown by by Zhou et al., showing a diamond layer grown atop a GaN device. Used with permission from the American Institute of Physics, from Y. Zhou et al., "Thermal characterization of polycrystalline diamond thin film heat spreaders grown on GaN HEMTs", Applied Physics Letters **111**, 041901 (2017). Permission conveyed through Copyright Clearance Center, Inc.

Using a H_2/N_2 plasma pretreatment process and oxygen-terminated nanodiamond seeds, Mandal et al. [17] demonstrated the growth of a thick polycrystalline diamond layer on an AlN substrate, with a low thermal barrier resistance measured between the AlN substrate and diamond film. Using the same seeding technique, Smith et al. [18] successfully grew a polycrystalline diamond film on an AlN interlayer atop a GaN device stack, with a high-quality interface observed using cross-sectional Scanning Transmission Electron Microscopy (STEM) (Figure 6.3).

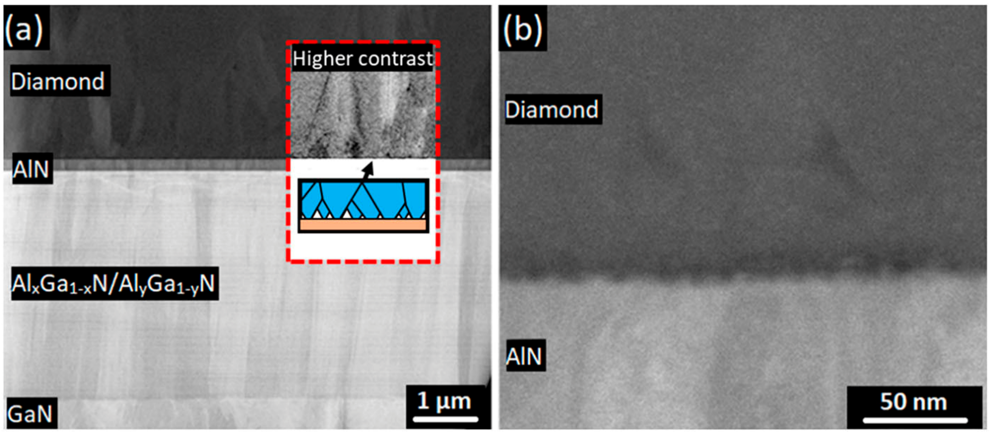

Figure 6.3: Cross-sectional STEM image of the AlN/diamond interface produced by Smith et al.. Reproduced with permission from [18].

Thermal resistance is not just introduced by the interlayer, but also by the disordered transition region of the diamond film formed during the early stages of growth [15]. For this reason, monitoring of the early stages of diamond film growth is critical. As demonstrated in Chapter 5, SE is ideally suited for *in-situ* monitoring of diamond film growth. The remainder of this chapter will discuss the use of SE for *in-situ* monitoring of the growth of diamond films on AlN.

6.2 Spectroscopic Ellipsometry of Aluminium Nitride

Whilst SE has not previously been applied to diamond films grown on aluminium nitride, it has previously been used for characterisation of AlN films. Given that the optical constants of AlN vary significantly with growth conditions [177, 178], it is impractical to utilise reference optical constants to model this layer. Previous attempts at characterisation of AlN films using SE have employed a Cauchy [179] or Cauchy-Urbach [180] dispersion to approximate optical constants of the AlN layer. The Cauchy dispersion accounts for refractive index as a function of wavelength:

$$n(\lambda) = A + \frac{B}{\lambda^2} + \frac{C}{\lambda^4} \tag{6.1}$$

Where $n(\lambda)$) is the refractive index at wavelength λ and A, B, and C are fitted model parameters. This model assumes that the modelled layer is transparent in the wavelength range used, with the extinction coefficient k assumed to be zero.

The Cauchy-Urbach model adds a second function to account for the absorption tail, with the extinction coefficient as a function of wavelength given by:

$$k(\lambda) = \alpha \exp \beta \left(12400 \left(\frac{1}{\lambda} - \frac{1}{\gamma}\right)\right) \tag{6.2}$$

Where k(λ) is the extinction coefficient at wavelength λ, α and β are fit paramaters, and γ is the band edge. These two models are only valid in the case of normal dispersion, where the refractive index increases with shorter wavelength.

The reader is referred to Chapter 5 for a discussion of the use of SE for the characterisation of diamond films.

6.3 *In-situ* Spectroscopic Ellipsometry of Diamond Growth on Aluminium Nitride

6.3.1 Experimental Methodology

The AlN layer was grown on a 150 mm Si substrate by MOCVD using an Aixtron 1x6” close coupled shower head reactor. The Si substrate was first annealed at high temperature (approximately 1070 °C) to remove the native oxide and was then exposed to a brief NH_3 flux to nitridate the Si surface. AlN growth was then initiated for 660s at a temperature of 960 °C using trimethyl aluminium as a precursor in a H_2 carrier gas, before the temperature was increased to approximately

1100 °C for the remainder of the growth process. The reactor pressure was maintained at 50 Torr.

The total thickness of the AlN layer was measured at approximately 180 nm using SE, with no significant variation seen between samples. Prior to diamond growth, samples were pre-treated for 10 minutes in a N_2/H_2 plasma as detailed in [17] to improve the adherence of the diamond film to the AlN substrate. Substrates were seeded by immersing them in a nanodiamond/DI H_2O colloid [120] and placing them in an ultrasonic bath for 10 minutes, a technique previously shown to result in high seeding densities on aluminium nitride [17]. Diamond growth was carried out in a Carat Systems CTS6U clamshell-type microwave CVD reactor, at microwave power of 3kW and chamber pressure of 50 Torr, resulting in substrate temperatures of approximately 730 °C measured using a WilliamsonIR Pro92 dual-wavelength pyrometer. Samples were grown for durations of 3-90 minutes, with a gas flow of 3% methane diluted in hydrogen. SE spectra were measured *in-situ* and *ex-situ* with a J. A. Woollam M-2000 rotating compensator ellipsometer over a wavelength range of 370-1000 nm. *Ex situ* spectra were taken at angles of 65, 70 and 75 °, with *in-situ* spectra taken through fixed fused silica viewports at an angle of incidence of approximately 66 °. A schematic of the *in-situ* SE setup is shown in Figure 6.4.

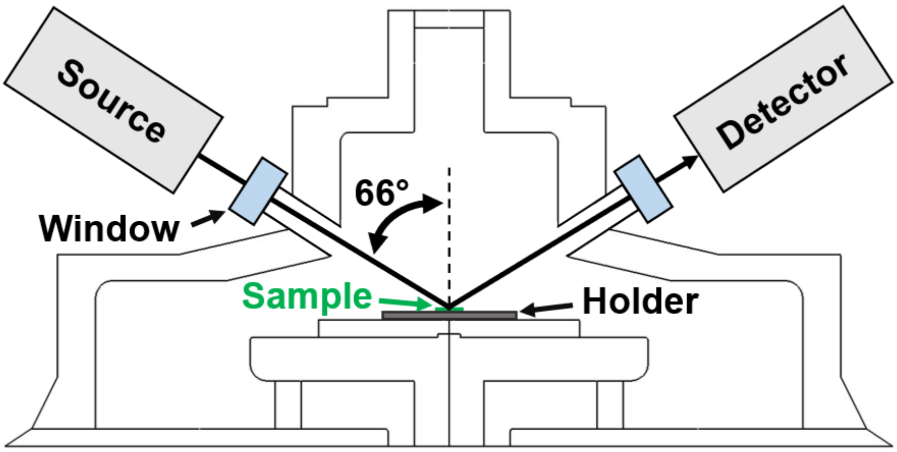

Figure 6.4: Schematic of the setup used for collection of *in-situ* SE spectra. The sample thickness has been exaggerated for visibility.

An iterative fitting process was used within the CompleteEASE software to generate a SE model for sample characterisation, with measured spectra compared with simulated spectra, and potential sample structures and parameters varied to minimise the MSE between these. Raman spectra were taken using a HORIBA LabRAM spectrometer with an excitation wavelength of 532 nm. AFM was preformed using a Bruker Dimension Icon microscope in peak force tapping mode equipped with a ScanAsyst tip.

6.3.2 Modelling the AlN Layer

An AlN sample was used to develop an optical model for characterisation of the AlN film after pre-treatment. The first iteration of the model consisted of a Cauchy layer atop a silicon substrate [134] with the A and B parameters allowed to vary, resulting in a MSE of 14.804 between measured and modelled spectra. Also allowing the C parameter to vary further reduced MSE to 10.141. The addition of an Urbach term proved unnecessary in this case, as its inclusion did not change the MSE, with the magnitude of k suggested extremely low. Finally, MSE was reduced to 8.439 by the inclusion of a 1.82 nm thick layer consisting of 50% void and 50% bulk layer to approximate surface roughness. The thickness of the AlN layer in this final iteration of the model was 179.87 nm. A schematic of this model as well as the the fit of psi and delta to SE spectra at an angle of 70° are shown in Figure 6.5, showing a good match between measured and modelled spectra.

6.3.3 *Ex-Situ* Model of Diamond Film

Ex-situ spectra of a diamond sample grown for a duration of 10 minutes were used to develop an SE model to characterise the diamond film. Figure 6.6 shows the development of this model over the fitting process. The first iteration of this model consisted of a silicon substrate [134] with a 179.87 nm thick AlN layer using the optical constants previously determined. This layer was fixed to avoid issues with parameter correlation. The diamond layer atop this was approximated using two oscillators matched to the optical constants of type I and II natural diamond [136]. The spectra simulated using this model significantly differed from mea-

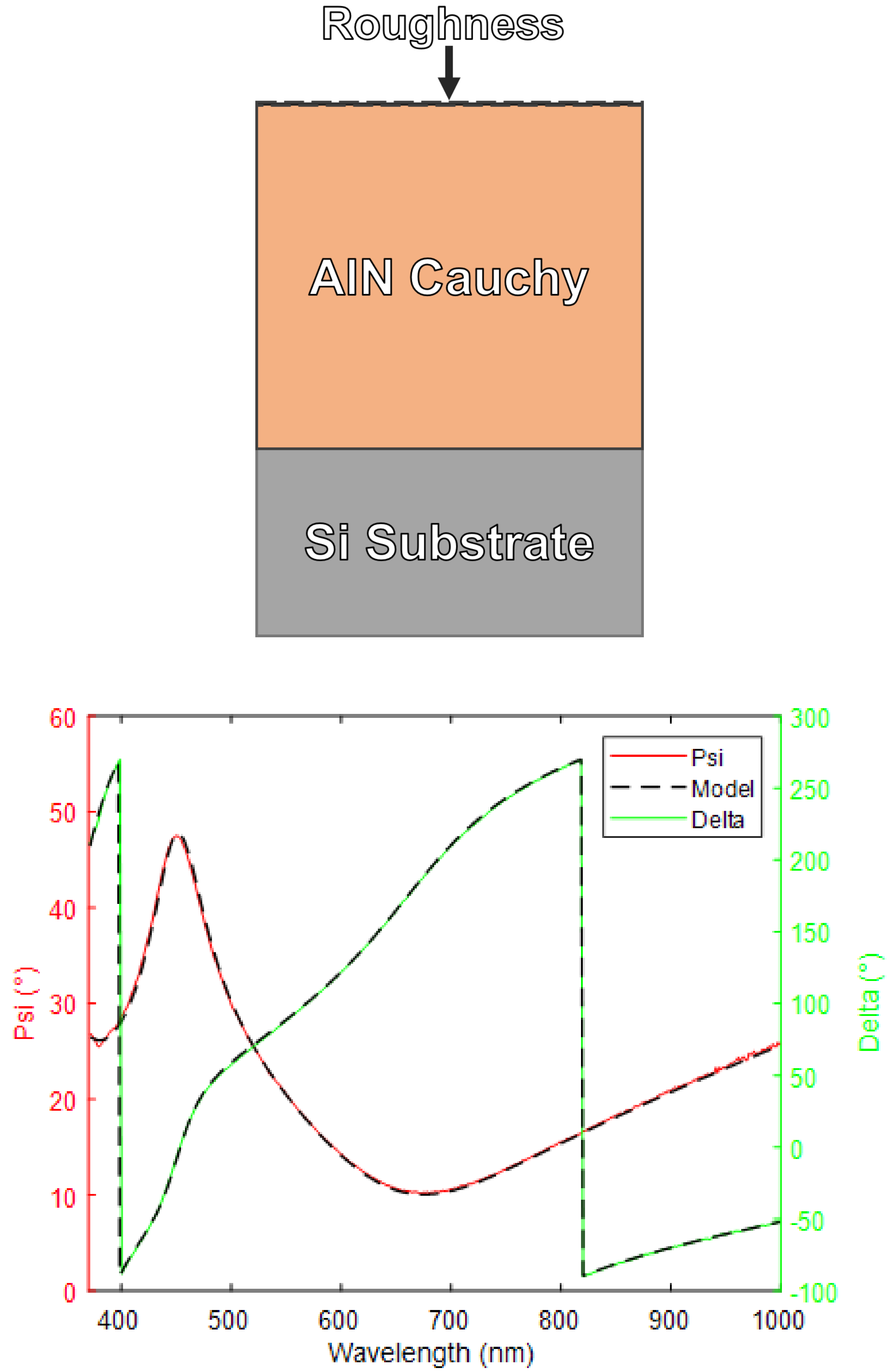

Figure 6.5: Top: Schematic of the SE model used to fit the AlN sample. Bottom: Comparison between SE model and measured spectra at an angle of 70 °.

sured spectra, with MSE exceeding 140. A very large reduction in MSE to 25.380 was achieved by accounting for void content within the bulk layer. This was done by using an EMA containing both diamond and void content to approximate this layer, with the void content allowed to vary. MSE was further reduced to 15.796 by the addition of the optical constants of glassy carbon [137] to approximate sp^2 content within the film. Previous studies have shown this to be a good approximation for non-diamond content within the film. [2, 13, 131, 132].

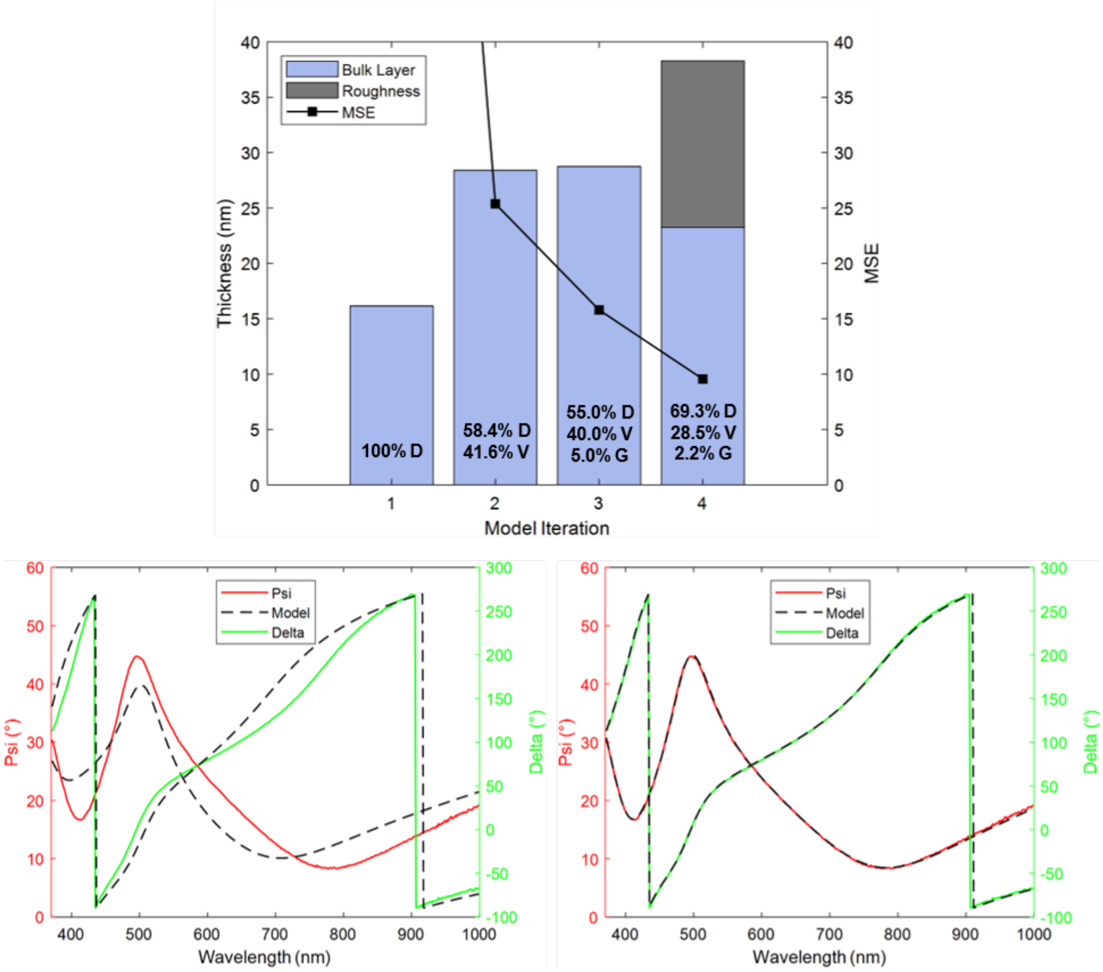

Figure 6.6: Top: Development of the model over the fitting process, showing MSE, bulk layer thickness and diamond (D), void (V) and glassy carbon (G) content for the 10-minute growth duration sample. Bottom: Comparison between measured and modelled spectra at an incidence angle of 70° for the initial (left) and final (right) models.

Finally, surface roughness was accounted for with a second EMA atop the bulk layer made up of 50% bulk and 50% void, resulting in reduction of the MSE to 9.554. Upon application of the model to samples of growth duration between 3-20

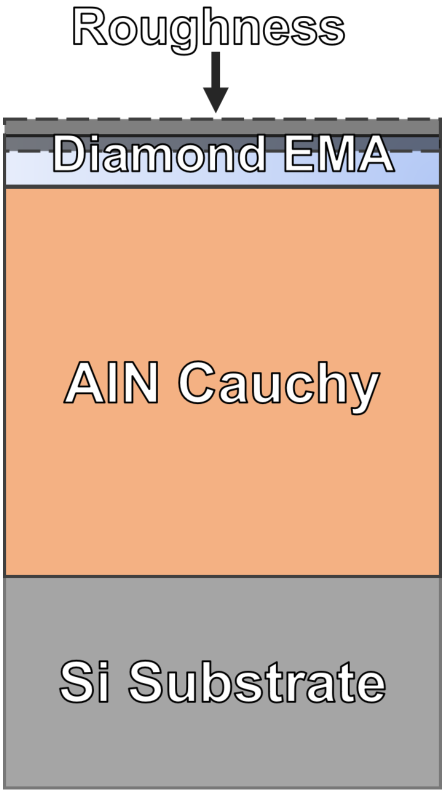

Figure 6.7: Schematic of the SE model used to fit the *ex-situ* sample.

minutes, as well as a seeded sample, it was found that the inclusion of the roughness layer was only necessary from the 10-minute sample onwards; its inclusion did not decrease the MSE of the 3-minute sample and was rejected by the fitting process when fitting the 5-minute and seeded samples. This observation matches what has previously been seen in SE characterisation of early-stage diamond film growth on silicon [13, 131]. Application of the SE model to a sample grown for 20 minutes resulted in an MSE in excess of 100 as a result of depolarisation due to increased surface roughness caused by crystallite overgrowth.

6.3.4 Application to *In-Situ* Spectra

The model was modified slightly to account for the changes introduced by the application to *in-situ* data. In-plane window effects from the fused silica windows were accounted by the CompleteEASE software using spectra of a reference sample as detailed in [156]. A second consideration was the impact of the elevated temperature on the optical constants of the silicon substrate. The optical constants used were replaced with those of silicon from a temperature-dependent library within the CompleteEASE software, with the temperature set to the substrate temperature of 730 °C measured using a dual-wavelength pyrometer. Whilst the refractive index of the modelled AlN layer did vary slightly when the Cauchy parameters were allowed to vary when fitting the *in-situ* data, this did not impact the trends seen in the modelled diamond layer thickness and composition. As a result, the Cauchy parameters were not allowed to vary in the *in-situ* model to reduce the impact of parameter correlation on the derived parameters. Such parameter correlation can occur during the data fitting process in cases where changes in multiple different parameters exhibit the same spectral signature, resulting in multiple combinations of parameter values producing the same quality of fit. This means that there will be no unique determination of optimal parameter values [181]. It was unnecessary to vary the optical constants of the diamond film components as the refractive index of diamond films does not vary substantially with temperature [157].

Figure 6.8 shows *in-situ* SE-derived parameters for the first 30 minutes of the 90-minute growth duration sample, along with *ex-situ* measurements taken from samples of varying growth duration. In the first 10 minutes of growth, a decrease in sp_2 content was seen, which is typical of the preferential etching of non-diamond carbon observed in hydrogen-containing plasmas [159]. Simultaneously, a decrease in void content was observed due to the lateral and vertical Volmer-Weber growth of diamond nuclei. A sharp increase in the sp^2 content is seen from approximately 13 minutes onwards, due to the trapping of non-diamond carbon within grain boundaries in the process of coalescence of individual crystallites into a single film [2, 13, 131]. A peak in surface roughness was seen just before coalescence, as individual islands reach their maximum size whilst still remaining isolated [131]. Following coalescence, growth proceeds by the van der Drift mechanism [131], with competitive overgrowth of crystallites resulting in increased surface roughness with growth duration [67]. Accordingly, a steep increase in surface roughness is seen after coalescence. This increasing surface roughness does result in increases in MSE further into the growth process due to depolarisation, and as such SE characterisation is limited to the early stages of growth.

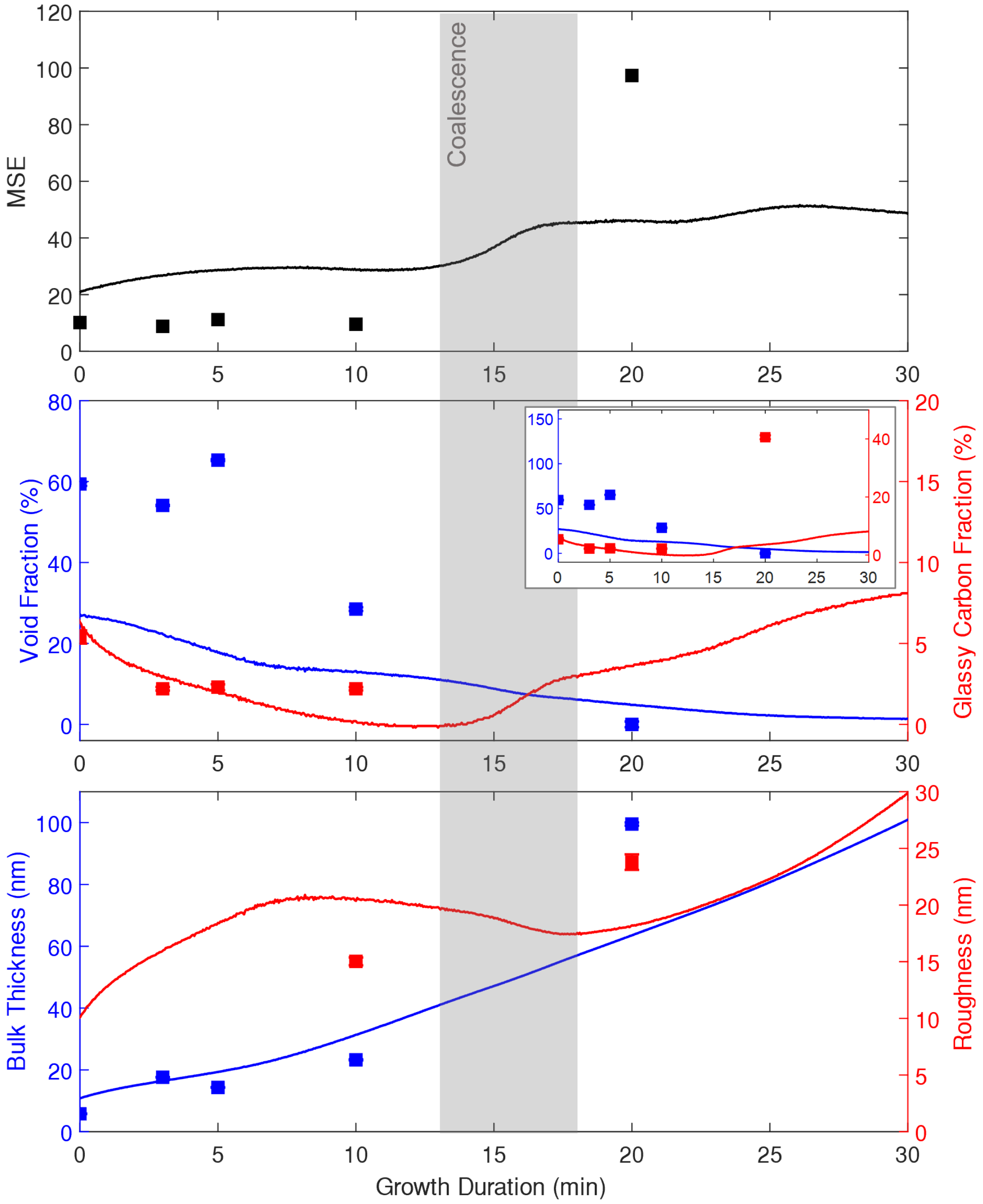

Figure 6.8: *In situ* and *ex situ* SE model parameters. Top: MSE. Middle: SE-derived void and glassy carbon fractions. Inset: Zoomed out view. Bottom: SE-derived bulk thickness and roughness layer thickness. All ex-situ parameters are plotted as individual points.

As seen previously in SE of diamond film grown on silicon, models of *ex-situ* spectra suggested a greater void fraction than *in-situ* spectra, although the same trend of decreasing void fraction with growth duration is seen. This is attributed to the cooling of samples in a purely hydrogen plasma, which can result in etching of sp^2 material [159]. Whilst results from fitting *ex-situ* spectra of the 20-minute growth duration sample are included for completeness, the very high MSE between measured and modelled spectra means that it is likely that parameters derived from the SEdo not accurately reflect the true nature of this specific sample.

6.3.5 Raman Spectroscopy

Figure 6.9 shows Raman spectra for samples of varying growth duration, normalised to the second order silicon Raman peak at 950 cm^{-1}. The limited diamond film and AlN layer thicknesses means that the most prominent peaks are from the Si substrate. These are the first and second-order Si Raman peaks, which are seen at 520 and 980 cm^{-1} respectively [161]. Minor peaks at 620 and 644 cm^{-1} are caused by local vibrational modes of boron atoms within the heavily doped Si substrate. For growth durations below 10 minutes, the the diamond Raman peak at 1332.5 cm^{-1} [9] is not observed, due to the limited bulk thickness and diamond fraction of these samples. At 10 minutes, SE measurements suggest a greater bulk diamond fraction and thickness, which is matched by the appearance of the diamond Raman peak. This peak exhibits broadening as is typical for samples with small crystallite size [9, 138]. Appearing for the first time in this sample are peaks at 1140 and 1450 cm^{-1}, assigned to *trans*-polyacetylene [8], as well as the G-band at around 1550 cm^{-1} caused by in-plane stretching of pairs of sp^2 sites [9]. Whilst the G peak, caused by bond stretching of pairs of sp^2 atoms in rings and chains, is typically visible at around 1560 cm^{-1} [96], it is obscured by the G-band in this case.

At 20 minutes, a significant increase in the intensity of the diamond peak is seen due to the increase in both thickness and diamond content by this point. Similar increases in the intensity of the G-band and *trans*-polyacetylene peaks were seen, with the intensities of those also increasing relative to that of the diamond peak. As *trans*-polyacetylene is found within the grain boundaries [8], its

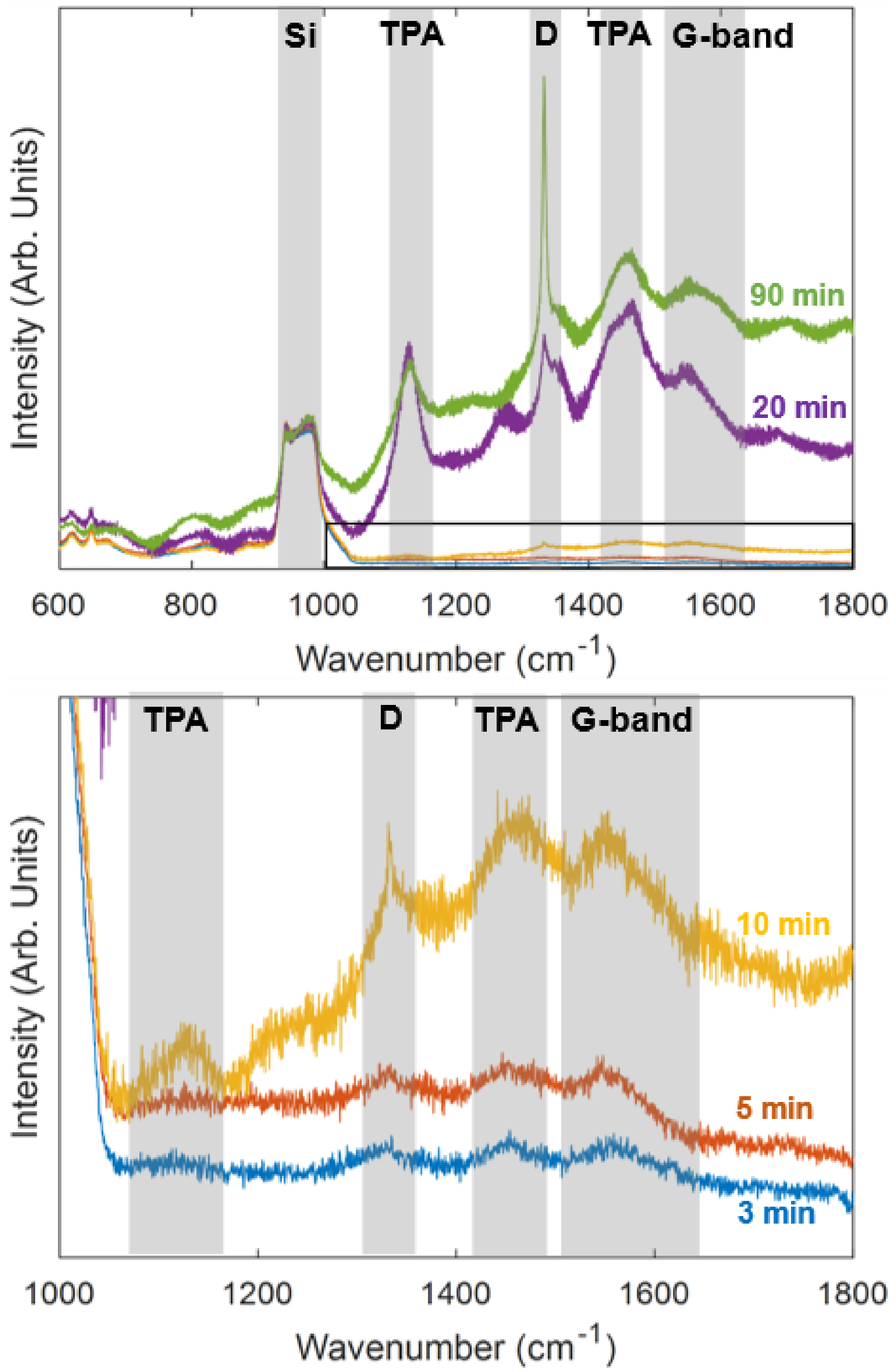

Figure 6.9: Top: *Ex-situ* Raman spectra of samples with varying growth duration, normalised to the second-order silicon Raman peak. Bottom: Magnified view of the region of the region of the spectrum indicated above.

appearance is indicative of the formation of these during the coalescence of crystallites into a single film, suggesting that this occurs prior to 20 minutes. This is consistent with the *in-situ* SE model suggesting that coalescence occurs between 10 and 20 minutes. Seen for the first time in the 20 minute sample is the D peak at 1350 cm^{-1}, caused by the breathing mode of graphitic rings [96].

The intensity of the diamond peak is greater in the 90-minute growth sample due to its increased thickness. Additionally, the *trans*-polyacetylene peaks and G-band are lower in intensity relative to the diamond peak, indicating a decrease in sp^2 content relative to the 20-minute sample because of the larger crystallite size of the thicker film. The sharp diamond peak seen in this sample is indicative of a high-quality polycrystalline diamond film.

6.3.6 Atomic Force Microscopy

Figure 6.10 shows AFM images of samples with increasing growth durations, with Figure 6.11 showing the AFM-measured RMS roughness of the same samples. A gradual increase in RMS roughness and crystallite size is seen up to 10 minutes. Between 10 and 20 minutes, a significant increase in crystallite size and roughness is observed due to coalescence and the switch to van der Drift type growth, another indication that coalescence occurs between 10 and 20 minutes as suggested by the *in-situ* SE model. Crystallite size continues to increase with growth duration due to the overgrowth of crystallites, with the greatest roughness and crystallite size seen in the 90 minute growth duration sample. Figure 6.12 shows a zoomed-out image of the 90 minute sample.

6.4 Conclusion

The early stages of polycrystalline diamond growth on aluminium nitride were investigated using SE. *Ex-situ* spectra were used to develop an optical model for film characterisation, with an iterative fitting process allowing parameters to vary to minimise MSE between measured and modelled spectra. This model was then applied to *in-situ* data and compared to AFM images and Raman spectra from

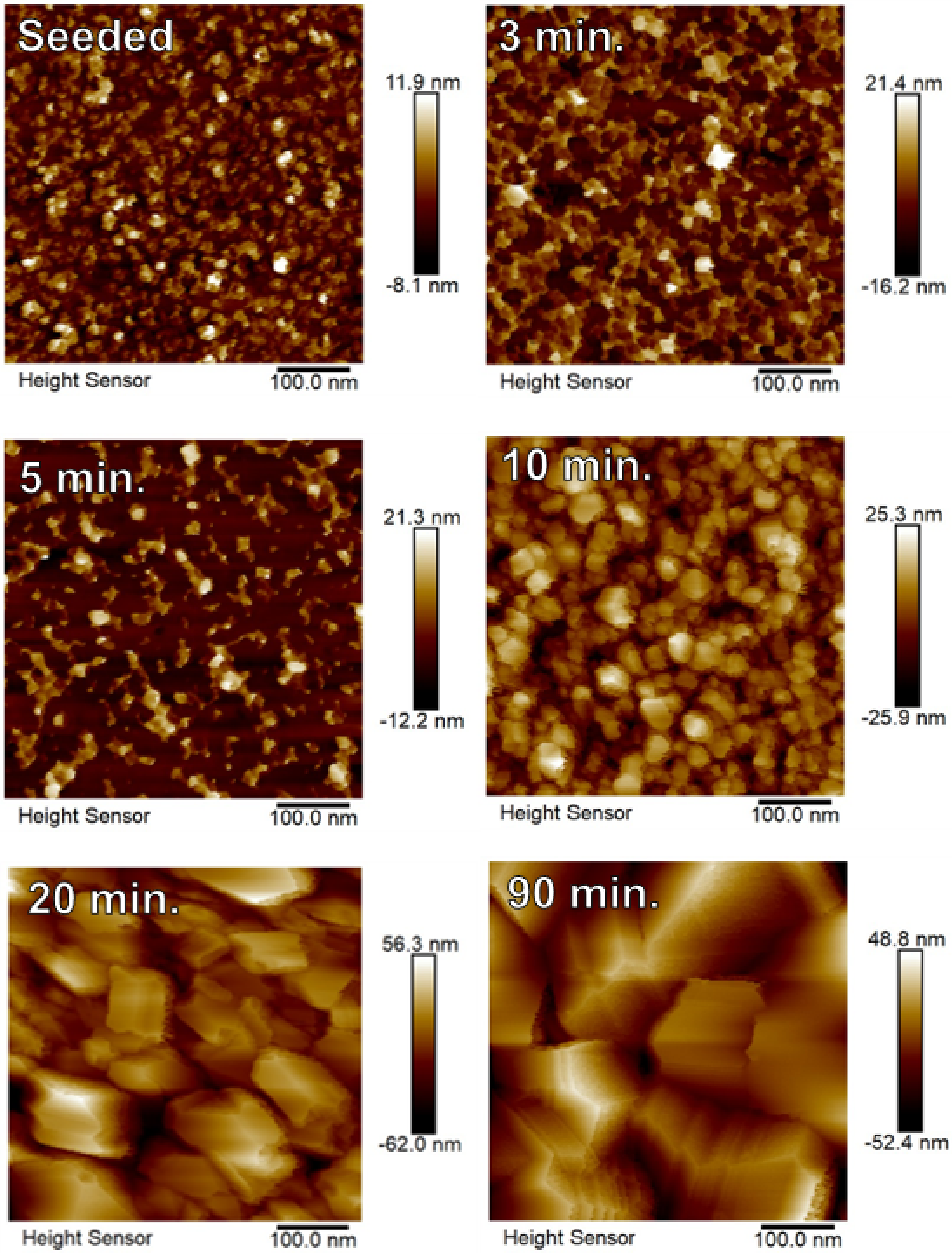

Figure 6.10: AFM images of samples grown for various durations

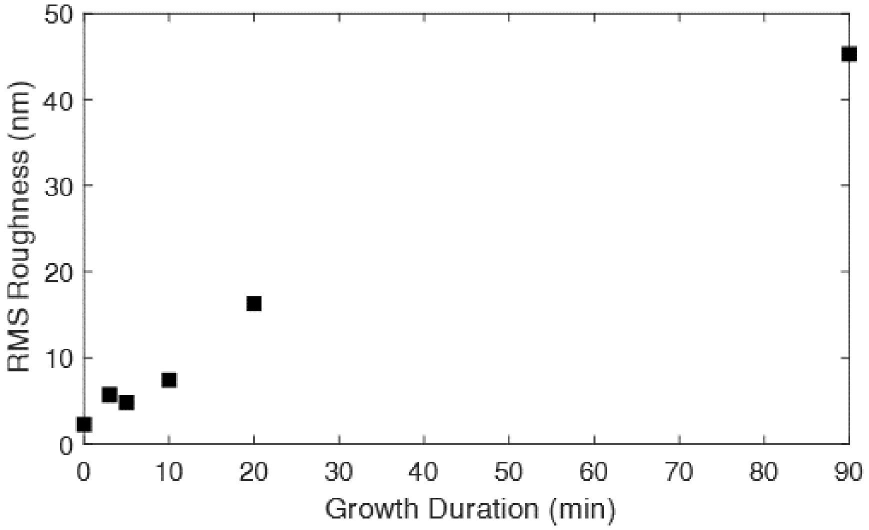

Figure 6.11: AFM-measured RMS roughness of samples with varying growth duration.

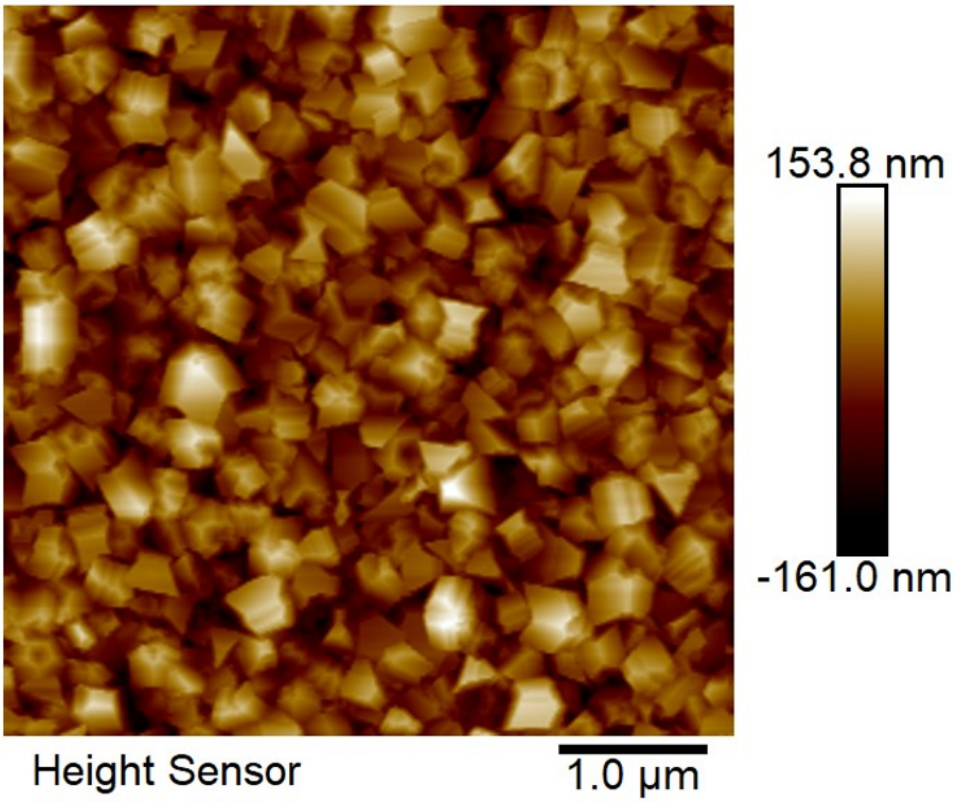

Figure 6.12: Zoomed-out AFM image of the 90 minute sample

samples of varying growth duration. An initial reduction in bulk layer void content was seen, followed by an increase in sp^2 content indicative of the formation of grain boundaries during coalescence of individual islands into a single film. The increase in sp^2 was also seen in Raman spectra, with peaks caused by *trans*-polyacetylene, found in grain boundaries, increasing in intensity following the point of coalescence indicated by the *in-situ* SE model. AFM images showed RMS roughness and crystallite size increasing with growth duration.

Application of SE to diamond growth on AlN in this way provides a highly useful ability to characterise the critical early stages of diamond growth, with sub-nanometre resolution and an ability to determine the composition and morphology of the film. The model developed in this chapter allows for further understanding and optimisation of these early stages, which is important to reduce the thermal barrier resistance associated with the disordered transition region formed during this period, improving the effectiveness of diamond thermal management layers. In addition to this, by demonstrating the adaptation of an existing SE model of diamond growth on silicon to growth on aluminium nitride, this work presents a clear blueprint for developing *in-situ* monitoring of diamond growth on new substrates.

Chapter 7

Conclusions and Future Work

This thesis focuses on *in-situ* monitoring of diamond growth by MPECVD, attempting to provide diagnostic measurements to optimise film growth. Firstly, the uniformity of substrate temperature under growth conditions is investigated. Substrate temperature during growth has a significant impact on film properties, with higher temperatures result in faster growth rates and lower levels of sp^2 content. Non-uniform substrate temperature will result in the growth of an inhomogeneous film. Chapter 4 details the employment of a mirror galvanometer system coupled with a dual-wavelength pyrometer to produce temperature maps of substrate holders under growth conditions. Three differently-shaped substrate holders were mapped, with increases in substrate temperature seen towards the centre of the holders, as well as around the edge. These showed good agreement with FEM simulations, which predicted a higher plasma density in these regions, as well as observations of the formation of a secondary plasma around the edge of the holder.

The temperature mapping technique was further validated by growing diamond films at the same power and pressure that temperature maps were taken, with the properties of these films mapped using *ex-situ* Raman spectroscopy and SE. A greater SE-measured bulk thickness and bulk sp^3 fraction were seen in the higher-temperature central region of the film. A greater intensity and lower FWHM of the first-order diamond Raman peak was also seen in this region, indicative of a thicker and higher-quality film.

With the temperature mapping system demonstrated and measurements validated, the next stage will be to utilise it, coupled with FEM simulations, to optimise substrate holder design. The impact of varying substrate holder design can be quickly evaluated, with easy experimental validation of FEM simulations of plasma density and substrate temperature. In addition, for existing holder designs the system can be utilised to easily determine the optimal combination of microwave power and chamber pressure to produce a uniform substrate temperature, and therefore a uniform diamond film.

Whilst substrate temperature has a significant impact on diamond film quality, it is not the only factor impacting this. Film quality is heavily dependent on seeding, nucleation, and the early stages of growth. With the ability to determine film composition and thickness with sub-nanometre resolution SE is ideally suited for*in-situ* monitoring early-stage diamond film growth. Chapter 5 describes the use of *SE* for this purpose. First, a model is developed using *ex-situ* spectra, consisting of an EMA mixing optical constants of diamond, void, and glassy carbon to approximate the different components of the diamond film atop a silicon substrate, with a third layer made up of 50% bulk and 50% void to account for surface roughness. The model was modified to account for window effects and the elevated substrate temperature and applied to *in-situ* spectra. After a short duration, a parabolic decrease in bulk void content was seen due to lateral growth of the individual crystallites. The coalescence of these into a single film was identified by a peak in glassy carbon content due to the trapping of sp^2 material in grain boundaries, with a peak in surface roughness just before coalescence as crystallites reach the maximum size whilst still remaining separate. The model was validated using *ex-situ* AFM and Raman spectra of samples grown for varying duration, with the same trends observed in diamond content, sp^2 content, and surface roughness.

With a model for characterisation of the diamond film developed and validated, it was then used to investigate the impact of varying the methane concentration during growth. It was found that increasing the methane concentration from 3% to 5% caused an increase in growth rate, with earlier coalescence and a greater peak in glassy carbon content at the point of coalescence. Decreasing the methane concentration to 1% resulted in much slower growth, with coalescence significantly delayed. Whilst methane concentration is an important growth parameter as it impacts the level of renucleation during growth, it is not the only important parameter. As demonstrated in Chapter 4, the substrate temperature during growth has a significant impact on the growth rate and properties of the film. Further work therefore could utilise the model developed here to investigate the impact of varying substrate temperature on the point of coalescence and peak sp^2 content.

Chapter 6 builds on the previous chapter by applying SE to the growth of diamond on AlN. Whilst diamond growth on silicon is routine and well understood, growth on AlN can be challenging and is less understood. In thermal management applications, the disordered interfacial region formed in the early stages of film growth is associated with a thermal barrier resistance and is therefore a significant limiting factor. As in Chapter 5, *ex-situ* spectra are used to develop an optical model for a diamond film grown on AlN. The diamond film was again modelled using an EMA with diamond, void and glassy carbon, with the AlN layer modelled using a three-term Cauchy dispersion. The point of coalescence was observed through a reduction in void content followed by a peak in glassy carbon content, with the *in-situ* model validated using *ex-situ* Raman spectra and AFM.

This chapter successfully demonstrated *in-situ* SE characterisation of diamond film growth on AlN for the first time. Given that growth was monitored for a single set of substrate temperature and methane concentration parameters, the clear next step is to employ the SE model to investigate the impact of varying these on the initial stages of the film, identifying the optimum growth conditions for a high quality interface and low thermal resistance. By demonstrating that SE can be applied to diamond growth on materials other than silicon, this work opens the door to characterisation of early-stage diamond growth on alternative heterogeneous materials such as GaN.

This thesis has attempted to develop methods for *in-situ* monitoring of MPECVD diamond growth. It is hoped that the techniques demonstrated here provide the reader with a toolset to optimise growth parameters for a greater diamond film uniformity and quality.

Bibliography

[1]T. G. McCauley, D. M. Gruen, and A. R. Krauss, “Temperature dependence of the growth rate for nanocrystalline diamond films deposited from an Ar/CH_4 microwave plasma”, Applied Physics Letters **73**, 1646–1648 (1998).

[2]B. Hong, J. Lee, R. Collins, Y. Kuang, W. Drawl, R. Messier, T. Tsong, and Y. Strausser, “Effects of processing conditions on the growth of nanocrystalline diamond thin films: real time spectroscopic ellipsometry studies”, Diamond and Related Materials **6**, 55–80 (1997).

[3]J. A. Cuenca, S. Mandal, E. L. H. Thomas, and O. A. Williams, “Microwave plasma modelling in clamshell chemical vapour deposition diamond reactors”, Diamond and Related Materials **124**, 108917 (2022).

[4]W. G. S. Leigh, J. A. Cuenca, E. L. H. Thomas, S. Mandal, and O. A. Williams, “Mapping the effect of substrate temperature inhomogeneity during microwave plasma-enhanced chemical vapour deposition nanocrystalline diamond growth”, Carbon **201**, 328–337 (2023).

[5]J. Philip, P. Hess, T. Feygelson, J. E. Butler, S. Chattopadhyay, K. H. Chen, and L. C. Chen, “Elastic, mechanical, and thermal properties of nanocrystalline diamond films”, Journal of Applied Physics **93**, 2164–2171 (2003).

[6]K. A. Snail and C. M. Marks, “*In situ* diamond growth rate measurement using emission interferometry”, Applied Physics Letters **60**, 3135–3137 (1992).

[7]C. D. Zuiker, D. M. Gruen, and A. R. Krauss, “*In situ* laser reflectance interferometry measurement of diamond film growth”, Journal of Applied Physics **79**, 3541–3547 (1996).

[8]A. C. Ferrari and J. Robertson, “Origin of the 1150-cm^{-1} Raman mode in nanocrystalline diamond”, Physical Review B **63**, 121405 (2001).

[9]A. C. Ferrari, J. Robertson, A. C. Ferrari, and J. Robertson, “Raman spectroscopy of amorphous, nanostructured, diamond–like carbon, and nanodiamond”, Philosophical Transactions of the Royal Society of London. Series A: Mathematical, Physical and Engineering Sciences **362**, 2477–2512 (2004).

[10]Y. Cong, R. W. Collins, G. F. Epps, and H. Windischmann, “Spectroellipsometry characterization of optical quality vapor-deposited diamond thin films”, Applied Physics Letters **58**, 819–821 (1991).

[11]B. Hong, M. Wakagi, R. Collins, I. An, N. Engdahl, W. Drawl, and R. Messier, “Real-time spectroscopic ellipsometry studies of diamond film growth by microwave plasma-enhanced chemical vapour deposition”, Diamond and Related Materials **3**, 431–437 (1994).

[12]G. Koster and G. Rijnders, eds., *In-situ characterization of thin film growth*, Woodhead Publishing in materials (Woodhead Publishing, Cambridge ; Philadelphia, PA, 2011).

[13]W. G. S. Leigh, E. L. H. Thomas, J. A. Cuenca, S. Mandal, and O. A. Williams, “*In-situ* monitoring of microwave plasma-enhanced chemical vapour deposition diamond growth on silicon using spectroscopic ellipsometry”, Carbon **202**, 204–212 (2023).

[14]J. W. Pomeroy, M. Bernardoni, D. C. Dumka, D. M. Fanning, and M. Kuball, “Low thermal resistance GaN-on-diamond transistors characterized by three-dimensional Raman thermography mapping”, Applied Physics Letters **104**, 083513 (2014).

[15]H. Sun, R. B. Simon, J. W. Pomeroy, D. Francis, F. Faili, D. J. Twitchen, and M. Kuball, “Reducing GaN-on-diamond interfacial thermal resistance for high power transistor applications”, Applied Physics Letters **106**, 111906 (2015).

[16]S. Mandal, E. L. H. Thomas, C. Middleton, L. Gines, J. T. Griffiths, M. J. Kappers, R. A. Oliver, D. J. Wallis, L. E. Goff, S. A. Lynch, M. Kuball, and O. A. Williams, “Surface Zeta Potential and Diamond Seeding on Gallium Nitride Films”, ACS Omega **2**, 7275–7280 (2017).

[17]S. Mandal, C. Yuan, F. Massabuau, J. W. Pomeroy, J. Cuenca, H. Bland, E. Thomas, D. Wallis, T. Batten, D. Morgan, R. Oliver, M. Kuball, and O. A. Williams, “Thick, Adherent Diamond Films on AlN with Low Thermal Barrier Resistance”, ACS Applied Materials & Interfaces **11**, 40826–40834 (2019).

[18]M. D. Smith, J. A. Cuenca, D. E. Field, Y.-c. Fu, C. Yuan, F. Massabuau, S. Mandal, J. W. Pomeroy, R. A. Oliver, M. J. Uren, K. Elgaid, O. A. Williams, I. Thayne, and M. Kuball, “GaN-on-diamond technology platform: Bonding-free membrane manufacturing process”, AIP Advances **10**, 035306 (2020).

[19]H. O. Pierson, *Handbook of carbon, graphite, diamond, and fullerenes: properties, processing, and applications* (Noyes Publications, Park Ridge, N.J., U.S.A, 1993).

[20]A. G. Guy and J. J. Hren, *Elements of physical metallurgy*, 3d ed, Addison-Wesley series in metallurgy and materials (Addison-Wesley, Reading, Mass, 1974).

[21]K. Kobashi, *Diamond films: chemical vapor deposition for oriented and heteroepitaxial growth*, 1st ed (London Elsevier, Amsterdam, 2005).

[22]L. S. Pan and D. R. Kania, eds., *Diamond: electronic properties and applications*, The Kluwer international series in engineering and computer science (Kluwer Academic, Boston, 1995).

[23]A. M. Zaitsev, *Optical Properties of Diamond: A Data Handbook* (Springer Science & Business Media, June 2001).

[24]A. M. Schrand, S. A. C. Hens, and O. A. Shenderova, “Nanodiamond Particles: Properties and Perspectives for Bioapplications”, Critical Reviews in Solid State and Materials Sciences **34**, 18–74 (2009).

[25]C. J. H. Wort and R. S. Balmer, “Diamond as an electronic material”, Materials Today **11**, 22–28 (2008).

[26]J. Isberg, J. Hammersberg, E. Johansson, T. Wikström, D. Twitchen, A. Whitehead, S. Coe, and G. Scarsbrook, “High carrier mobility in single-crystal plasma-deposited diamond”, Science **297**, 1670–1672 (2002).

[27]M. Yahiaoui, J. .-. Paris, K. Delbé, J. Denape, L. Gerbaud, and A. Dourfaye, "Independent analyses of cutting and friction forces applied on a single polycrystalline diamond compact cutter", International Journal of Rock Mechanics and Mining Sciences **85**, 20–26 (2016).

[28]J. W. Pomeroy, R. B. Simon, H. Sun, D. Francis, F. Faili, D. J. Twitchen, and M. Kuball, "Contactless Thermal Boundary Resistance Measurement of GaN-on-Diamond Wafers", IEEE Electron Device Letters **35**, 1007–1009 (2014).

[29]J. V. Macpherson, "A practical guide to using boron doped diamond in electrochemical research", Physical Chemistry Chemical Physics **17**, 2935–2949 (2015).

[30]H. A. Bland, I. A. Centeleghe, S. Mandal, E. L. H. Thomas, J.-Y. Maillard, and O. A. Williams, "Electropositive Nanodiamond-Coated Quartz Microfiber Membranes for Virus and Dye Filtration", ACS Applied Nano Materials **4**, 3252–3261 (2021).

[31]S. Mandal, G. Shaw, and O. A. Williams, "Comparison of nanodiamond coated quartz filter with commercial electropositive filters: Zeta potential and dye retention study", Carbon **199**, 439–443 (2022).

[32]G. Aiello, T. Scherer, K. Avramidis, N. Casal, T. Franke, M. Gagliardi, G. Gantenbein, M. Henderson, J. Jelonnek, A. Meier, G. Saibene, S. Schreck, D. Strauss, M. Thumm, M. Q. Tran, C. Wild, and E. Woerner, "Diamond Window Technology for Electron Cyclotron Heating and Current Drive: State of the Art", Fusion Science and Technology **75**, 719–729 (2019).

[33]E. Pace and A. De Sio, "Diamond detectors for space applications", Nuclear Instruments and Methods in Physics Research Section A: Accelerators, Spectrometers, Detectors and Associated Equipment, Proceedings of the 4th International Conference on Radiation Effects on Semiconductor Materials, Detectors and Devices **514**, 93–99 (2003).

[34]A. V. Sumant, O. Auciello, M. Liao, and O. A. Williams, "MEMS/NEMS based on mono-, nano-, and ultrananocrystalline diamond films", MRS Bulletin **39**, 511–516 (2014).

[35]H. Davy, "XXVII. Some experiments on the combustion of the diamond and other carbonaceous substances", Philosophical Transactions of the Royal Society of London **104**, 557–570 (1814).

[36]P. A. Rock, *Chemical Thermodynamics* (University Science Books,U.S., Nov. 1983).

[37]F. P. Bundy, H. P. Bovenkerk, H. M. Strong, and R. H. Wentorf, "Diamond-Graphite Equilibrium Line from Growth and Graphitization of Diamond", The Journal of Chemical Physics **35**, 383–391 (1961).

[38]D. M. Adams, *Inorganic Solids: Introduction to Concepts in Solid-state Structural Chemistry*, First Edition (Wiley–Blackwell, London, New York, Jan. 1974).

[39]F. P. Bundy, H. T. Hall, H. M. Strong, and R. H. Wentorfjun., "Man-Made Diamonds", Nature **176**, 51–55 (1955).

[40]H. Liander and E. Lundblad, "Artificial diamonds", ASEA J **28**, 97 (1955).

[41]S. M. Stishov, "Mysteries of diamond synthesis at the Institute of High Pressure Physics of the Academy of Sciences of the Soviet Union", Physics-Uspekhi **62**, 704 (2019).

[42]P. W. May, "Diamond thin films: a 21st-century material", en, Philosophical Transactions of the Royal Society of London. Series A: Mathematical, Physical and Engineering Sciences **358**, 473–495 (2000).

[43]V. V. Danilenko, "On the history of the discovery of nanodiamond synthesis", Physics of the Solid State **46**, 595–599 (2004).

[44]A. Krüger, F. Kataoka, M. Ozawa, T. Fujino, Y. Suzuki, A. E. Aleksenskii, A. Y. Vul', and E. Ōsawa, "Unusually tight aggregation in detonation nanodiamond: Identification and disintegration", Carbon **43**, 1722–1730 (2005).

[45]W. G. Eversole, "Synthesis of diamond", US3030187A (Apr. 1962).

[46]J. C. Angus, "Diamond synthesis by chemical vapor deposition: The early years", Diamond and Related Materials **49**, 77–86 (2014).

[47]J. C. Angus, H. A. Will, and W. S. Stanko, "Growth of Diamond Seed Crystals by Vapor Deposition", Journal of Applied Physics **39**, 2915–2922 (1968).

[48]B. Spitsyn, L. Bouilov, and B. Derjaguin, "Vapor growth of diamond on diamond and other surfaces", Journal of Crystal Growth **52**, 219–226 (1981).

[49]S. Matsumoto, Y. Sato, M. Kamo, and N. Setaka, “Vapor Deposition of Diamond Particles from Methane”, Japanese Journal of Applied Physics **21**, L183 (1982).

[50]M. Kamo, Y. Sato, S. Matsumoto, and N. Setaka, “Diamond synthesis from gas phase in microwave plasma”, Journal of Crystal Growth **62**, 642–644 (1983).

[51]O. A. Williams, “Nanocrystalline diamond”, Diamond and Related Materials **20**, 621–640 (2011).

[52]M. A. Prelas, G. Popovici, and L. K. Bigelow, eds., *Handbook of industrial diamonds and diamond films* (Marcel Dekker, New York, 1998).

[53]K. Ohtsuka, K. Suzuki, A. Sawabe, and T. Inuzuka, “Epitaxial growth of diamond on iridium”, Japanese Journal of Applied Physics, Part 2: Letters **35**, L1072–L1074 (1996).

[54]W. S. Yang and J. H. Je, “Effects of secondary pretreatments of substrate on the nucleation of diamond film”, Journal of Materials Research **11**, 1787–1794 (1996).

[55]X. Jiang, K. Schiffmann, and C.-P. Klages, “Nucleation and initial growth phase of diamond thin films on (100) silicon”, Physical Review B **50**, 8402–8410 (1994).

[56]P. Ascarelli and S. Fontana, “Dissimilar grit-size dependence of the diamond nucleation density on substrate surface pretreatments”, Applied Surface Science **64**, 307–311 (1993).

[57]S. Iijima, Y. Aikawa, and K. Baba, “Early formation of chemical vapor deposition diamond films”, Applied Physics Letters **57**, 2646–2648 (1990).

[58]B. R. Stoner, G.-H. M. Ma, S. D. Wolter, and J. T. Glass, “Characterization of bias-enhanced nucleation of diamond on silicon by invacuo surface analysis and transmission electron microscopy”, Physical Review B **45**, 11067–11084 (1992).

[59]J. Robertson, “Mechanism of bias-enhanced nucleation and heteroepitaxy of diamond on Si”, Diamond and Related Materials, Diamond Films ’94 **4**, 549–552 (1995).

[60]J.-C. Arnault, S. Saada, S. Delclos, L. Rocha, L. Intiso, R. Polini, A. Hoffman, S. Michaelson, and P. Bergonzo, “Surface science contribution to the BEN control on Si(100) and 3C-SiC(100): Towards ultrathin nanocrystalline diamond films”, Chemical Vapor Deposition **14**, 187–195 (2008).

[61]O. A. Williams, O. Douhéret, M. Daenen, K. Haenen, E. Ōsawa, and M. Takahashi, "Enhanced diamond nucleation on monodispersed nanocrystalline diamond", Chemical Physics Letters **445**, 255–258 (2007).

[62]O. Williams, J. Hees, C. Dieker, W. Jäger, L. Kirste, and C. Nebel, "Size-dependent reactivity of diamond nanoparticles", ACS Nano **4**, 4824–4830 (2010).

[63]S. Osswald, G. Yushin, V. Mochalin, S. Kucheyev, and Y. Gogotsi, "Control of sp2/sp3 carbon ratio and surface chemistry of nanodiamond powders by selective oxidation in air", Journal of the American Chemical Society **128**, 11635–11642 (2006).

[64]L. Bousse, S. Mostarshed, B. Van Der Shoot, N. F. de Rooij, P. Gimmel, and W. Göpel, "Zeta potential measurements of Ta2O5 and SiO2 thin films", Journal of Colloid and Interface Science **147**, 22–32 (1991).

[65]S. Michaelson, O. Ternyak, A. Hoffman, and Y. Lifshitz, "Correlation between diamond grain size and hydrogen retention in diamond films studied by scanning electron microscopy and secondary ion mass spectroscopy", Applied Physics Letters **90**, 031914 (2007).

[66]Z. Cao, *Thin film growth: physics, materials science and applications*, Woodhead publishing in materials (Woodhead publ, Oxford (GB), 2011).

[67]A. van der Drift, "Evolutionary Selection, a Principle Governing Growth Orientation in Vapour-Deposited Layers", Philips Research Report **22**, 267–268 (1967).

[68]C. Wild, N. Herres, and P. Koidl, "Texture formation in polycrystalline diamond films", Journal of Applied Physics **68**, 973–978 (1990).

[69]O. A. Williams, M. Nesladek, M. Daenen, S. Michaelson, A. Hoffman, E. Osawa, K. Haenen, and R. B. Jackman, "Growth, electronic properties and applications of nanodiamond", Diamond and Related Materials, Proceedings of Diamond 2007, the 18th European Conference on Diamond, Diamond-Like Materials, Carbon Nanotubes, Nitrides and Silicon Carbide **17**, 1080–1088 (2008).

[70]P. R. N. Childs, *Practical temperature measurement* (Butterworth-Heinemann, Oxford, 2001).

[71] S. Blundell and K. M. Blundell, *Concepts in thermal physics* (Oxford University Press, Oxford ; New York, 2006).

[72] J. Wedgewood, “XIX. An attempt to make a thermometer for measuring the higher degrees of heat, from a red heat up to the strongest that vessels made of clay can support”, Philosophical Transactions of the Royal Society of London **72**, 305–326 (1782).

[73] M. Planck, *The theory of heat radiation* (P. Blakiston’s Son & Co., Philadelphia, 1914).

[74] W. Wien, “XXX. *On the division of energy in the emission-spectrum of a black body*”, The London, Edinburgh, and Dublin Philosophical Magazine and Journal of Science **43**, 214–220 (1897).

[75] L. Michalski and L. Michalski, eds., *Temperature measurement*, 2nd ed (J. Wiley, Chichester ; New York, 2001).

[76] T. J. Quinn and T. J. Quinn, *Temperature.* (Elsevier Science, Kent, 2014).

[77] J. R. Simonson, *Engineering heat transfer*, repr. of the 1st ed. 1975 (MacMillan, London, 1983).

[78] Y. Zhang, *Theory and calculation of heat transfer in furnaces* (Elsevier, Boston, MA, 2016).

[79] E. F. Morse, “Method of gaging temperatures of heated substances”, US696878A (Apr. 1902).

[80] E. F. Morse, “Apparatus for gaging temperatures of heated substances”, US696916A (Apr. 1902).

[81] L. Holborn and F. Kurlbaum, “Über ein optisches Pyrometer”, Annalen der Physik **315**, 225–241 (1903).

[82] S. A. Treese, *History and Measurement of the Base and Derived Units* (Springer International Publishing, Cham, Switzerland, 2018).

[83] R. F. Speyer, *Thermal analysis of materials*, Materials engineering 5 (Marcel Dekker, New York, 1994).

[84] R. E. Bentley, ed., *Handbook of temperature measurement* (Springer, Singapore ; New York, 1998).

[85]H. Fujiwara, *Spectroscopic ellipsometry: principles and applications* (John Wiley & Sons, Chichester, England ; Hoboken, NJ, 2007).

[86]S.-i. Ohkoshi, T. Nuida, T. Matsuda, H. Tokoro, and K. Hashimoto, “The dielectric constant in a thermal phase transition magnetic material composed of rubidium manganese hexacyanoferrate observed by spectroscopic ellipsometry”, Journal of Materials Chemistry **15**, 3291–3295 (2005).

[87]H. G. Tompkins, *A User’s Guide to Ellipsometry* (Elsevier Science, Saint Louis, 2014).

[88]S. Saada, S. Pochet, L. Rocha, J. C. Arnault, and P. Bergonzo, “Real time investigation of diamond nucleation by laser scattering”, Diamond and Related Materials, Proceedings of Diamond 2008, the 19th European Conference on Diamond, Diamond-Like Materials, Carbon Nanotubes, Nitrides and Silicon Carbide **18**, 707–712 (2009).

[89]F. Bénédic, M. Belmahi, T. Easwarakhanthan, and P. Alnot, “In situ optical characterization during MPACVD diamond film growth on silicon substrates using a bichromatic infrared pyrometer under oblique incidence”, Journal of Physics D: Applied Physics **34**, 1048–1058 (2001).

[90]C. R. Brundle, C. A. Evans, and S. Wilson, eds., *Encyclopedia of materials characterization: surfaces, interfaces, thin films*, Materials characterization series (Butterworth-Heinemann ; Manning, Boston : Greenwich, CT, 1992).

[91]J. W. Strutt, “On the light from the sky, its polarization and colour”, The London, Edinburgh, and Dublin Philosophical Magazine and Journal of Science **41**, 107–120 (1871).

[92]G. G. Stokes, “On the change of refrangibility of light”, Philosophical Transactions of the Royal Society of London **142**, 463–562 (1852).

[93]P. Vandenabeele, *Practical Raman Spectroscopy – An Introduction*, 1st ed. (Wiley, July 2013).

[94]C. V. Raman and K. S. Krishnan, “A New Type of Secondary Radiation”, Nature **121**, 501–502 (1928).

[95]S. Leeds, T. Davis, P. May, C. Pickard, and M. Ashfold, “Use of different excitation wavelengths for the analysis of CVD diamond by laser Raman spectroscopy”, Diamond and Related Materials **7**, 233–237 (1998).

[96]A. C. Ferrari, “Raman spectroscopy of graphene and graphite: Disorder, electron–phonon coupling, doping and nonadiabatic effects”, Solid State Communications, Exploring graphene **143**, 47–57 (2007).

[97]G. Binnig, C. F. Quate, and C. Gerber, “Atomic Force Microscope”, Physical Review Letters **56**, 930–933 (1986).

[98]K. Morrison, *Characterisation Methods in Solid State and Materials Science* (IOP Publishing, Oct. 2019).

[99]Y. Seo and W. Jhe, “Atomic force microscopy and spectroscopy”, Reports on Progress in Physics **71**, 016101 (2007).

[100]S. Amelinckx, *Handbook of microscopy: applications in materials science, solid-state physics, and chemistry. 2, Methods II*, Handbook of microscopy : applications in materials science, solid-state physics, and chemistry (VCH, Weinheim, 1997).

[101]W. Bowen, *Atomic Force Microscopy in Process Engineering: An Introduction to AFM for Improved Processes and Products* (Butterworth-Heinemann, Amsterdam Boston Paris etc., Jan. 2009).

[102]S. N. Magonov and M.-H. Whangbo, *Surface Analysis with STM and AFM: Experimental and Theoretical Aspects of Image Analysis*, 1st ed. (Wiley, Dec. 1995).

[103]V. V. Tsukruk and S. Singamaneni, *Scanning Probe Microscopy of Soft Matter: Fundamentals and Practices*, 1st ed. (Wiley, Nov. 2011).

[104]D. L. Logan, *A First Course in the Finite Element Method*, 5th Revised ed. edition (CL Engineering, Stamford, CT, Apr. 2010).

[105]D. V. Hutton, *Fundamentals of Finite Element Analysis* (McGraw-Hill Higher Education, Boston, July 2003).

[106]K. Tsugawa, M. Ishihara, Y. J. Kim, and M. Hasegawa, “Nucleation enhancement of nanocrystalline diamond growth at low substrate temperatures by adamantane seeding”, Journal of Physical Chemistry C **114**, 3822–3824 (2010).

[107]H. Windischmann, G. F. Epps, Y. Cong, and R. W. Collins, "Intrinsic stress in diamond films prepared by microwave plasma CVD", Journal of Applied Physics **69**, 2231–2237 (1991).

[108]W. Fortunato, A. J. Chiquito, J. C. Galzerani, and J. R. Moro, "Crystalline quality and phase purity of CVD diamond films studied by Raman spectroscopy", Journal of Materials Science **42**, 7331–7336 (2007).

[109]J. Lee, B. Hong, R. Messier, and R. W. Collins, "Nucleation and bulk film growth kinetics of nanocrystalline diamond prepared by microwave plasma-enhanced chemical vapor deposition on silicon substrates", Applied Physics Letters **69**, 1716–1718 (1996).

[110]J. Zimmer and K. Ravi, "Aspects of scaling CVD diamond reactors", Diamond and Related Materials **15**, 229–233 (2006).

[111]I. Schmidt and C. Benndorf, "Low temperature CVD diamond deposition using halogenated precursors — deposition on low melting materials: Al, Zn and glass", Diamond and Related Materials, 11th European Conference on Diamond, Diamond-like Materials, Carbon Nanotubes, Nitrides and Silicon Carbide **10**, 347–351 (2001).

[112]M. Schwander and K. Partes, "A review of diamond synthesis by CVD processes", Diamond and Related Materials **20**, 1287–1301 (2011).

[113]S. Zuo, M. Yaran, T. Grotjohn, D. Reinhard, and J. Asmussen, "Investigation of diamond deposition uniformity and quality for freestanding film and substrate applications", Diamond and Related Materials **17**, 300–305 (2008).

[114]P. Spiberg, R. L. Woodin, J. E. Butler, and L. Dhar, "In-situ Fourier transform IR emission spectroscopy of diamond chemical vapor deposition", Diamond and Related Materials, Diamond 1992 **2**, 708–712 (1993).

[115]M. T. Bieberich and S. L. Girshick, "Control of substrate temperature during diamond deposition", Plasma Chemistry and Plasma Processing **16**, S157–S168 (1995).

[116]A. Mallik, K. Pal, N. Dandapat, B. Guha, S. Datta, and D. Basu, “Influence of the microwave plasma CVD reactor parameters on substrate thermal management for growing large area diamond coatings inside a 915 MHz and moderately low power unit”, Diamond and Related Materials **30**, 53–61 (2012).

[117]A. K. Mallik, S. Bysakh, M. Sreemany, S. Roy, J. Ghosh, S. Roy, J. C. Mendes, J. Gracio, and S. Datta, “Property mapping of polycrystalline diamond coatings over large area”, Journal of Advanced Ceramics **3**, 56–70 (2014).

[118]Z. J. Ayres, J. C. Newland, M. E. Newton, S. Mandal, O. A. Williams, and J. V. Macpherson, “Impact of chemical vapour deposition plasma inhomogeneity on the spatial variation of sp2 carbon in boron doped diamond electrodes”, Carbon **121**, 434–442 (2017).

[119]S. Mandal, “Nucleation of diamond films on heterogeneous substrates: a review”, RSC Advances **11**, 10159–10182 (2021).

[120]J. Hees, A. Kriele, and O. A. Williams, “Electrostatic self-assembly of diamond nanoparticles”, Chemical Physics Letters **509**, 12–15 (2011).

[121]O. A. Williams, M. Daenen, J. D’Haen, K. Haenen, J. Maes, V. V. Moshchalkov, M. Nesládek, and D. M. Gruen, “Comparison of the growth and properties of ultrananocrystalline diamond and nanocrystalline diamond”, Diamond and Related Materials, Diamond 2005 **15**, 654–658 (2006).

[122]H. Yamada, A. Chayahara, and Y. Mokuno, “Simplified description of microwave plasma discharge for chemical vapor deposition of diamond”, Journal of Applied Physics **101**, 063302 (2007).

[123]O. Williams, A. Kriele, J. Hees, M. Wolfer, W. Müller-Sebert, and C. Nebel, “High Young’s modulus in ultra thin nanocrystalline diamond”, Chemical Physics Letters **495**, 84–89 (2010).

[124]A. Köpf, R. Haubner, and B. Lux, “Multilayer coatings containing diamond and other hard materials on hardmetal substrates”, International Journal of Refractory Metals and Hard Materials **20**, 107–113 (2002).

[125]S. Bühlmann, E. Blank, R. Haubner, and B. Lux, “Characterization of ballas diamond depositions”, Diamond and Related Materials **8**, 194–201 (1999).

[126]N. Ali, V. F. Neto, and J. Gracio, “Promoting secondary nucleation using methane modulations during diamond chemical vapor deposition to produce smoother, harder, and better quality films”, Journal of Materials Research **18**, 296–304 (2003).

[127]S. Abedrabbo, J. C. Hensel, A. T. Fiory, B. Sopori, W. Chen, and N. M. Ravindra, “Perspectives on emissivity measurements and modeling in silicon”, Materials Science in Semiconductor Processing **1**, 187–193 (1998).

[128]D. S. Knight and W. B. White, “Characterization of diamond films by Raman spectroscopy”, Journal of Materials Research **4**, 385–393 (1989).

[129]M. Pandey, V. Sugandhi, R. D’cunha, A. K. Sikder, and D. S. Mishra, “Spectroscopic studies of hydrogen related defects in CVD diamond”, Bulletin of Materials Science **21**, 479–484 (1998).

[130]M. Pandey, R. D’Cunha, and A. K. Tyagi, “Defects in CVD diamond: Raman and XRD studies”, Journal of Alloys and Compounds **333**, 260–265 (2002).

[131]E. L. H. Thomas, S. Mandal, Ashek-I-Ahmed, J. E. Macdonald, T. G. Dane, J. Rawle, C.-L. Cheng, and O. A. Williams, “Spectroscopic Ellipsometry of Nanocrystalline Diamond Film Growth”, ACS Omega **2**, 6715–6727 (2017).

[132]N. Cella, H. El Rhaleb, J. P. Roger, D. Fournier, E. Anger, and A. Gicquel, “Ex-situ spectroscopic ellipsometry studies of micron thick CVD diamond films”, Diamond and Related Materials **5**, 1424–1432 (1996).

[133]Z. Pápa, J. Budai, I. Hanyecz, J. Csontos, and Z. Toth, “Depolarization correction method for ellipsometric measurements of large grain size zinc-oxide films”, Thin Solid Films **571**, 562–566 (2014).

[134]C. M. Herzinger, B. Johs, W. A. McGahan, J. A. Woollam, and W. Paulson, “Ellipsometric determination of optical constants for silicon and thermally grown silicon dioxide via a multi-sample, multi-wavelength, multi-angle investigation”, Journal of Applied Physics **83**, 3323–3336 (1998).

[135]J. C. Arnault, S. Saada, M. Nesladek, O. A. Williams, K. Haenen, P. Bergonzo, and E. Osawa, “Diamond nanoseeding on silicon: Stability under H2 MPCVD exposures and early stages of growth”, Diamond and Related Materials, Proceedings of Diamond 2007, the 18th European Conference on Diamond, Diamond-Like Materials, Carbon Nanotubes, Nitrides and Silicon Carbide **17**, 1143–1149 (2008).

[136]E. D. Palik, *Handbook of optical constants of solids.* Nachdr., Vol. 3 (Acad. Press, San Diego, Calif., 2003).

[137]M. Williams and E. Arakawa, “Optical properties of glassy carbon from 0 to 82 eV”, Journal of Applied Physics **43**, 3460–3463 (1972).

[138]J. A. Cuenca, E. Thomas, S. Mandal, O. Williams, and A. Porch, “Microwave determination of sp2 carbon fraction in nanodiamond powders”, Carbon **81**, 174–178 (2015).

[139]C. G. Granqvist and O. Hunderi, “Optical properties of ultrafine gold particles”, Physical Review B **16**, 3513–3534 (1977).

[140]D. E. Aspnes and A. A. Studna, “Dielectric functions and optical parameters of si, ge, gap, gaas, gasb, inp, inas, and insb from 1.5 to 6.0 ev”, Phys. Rev. B **27**, 985–1009 (1983).

[141]R. W. Collins, Y. Cong, Y. .-. Kim, K. Vedam, Y. Liou, A. Inspektor, and R. Messier, “Real-time and spectroscopic ellipsometry characterization of diamond and diamond-like carbon”, Thin Solid Films, International Conference on Metallurgical Coatings, San Diego, 1989 **181**, 565–578 (1989).

[142]D. N. Belton, S. J. Harris, S. J. Schmieg, A. M. Weiner, and T. A. Perry, “*In situ* characterization of diamond nucleation and growth”, Applied Physics Letters **54**, 416–417 (1989).

[143]D. J. Monk, D. S. Soane, and R. T. Howe, “A review of the chemical reaction mechanism and kinetics for hydrofluoric acid etching of silicon dioxide for surface micromachining applications”, Thin Solid Films **232**, 1–12 (1993).

[144]J. M. Harris, H. C. Gatos, and A. F. Witt, “Etching Characteristics of Silicon Carbide in Hydrogen”, Journal of The Electrochemical Society **116**, 380 (1969).

[145]R. W. Collins, Y. Cong, H. V. Nguyen, I. An, K. Vedam, T. Badzian, and R. Messier, “Real time spectroscopic ellipsometry characterization of the nucleation of diamond by filament-assisted chemical vapor deposition”, Journal of Applied Physics **71**, 5287–5289 (1992).

[146]J. Mistrik, P. Janicek, A. Taylor, F. Fendrych, L. Fekete, A. Jager, and M. Nesladek, "Spectroscopic ellipsometry characterization of nano-crystalline diamond films prepared at various substrate temperatures and pulsed plasma frequencies using microwave plasma enhanced chemical vapor deposition apparatus with linear antenna delivery", Thin Solid Films **571**, 230–237 (2014).

[147]I. Pintér, P. Petrik, E. Szilágyi, S. Kátai, and P. Deák, "Characterization of nucleation and growth of MW-CVD diamond films by spectroscopic ellipsometry and ion beam analysis methods", Diamond and Related Materials **6**, 1633–1637 (1997).

[148]T. Lohner, P. Csíkvári, N. Q. Khánh, S. Dávid, Z. E. Horváth, P. Petrik, and G. Hárs, "Spectroellipsometric and ion beam analytical investigation of nanocrystalline diamond layers", Thin Solid Films, 5th International Conference on Spectroscopic Ellipsometry (ICSE-V) **519**, 2806–2810 (2011).

[149]L. Wang, Y. Xia, M. Zhang, H. Shen, Q. Su, B. Gu, and Y. Lou, "Spectroscopic ellipsometric study of CVD diamond films: modelling and optical properties in the energy range of 0.1–0.4 eV", Journal of Physics D: Applied Physics **37**, 1976 (2004).

[150]Z. Fang, Y. Xia, L. Wang, W. Zhang, Z. Ma, and M. Zhang, "An ellipsometric analysis of CVD-diamond films at infrared wavelengths", Carbon **41**, 967–972 (2003).

[151]J. Cifre, J. Campmany, E. Bertran, and J. Esteve, "Spectroscopic ellipsometry measurements of the diamond-crystalline Si interface in chemically vapour-deposited polycrystalline diamond films", Diamond and Related Materials, Diamond 1992 **2**, 728–731 (1993).

[152]P. Lautenschlager, M. Garriga, L. Vina, and M. Cardona, "Temperature dependence of the dielectric function and interband critical points in silicon", Physical Review B **36**, 4821–4830 (1987).

[153]W. Kern and D. A. Puotinen, "Cleaning solutions based on hydrogen peroxide for use in silicon semiconductor technology", RCA Review **31**, 187–206 (1970).

[154]W. Kern, "The evolution of silicon wafer cleaning technology", Journal of The Electrochemical Society **137**, 1887 (1990).

[155] M. Ishii, K. Nakashima, I. Tajima, and M. Yamamoto, “Properties of silicon surface cleaned by hydrogen plasma”, Applied Physics Letters **58**, 1378–1380 (1991).

[156] B. D. Johs and C. M. Herzinger, “Methods for uncorrelated evaluation of parameters in parameterized mathematical model equations for window retardence, in ellipsometer and polarimeter systems”, US6034777A (Mar. 2000).

[157] Z. G. Hu and P. Hess, “Optical constants and thermo-optic coefficients of nanocrystalline diamond films at 30–500°C”, Applied Physics Letters **89**, 081906 (2006).

[158] P. G. Snyder, J. A. Woollam, S. A. Alterovitz, and B. Johs, “Modeling AlxGa1-xAs optical constants as functions of composition”, Journal of Applied Physics **68**, 5925–5926 (1990).

[159] I. Villalpando, P. John, S. Porro, and J. I. B. Wilson, “Hydrogen plasma etching of diamond films deposited on graphite”, Diamond and Related Materials **20**, 711–716 (2011).

[160] P. B. Barna and M. Adamik, “Fundamental structure forming phenomena of polycrystalline films and the structure zone models”, Thin Solid Films **317**, 27–33 (1998).

[161] J. H. Parker, D. W. Feldman, and M. Ashkin, “Raman Scattering by Silicon and Germanium”, Physical Review **155**, 712–714 (1967).

[162] C. S. Wang, J. M. Chen, R. Becker, and A. Zdetsis, “Second order Raman spectrum and phonon density of states of silicon”, Physics Letters A **44**, 517–518 (1973).

[163] S. Tóth, P. Németh, P. Rácz, L. Himics, P. Dombi, and M. Koós, “Silicon carbide nanocrystals produced by femtosecond laser pulses”, Diamond and Related Materials **81**, 96–102 (2018).

[164] F. Cerdeira, T. A. Fjeldly, and M. Cardona, “Raman study of the interaction between localized vibrations and electronic excitations in boron-doped silicon”, Physical Review B **9**, 4344–4350 (1974).

[165] M. Chandrasekhar, H. R. Chandrasekhar, M. Grimsditch, and M. Cardona, “Study of the localized vibrations of boron in heavily doped Si”, Physical Review B **22**, 4825–4833 (1980).

[166]U. Mishra, P. Parikh, and Y.-F. Wu, “AlGaN/GaN HEMTs-an overview of device operation and applications”, Proceedings of the IEEE **90**, 1022–1031 (2002).

[167]U. K. Mishra, L. Shen, T. E. Kazior, and Y.-F. Wu, “GaN-Based RF Power Devices and Amplifiers”, Proceedings of the IEEE **96**, 287–305 (2008).

[168]A. Bar-Cohen, J. J. Maurer, and D. H. Altman, “Embedded Cooling for Wide Bandgap Power Amplifiers: A Review”, Journal of Electronic Packaging **141**, 040803 (2019).

[169]Sangmin Lee, R. Vetury, J. D. Brown, S. R. Gibb, W. Z. Cai, Jinming Sun, D. S. Green, and J. Shealy, “Reliability assessment of AlGaN/GaN HEMT technology on SiC for 48V applications”, in 2008 IEEE International Reliability Physics Symposium (Apr. 2008), pp. 446–449.

[170]R. Gaska, A. Osinsky, J. Yang, and M. Shur, “Self-heating in high-power AlGaN-GaN HFETs”, IEEE Electron Device Letters **19**, 89–91 (1998).

[171]M. E. Levinshteĭn, S. L. Rumyantsev, and M. Shur, eds., *Properties of advanced semiconductor materials: GaN, AlN, InN, BN, SiC, SiGe* (Wiley, New York, 2001).

[172]D. Francis, F. Faili, D. Babić, F. Ejeckam, A. Nurmikko, and H. Maris, “Formation and characterization of 4-inch GaN-on-diamond substrates”, Diamond and Related Materials, NDNC 2009 **19**, 229–233 (2010).

[173]T. Gerrer, V. Cimalla, P. Waltereit, S. Müller, F. Benkhelifa, T. Maier, H. Czap, O. Ambacher, and R. Quay, “Transfer of AlGaN/GaN RF-devices onto diamond substrates via van der Waals bonding”, International Journal of Microwave and Wireless Technologies **10**, Publisher: Cambridge University Press, 666–673 (2018).

[174]W. M. Waller, J. W. Pomeroy, D. Field, E. J. W. Smith, P. W. May, and M. Kuball, “Thermal boundary resistance of direct van der Waals bonded GaN-on-diamond”, Semiconductor Science and Technology **35**, Publisher: IOP Publishing, 095021 (2020).

[175]K. Hirama, Y. Taniyasu, and M. Kasu, “AlGaN/GaN high-electron mobility transistors with low thermal resistance grown on single-crystal diamond (111) substrates by metalorganic vapor-phase epitaxy”, Applied Physics Letters **98**, 162112 (2011).

[176] Y. Zhou, R. Ramaneti, J. Anaya, S. Korneychuk, J. Derluyn, H. Sun, J. Pomeroy, J. Verbeeck, K. Haenen, and M. Kuball, "Thermal characterization of polycrystalline diamond thin film heat spreaders grown on GaN HEMTs", Applied Physics Letters **111**, 041901 (2017).

[177] J. Baek, J. Ma, M. F. Becker, J. W. Keto, and D. Kovar, "Correlations between optical properties, microstructure, and processing conditions of Aluminum nitride thin films fabricated by pulsed laser deposition", Thin Solid Films **515**, 7096–7104 (2007).

[178] L. Duta, G. E. Stan, H. Stroescu, M. Gartner, M. Anastasescu, Z. Fogarassy, N. Mihailescu, A. Szekeres, S. Bakalova, and I. N. Mihailescu, "Multi-stage pulsed laser deposition of aluminum nitride at different temperatures", Applied Surface Science, E-MRS 2015 Spring Meeting Symposium CC: "Laser and plasma processing for advanced applications in material science", 11-15 May 2015, Lille (France) **374**, 143–150 (2016).

[179] A. Mohammad, D. Shukla, S. Ilhom, B. Willis, B. Johs, A. K. Okyay, and N. Biyikli, "Real-time in situ ellipsometric monitoring of aluminum nitride film growth via hollow-cathode plasma-assisted atomic layer deposition", Journal of Vacuum Science & Technology A **37**, 020927 (2019).

[180] J. M. Khoshman and M. E. Kordesch, "Optical characterization of sputtered amorphous aluminum nitride thin films by spectroscopic ellipsometry", Journal of Non-Crystalline Solids **40-42**, 3334–3340 (2005).

[181] J. Woollam, B. Johs, C. Herzinger, J. Hilfiker, R. Synowicki, and C. Bungay, "Overview of Variable Angle Spectroscopic Ellipsometry (VASE), Part I: Basic Theory and Typical Applications", Proceedings of SPIE - The International Society for Optical Engineering **-1**, 3–28 (1999).